Ministry of Higher education and scientific research

University Hassiba Benbouali of Chlef

Faculty of Technology

Department of Electrical Engineering

THESIS

Submitted for the fulfillment of degree of

DOCTORATE

In Electrical Engineering

Option: Electrical Engineering and Renewable Energy

By

Abdelatif GADOUM

Theme:

MODELING OF NON-EQUILIBRIUM COLD PLASMA APLIED TO HYDROGEN PRODUCTION

Thesis defense: 18 /12 /2019, in front of jury composed of:

Abdelkader KANSAB	MCA	University of Chlef	President
Djilali BENYOUCEF	Professor	University of Chlef	Supervisor
Bachir BELMADANI	Professor	University of Chlef	Examiner
Toufik TAHRI	Professor	University of Chlef	Examiner
Driss RAOUTI	MCA	University of Saida	Examiner

Ministère de l'Enseignement Supérieur et de la Recherche Scientifique

Université Hassiba Benbouali de Chlef

Faculté de Technologies.

Département d'électrotechnique.

THÈSE

Présentée pour l'obtention du diplôme de

DOCTORAT

Filière : électrotechnique.

Spécialité : Electrotechnique et Energies Renouvelables.

Par

Abdelatif GADOUM

Thème:

MODELISATION D'UN PLASMA FROID HORS-EQUILIBRE POUR LA PRODUCTION D'HYDROGENE

Soutenue le : 18 /12 /2019, devant le jury composé de :

Abdelkader KANSAB	MCA	Université de Chlef	Président
Djilali BENYOUCEF	Professeur	Université de Chlef	Rapporteur
Bachir BELMADANI	Professeur	Université de Chlef	Examinateur
Toufik TAHRI	Professeur	Université de Chlef	Examinateur
Driss RAOUTI	MCA	Université de Saida	Examinateur

Acknowledgement

I would like to express my sincere and warm thanks to Mr. **Djilali BENYOUCEF**, who trained me and accompanied me throughout these five years with great patience and pedagogy, for the judicious advice that he knew how to bring me, for the trust he gave me but also for his enthusiasm, his help and the unique way he managed to supervise my work. Also, his advices even outside of study. All my respect for him, I ask God Almighty, Lord of the Great Throne, to grant him all the best

Finally, I thank my family especially my father; Ali, my brother; Saber, my two sisters; Saliha and Rahima,

and so all my friends especially:

Yacine AYAD, Abdelhak BACHIOUA & his wife and Adel_(Fouad) KORICHI & his wife.

Gadoum Abdelatif

ABSTRACT

تتم دراسة استخدام الهيدروجين كوقود للطاقة التي تنتجها خلايا الوقود بشكل متزايد في العديد من المجالات مثل المركبات الجوية والارضية. المهم هو إيجاد بدائل للوقود الأحفوري والحد من المشكلات البيئية. غاز الهيدروجين أخف بكثير من الهواء، يرتفع بسرعة ويتسرب من الغلاف الجوي. هذا هو السبب في أن طور غاز الهيدروجين (H2) ليس في حد ذاته على الأرض. يتحد الهيدروجين بسهولة مع العناصر الكيميائية الأخرى مثل الماء والهيدروكربونات والكحول ... الهيدروجين موجود أيضًا في الكتلة الحيوية الطبيعية بما في ذلك النباتات والحيوانات. نظرًا لأنه يتعين علينا إنفاق الطاقة لإنتاج الهيدروجين، فإننا نتحدث عن متجهات الطاقة وليس الطاقة.

يمكن إنتاج الهيدروجين من مصادر طبيعية مثل الغاز الطبيعي والمياه وغيرها من المصادر. في الوقت الحالي، في التقنيات المستخدمة، فإن الغاز المستخرج ليس هيدروجين وحده، ولكن أيضًا النفايات السائلة الغازية مثل أول أكسيد الكربون (CO) وأيضًا ثاني أكسيد الكربون (CO2) المعروف باسم إسهامه في تفاقم تأثير الاحتباس الحراري. لذا، فإن السؤال الرئيسي الذي يطرح نفسه في تطوير تقنيات إنتاج الهيدروجين هو العثور على أكثر التقنيات كفاءة وأقل تلويثًا. من المهم أن نلاحظ أن الهيدروجين غير سام على الإطلاق ولديه كفاءة عالية في استخدام الطاقة لأن كيلوغرام من الهيدروجين يمكن أن ينتج 33 كيلو واط / ساعة من الطاقة الكهربائية، وهو ما يعادل ثلاثة أضعاف الطاقة الناتجة عن حرق البنزين.

تفكك الهيدروكربونات بواسطة البلازما الباردة مطلوب بشدة كتقنية بيئية لإنتاج الهيدروجين. من المعروف أن الهيدروكربونات يمكنها أن تتحلل مباشرة إلى الكربون الصلب والهيدروجين لتزويد خلايا الوقود لتوليد الكهرباء. البلازما الباردة غير المتوازنة والتي تتميز بدرجة حرارة إلكترونية عالية في بيئة غازية باردة يمكن توليدها عن طريق مصادر كهربائية أو كهرومغناطيسية مثل البلازما الباردة الناتجة عن تفريغ الترددات الراديوية أو مصادر هليكون (Helicon) تردد الراديوي (RF-H plasma) أو الميكروويف بلازما(MW) ، إلخ.

الهدف من هذه الأطروحة هو نمذجة البلازما الباردة الخارجة عن التوازن المستخدمة لإنتاج الهيدروجين لتغذية خلايا الوقود التي تتيح إنتاج الكهرباء بواسطة هذه التكنولوجيا "الخضراء."

الكلمات المفتاحية: الهيدروجين، الميثان، البلازما الباردة، بلازما ذات تردد راديو، نموذج الموائع، معادلات التفاعل.

ABSTRACT

The use of hydrogen as a fuel for the energy produced by fuel cells is being increasingly studied in several areas such as small air and ground vehicles. The interest is to find alternatives to fossil fuels and to limit environmental problems. Hydrogen gas being much lighter than air, rises rapidly and escapes from the atmosphere. This is the reason why hydrogen gas phase (H2) is not by itself on the earth. Hydrogen combines easily with other chemical elements such as water, hydrocarbons, alcohols ... Hydrogen is also present in natural biomass including both plants and animals. Since we have to spend energy to produce hydrogen, we are talking about energy vectors and not energy.

Hydrogen can be produced from natural sources such as natural gas, water, biomass and other sources. At the present time, in the technologies used, the gas extracted is not Hydrogen alone, but also toxic gaseous effluents such as carbon monoxide (CO) and also carbon dioxide (CO2) known as its contribution to the worsening of the greenhouse effect. So, the main question that arises in the development of hydrogen production technologies is to find the most efficient and least polluting technique. It is important to note that hydrogen is absolutely nontoxic and has a high energy efficiency since a kilogram of hydrogen can produce 33kW / h of electrical energy, which is three times the energy from burning benzene.

The dissociation of hydrocarbons by a cold plasma is strongly required as an environmental technology for the production of hydrogen. It is known that hydrocarbons can decompose directly into solid carbon and Hydrogen to fuel fuel cells for electricity generation. Non-equilibrium cold plasmas that are characterized by a high electronic temperature in a cold gaseous environment can be generated by electrical or electromagnetic sources such as cold plasmas from radio frequency (RF) discharges, radiofrequency helicon sources (RF-H plasma) or microwave (MW plasma), Dielectric Barrier discharges (DBD plasma), and also corona discharges, etc.

The objective of this thesis is the modeling of the out-of-equilibrium cold plasma used for the production of Hydrogen to feed the fuel cells that allow the production of electricity by this "green" technology.

Keywords : Hydrogen, Methane, Cold Plasmas, RF Plasmas, Non Equilibrium Plasmas, Fluid Model, Reaction Rates, Cross Section

ABSTRACT

L'utilisation de l'hydrogène comme carburant pour l'énergie produite par les piles à combustible est de plus en plus étudiée dans plusieurs domaines tels que les petits véhicules aériens et terrestres. L'intérêt est de trouver des alternatives aux énergies fossiles et de limiter les problèmes environnementaux. Le gaz hydrogène étant beaucoup plus léger que l'air, monte rapidement et s'échappe de l'atmosphère. C'est la raison pour laquelle la phase d'hydrogène gazeux (H2) n'est pas seule sur la terre. L'hydrogène se combine facilement avec d'autres éléments chimiques tels que l'eau, les hydrocarbures, les alcools ... L'hydrogène est également présent dans la biomasse naturelle, y compris les plantes et les animaux. Comme nous devons dépenser de l'énergie pour produire de l'hydrogène, nous parlons de vecteurs énergétiques et non d'énergie.

L'hydrogène peut être produit à partir de sources naturelles telles que le gaz naturel, l'eau, la biomasse et d'autres sources. À l'heure actuelle, dans les technologies utilisées, le gaz extrait n'est pas de l'hydrogène seul, mais aussi des effluents gazeux toxiques comme le monoxyde de carbone (CO) et également le dioxyde de carbone (CO2) connu pour sa contribution à l'aggravation de l'effet de serre. Ainsi, la principale question qui se pose dans le développement des technologies de production d'hydrogène est de trouver la technique la plus efficace et la moins polluante. Il est important de noter que l'hydrogène est absolument non toxique et a une efficacité énergétique élevée, car un kilogramme d'hydrogène peut produire 33 kW / h d'énergie électrique, soit trois fois l'énergie produite par la combustion du benzène.

La dissociation des hydrocarbures par un plasma froid est fortement requise en tant que technologie environnementale pour la production d'hydrogène. Il est connu que les hydrocarbures peuvent se décomposer directement en carbone solide et en hydrogène pour alimenter les piles à combustible pour la production d'électricité. Les plasmas froids hors équilibre caractérisés par une température électronique élevée dans un environnement gazeux froid peuvent être générés par des sources électriques ou électromagnétiques telles que les plasmas froids provenant de décharges par radiofréquence (RF), les sources d'hélicon radiofréquence (plasma RF-H) ou les micro-ondes (Plasma MW), les décharges à barrière diélectrique (plasma DBD), ainsi que les décharges corona, etc.

L'objectif de cette thèse est la modélisation du plasma froid hors équilibre utilisé pour la production d'hydrogène pour alimenter les piles à combustible qui permettent la production d'électricité par cette technologie "verte".

Mots-clés: Hydrogène, Méthane, Plasmas froids, Plasmas RF, Plasmas hors équilibre, Modèle fluide, Taux de réaction, Section efficace

SYMBOLS

a : acceleration of the particle

B : the magnetic field

E : the electric field

C_B : blocking ability

f_s : function of distribution of particles of type s

f_p : the plasma frequency

i_c : conduction current

i_D : displacement current

k_B : constant Boltzmann

m_e : the electron mass

m_s : the mass of the particle type s

m : the particle mass

m_p : the mass of the projectile particle

m_c *:* the mass of the target particle

n_0* : the density of excited neutral particles

n_0 : the density of neutral particles

n_i* : the density of excited ions

n_r : the density of radicals

n_s : the density of type s particles

P_{eff} : the effective power coupled to the plasma

P_{in} : Input Power

Q : the electric charge

T : Temperature

T_e : Electronic temperature

T_{rf} : period of the radio frequency cycle

r : radius

t : time

V_{dc} : the self bias voltage

V_{rf} : radio frequency voltage

v : the speed of the particle

v_p : the velocity of the projectile particle

v_c : the speed of the target particle

v_r : the relative velocity between the projectile particle and the target particle.

μ_r : reduced mass

φ : Particle flow

τ_i : the ionization rate

τ_d : the dissociation rate

τ^* : the excitation rate

λ_D : Debye's length

λ_l : length of Landau

λ_{vol} : the free path

ε : the energy of the particle

ε_p : the energy of the projectile particle

ε_c : the energy of the target particle

ρ : the charge density of the charged particles

σ_i : the cross section of the type i collision

σ_T : the total cross section of collision

θ : the axial angle of velocity vector in the lab benchmark.

ϕ : the azimuth angle of vector velocity in the laboratory benchmark.

χ : the axial angle of velocity vector in the reference of the center of mass

ψ : velocity vector azimuth angle in the center of mass reference

η : the energy loss factor

α_B : the electric polarizability of the atom

ω : the pulsation

ω_p : plasma pulsation

List of Figures

LIST OF FIGURES

List of Tables

Table of contents

GENERAL INTRODUCTON

General Introduction

The use of hydrogen as a fuel for the energy produced by fuel cells is being increasingly studied in several areas such as small air or land vehicles. The interest is to find alternatives to fossil fuels and to limit environmental problems. Hydrogen gas being much lighter than air rises rapidly and escapes from the atmosphere. This is the reason why the hydrogen gas phase (H_2) is not by itself on the ground. Hydrogen combines easily with other chemical elements such as water, hydrocarbons, alcohols ...etc. Hydrogen is also present in natural biomass including both plants and animals. Since we have to spend energy to produce hydrogen, we are talking about energy vectors and not energy.

Hydrogen can be produced from natural sources such as natural gas, water, biomass and other sources. At the present time, in the technologies used, the gas extracted is not Hydrogen alone, but also toxic gaseous effluents such as carbon monoxide (CO) and also carbon dioxide (CO_2) known to contribute to the worsening of the greenhouse effect. So, the main question that arises in the development of hydrogen production technologies is to find the most efficient and least polluting technical. It is important to note that hydrogen is absolutely nontoxic and has high energy efficiency since a kilogram of hydrogen can produce 33kW / h of electrical energy, which is three times the energy from burning benzene. The dissociation of hydrocarbons by cold plasma is strongly required as an environmental technology for the production of hydrogen. It is known that hydrocarbons can decompose directly into carbon in the solid state and Hydrogen to fuel cells for the production of electricity. Non-equilibrium cold plasmas that are characterized by a high electronic temperature in a cold gaseous environment can be generated by electrical or electromagnetic sources such as cold plasmas from Radio Frequency (RF) discharges, radiofrequency (RF-H plasma) sources or microwave (MW plasma), Dielectric Barrier discharges (DBD plasma), and also corona discharges, etc.

The objective of this thesis is the modeling of non-equilibrium cold plasma used for the production of Hydrogen to supply fuel cells that allow the production of electricity by this "green" technology.

In the first chapter, we show the actual situation of the world in term of energy and the need to renewable safe energies, as well as, the production of hydrogen methods and the function of fuel cell.

The second chapter is devoted to the generalities of the plasma, the different types of plasma, characteristics of cold plasma, and then we will talk about different types of existing plasmas, as well as the possible collisions in the plasma. Finally, we draw up a state of the art of plasma sources operating at low pressure for different excitation sources, as well as their fields of application and the different existing mathematical models of low-temperature plasma.

In the third chapter, we study electron-methane collision cross sections, where the collision processes involved are: elastic moment transfer, two composite vibration modes, all partial dissociations and all partial ionizations. This set of collision cross sections was validated by a comparison between the transport coefficients calculated using this dataset and the measurements published in the literature. We also calculated and adjusted the rate coefficients of the partial dissociation into neutrals and the partial ionization, which can be used as input parameters for fluid models.

The fourth chapter of this thesis is reserved to the detailed description and the modeling of capacitive coupled discharge plasma in methane by presenting the most existing and dominant species. In this chapter, a One Dimension (1D) simulation for more than 300 reactions is performed, in the order to know the governing reactions. The work carried out has highlighted a number of phenomena taking place in the methane plasma especially the densities of existing species.

In chapter five we will present another modeling results; which concern a 2D modeling of low pressure inductively coupled discharge in methane, in the order to compute the density of hydrogen for different powers, the simulation is done for more than 300 reactions; a set of 105 electronic impact collision cross sections with: CH_4, CH_3, CH_2, CH, C, H, H_2, C_2H_2, C_2H_4 and C_2H_6. In this chapter, the neutral-neutral and ion-neutral reactions, and also the wall reactions are considered. In this simulation we include the ICP module and laminar flow module for a good description of the phenomena existing in this type of plasma.

Finally, in the general conclusion we will discuss the different results obtained in this study and closed this work with some perspectives.

CHAPTER: I

STATE OF THE ART AND FEASIBILITY OF HYDROGEN PRODUCTION BY METHANE COLD PLASMA

I.1. Introduction

Our modern societies are spending increasing amounts of energy, most of them from world heritage, which has taken hundreds of millions of years to build up: oil, coal or gas.

Today, humanity is dependent on these energies which serve for many uses such as transport, agriculture, building, and the industry. The total energy consumption in the world has increased for example 35% between 1973 and 2000, which is not without posing serious problems as for the exhaustion of these fossil resources, without omitting their impact on the environment. At the pace we have been running since 1850, the beginning of the industrial era, it will take us less than two centuries to exhaust this irreplaceable heritage on the scale of the history of the human race. Modern economic development as we know it today, resulting from the process of industrialization of the last two centuries, feeds primarily on non-renewable mineral resources extracted from the subsoil. It benefits from relatively abundant and cheap energy from fossil fuels - oil, natural gas and coal - and also from fissile fuels such as uranium. Oil, with exceptional qualities, has become the main source of industrial and military power. It replaced coal, used massively since the nineteenth century, as reference energy. High energy intensity, this black gold has become the engine of growth, especially from the 1950s to 60th. It is the leading source of fuels for land and sea transport, and even the only source for aviation. This raw material is at the very heart of the way of life of the majority of humans, in terms of energy of course but also that of objects, food production or even health. In 150 years, our ways of life were radically changed and our standards of life multiplied, the productivity gain between the last century and our century was not negligible. It is the energetic abundance that allowed these mutations; our daily life was transformed by energy. The energy consumption of humanity has thus been multiplied by nearly 30 since 1900 and 150 since 1850.

I.2. Fossil Energy

I.2.1 Quantity of CO_2 released per energy per kWh

The main disadvantage of using fossil fuels is that they produce carbon dioxide (CO_2). As a greenhouse gas, CO_2 is one of the main elements responsible for acid pollution. On its own, it has resulted in more than 50% of the increase in all greenhouse gases. Its environmental impact is in the long term, its lifespan in the atmosphere being several centuries. Thus, if

tomorrow we stop these fossil carbon dioxide emissions, it will still take several million years for the quality of CO_2 in the air to return to the level that was his before the industrial revolution. In addition, carbon dioxide is not the only greenhouse gas generated by fossil fuels. Methane, produced during the exploitation of natural gas fields and coal mines. Moreover, we must be aware that already the climatic evolution of the next 20 years is irreversible. But we still have the power to preserve life for generations to come, bequeathing them a planet still hospitable if we drastically reduce our CO_2 emissions.

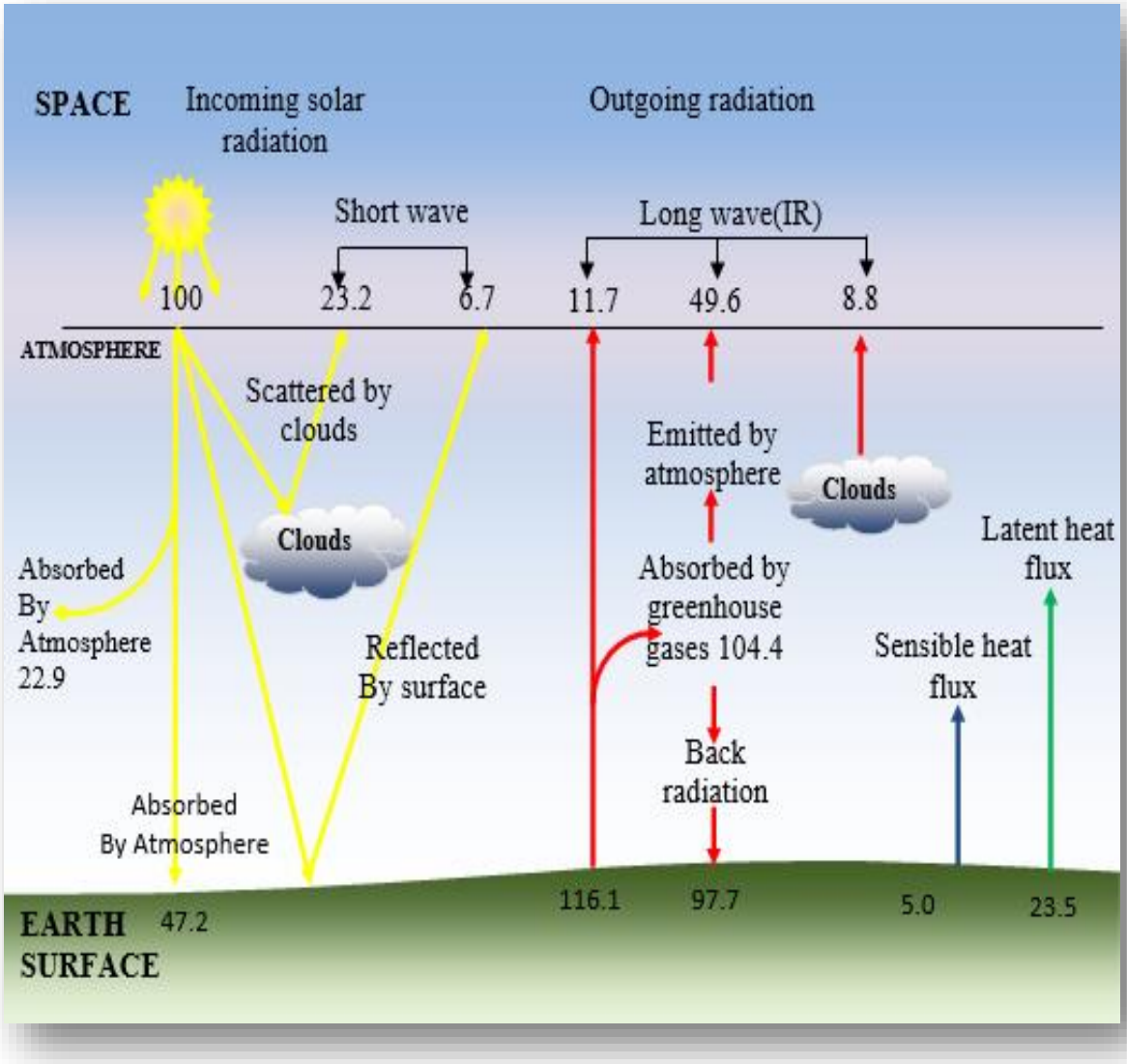

Fig. I-1: Schematic diagram showing the Earth energy balance through incoming and outgoing radiation. All values are in W m^{-2} and represent the energy budget for the period of March 2000 to May 2004. The broad arrows indicate the flow of energy in proportion to their importance.

I.2.2. Evolution of the consumption of fossil energies

The primary energy currently traded in the world is about 9 Gtep (billions of tons of oil equivalent) per year; it is 90% fossil fuels, of which hydrocarbons, oil and gas, account for two-thirds, or 5.4 Gtoe. Coal provides the last third. Oil and gas are considered as "loopback energies" in all medium-term forecasts to balance the demand of the various sectors of the economy. Their production would thus reach 7 to 9 Gtep in 2020, for a global primary energy demand of 13 to 15 Gtoe. In this perspective, half of the proven oil reserves, currently estimated at 145 Gt will be consumed between 2000 and 2020, and one-third of natural gas reserves, currently about 150 Gtoe. Energy is used for many purposes: for transportation, for heating homes or food, for industry, for lighting and other electrical devices etc. The total energy consumption in the world is clear that in continuous increasing (between 1973 and 2000: + 35%).

I.2.3. An unsustainable and uncertain situation

Since the 1970s, debates have raged between the optimists, who trust the market forces, the capacity for innovation and the technological ingenuity of the man to overcome these obstacles, and the pessimists (who nevertheless want to realistic), for whom it is urgent to take seriously the double threat of post-peak oil and global warming. Pessimists call to correct the excesses of the consumer society that undermine the ecological balance of the land. In a relatively optimistic scenario, the International Energy Agency (IEA) projects global demand for primary energy to increase by 36% between 2008 and 2035, or 1.2% per year, from 12.3 billion tons of oil equivalent (Mtoe) to more than 16,700 Mtoe (IEA 2010). This 'new policies' scenario assumes that all countries are implementing the policy commitments and action plans they have announced to reduce their CO_2 emissions. Whatever the scenario, the IEA predicts that fossil fuels will remain the main source of energy in 2035 and account for more than half of the increase in total primary energy demand. As a result of demographic and economic growth and urbanization in emerging countries, 93% of the additional demand will come from emerging economies and developing countries. In addition, the IEA implicitly indicates that conventional oil production would have already reached its historical peak in 2006 at 70 million barrels per day. In 2035, the deposits exploited today are expected to provide only one-fifth of total conventional oil production, which means that more than 80% of production will have to come from new deposits in 2035. This projection seems very optimistic.

I.3. Renewable energies

The Renewable energies are modes of energy production using forces or resources whose stocks are unlimited. They are drawn from the elements (earth, water, air and fire) and the sun. Renewable energies are today defined as a set of diversified supply chains whose implementation does not entail in any way the extinction of the initial resource. Renewable energies are a bit more popular, but only for a few years. States, manufacturers, and us simple consumers, have long neglected these energies naturally offered by the planet in favor of energies immediately more profitable, but also more costly for the environment. Overall, the share of renewable energy in electricity generation is low. The world's renewable energy production is about 20%, with fossil fuels, such as oil or coal (63%), and nuclear (17%).

I.3.1. Types of renewable energy

Solar energy: The sun's rays make it possible to generate so-called photovoltaic energy that transforms radiation into electricity and solar thermal energy that converts it into heat.

Geothermal energy: Under your feet, at about 30 km deep, the temperatures are around 1000 degrees; the magma diffuses its heat under the earth's crust. Potential not yet fully explored but geothermal energy is already producing electricity and heating.

Wind power: These are wind turbines whose blades use the power of the wind, whose driving force is used in the movement of sailboats and other vehicles or transformed by means of an aerogenerator device such as a wind turbine or a windmill in a diversely usable energy.

Hydraulic: Water is also a force of nature used to create clean energy. In addition to hydroelectric power plants, associated with dams, tides and ocean currents are exploitable and inexhaustible sources for generating electricity.

The biomass: The biomass is the organic matter of plant origin (microalgae included), animal, bacterial or fungal (fungi), usable as a source of energy. Energy can be extracted by direct combustion (eg wood energy), or by combustion after a process of transformation of the raw material, for example methanation (biogas, or its purified version biomethane) or other chemical transformations (including pyrolysis, hydrothermal carbonization and methods of producing biofuels or "agrofuels").

I.4. Hydrogen Production

Unlike fossil fuels, H_2 cannot be extracted from underground; it must be produced from another source, as a secondary fuel. The annual production of H_2 has been estimated at around 65 million tons by the International Energy Agency in 2007, of which ~ 96 % comes from fossil fuels, either from reforming of natural gas, refinery/chemical off-gases or by coal gasification. If a transition towards H_2 energy and fuel cells is to be made possible, large quantities of renewable H_2 will need to be produced from an abundant source and at a lower cost than offered by current methods. This has been internationally recognized by many governments, who currently have initiatives in place for the development of H_2 technologies. Brief descriptions of the key emerging technologies for H_2 production are given in this section[1-11].

Reforming of natural gas with carbon sequestration – The most established method for H_2 production is by reforming of natural gas. However, even if significant advances were to bring down the cost of methane reforming, there is still the issue of the carbon by-product. Carbon capture and sequestration (CCS) is a possible option, whereby the carbon dioxide product is liquefied and injected deep underground beneath layers of rock or into the deep ocean where it would form CO_2. These technologies are currently at an experimental stage and have significant technological, economic and environmental issues which would need to be addressed before it could be implemented on a large scale.

Biogas reforming – Reforming of biogas from renewable sources is a potential route to gas production, without the need for carbon sequestration. Since biogas contains CH_4 in conjunction with CO_2 there is no need for an additional oxidant.

Dry reforming of CH_4 with CO_2 using thermal catalysis - Dry reforming of methane with CO_2 is an attractive process from an environmental perspective as it involves the destruction of two greenhouse gases (1.7) that can be renewably generated as biogas. Dry reforming may also be applicable to low-grade natural gas that contains a large amount of CO_2, such as is often found at oil wells.

Biomass gasification/pyrolysis – This process is similar to the process of coal gasification, except that the organic matter comes from a renewable source, such as woody materials or waste organic products. Under conditions of high temperatures, catalysis and the

presence of an oxidant (O_2, air or steam), a combination of reactions can take place including pyrolysis, partial oxidation and steam reforming of hydrocarbons, as well as methane and the water-gas shift reaction. Optimization of reaction conditions can maximize the yield of gas production. Biomass gasification requires temperatures of ~ 700 °C; however, higher temperatures are usually favored in order to reduce the formation of tar.

Electrolysis of water – Electricity from renewable sources can be used to split H_2O into H_2 and O_2. The electricity can be supplied from intermittent sources such as wind turbines, solar cells, hydroelectric or geothermal facilities; for each of these sources the electricity generation does not necessarily meet the demand at a given time. Since it is difficult to store excess electricity, the energy can be used in electrolysis of H_2O to produce H_2, which behaves as an energy carrier that can be converted back to electricity when it is needed. This method has the advantage that it does not produce CO, which is incompatible with fuel cells.

The current method for hydrogen production involves dissociating hydrogen from hydrocarbons such as methane in a reaction with water vapor at very high temperatures. In such reactions, carbon dioxide gas and hydrogen gas are the resultant products. Currently, this process involves the production and emission of ~0.3mol CO_2 for 1mol of H_2, resulting in large production of a greenhouse gas in the extraction of hydrogen from methane. The ***helicon*** plasma reaction chamber (HPRC) is a device that produces molecular hydrogen gas by the dissociation of hydrogen-rich compounds such as methane gas, CH_4. The resultant carbon is collected in the form of solid graphite at an ion collection stage and the hydrogen gas is pumped out of the chamber in the collection stage.

In the study of B W Longmier et al [12], a high-density RF helicon plasma source is used to generate a population of electrons that provides enough energy to dissociate and ionize the input methane gas into its constituent atoms and/or ions. The HPRC uses a Faraday shield with multiple axial slits in order to provide an ion loss area, while at the same time allowing the time-varying RF fields to penetrate the reaction chamber. It was determined that the Faraday shield plays a critical role in preventing carbon soot from building up on the interior of the dielectric reaction chamber. An electron sheath is utilized to provide a high recirculation rate of ions in order to ensure that the exiting neutral particles will have participated in a multitude of dissociation and ionization events. The ratio of the ion loss area (for ions traversing the ion sheath) to that of the exit aperture area (for electrons traversing the

electron sheath) was carefully balanced so that the particle losses within the HPRC were in total non ambipolar flow, resulting in large recirculation rates of ions and consequently a very high degree of decomposition of the input methane. In one operating mode, greater than 99.99±0.06% of the methane injected into the HPRC was decomposed into hydrogen gas and solid carbon. The HPRC in its present proof-of-concept form requires 37× more energy per kg of H_2 produced, compared with steam– methane reformation, though this energy comparison does not include the energy required to sequester the emitted CO_2 during the steam–methane reformation cycle. Based on the trends in the data presented, further efficiency gains are expected from operation at higher RF power densities and higher methane flow rates.

I.4.1. Hydrogen Infrastructure

Hydrogen energy could be used in stationary, portable and mobile applications. Large stationary power plants (~ 250 kW) could produce the electricity supply for buildings; initially this is likely to provide supplementary energy to larger sites such as hospitals, office buildings and factories. If this market succeeds, H_2 could be used gradually for residential areas of small factories (5 – 10 kW). Building regulations would need to be updated for the change of fuel, which could mean a costly modification of the existing infrastructure. Portable applications such as laptop computers and mobile telephones require a lower power output (< 1 kW). This is possible with H_2 fuel cells but the size of the H_2 storage unit and fuel cell stack are likely to make these applications uncompetitive with the existing battery-powered technologies. The automotive market is considered to be the main application for H_2 energy. This transition would require the replacement of current vehicles and infrastructure with those capable of using H_2 as a fuel. The technical challenges of H_2 storage and delivery to the consumer are a major barrier to the widespread use of hydrogen [13]. Being the lightest chemical element, compressed H_2 gas has a very low energy per unit volume of 0.5 kW. h. dm^{-3}, but the highest energy output per unit weight of any substance at 33.3 kW. h. kg^{-1}. The comparisons of the gravimetric and volumetric energy densities of the most common fuels are shown in Table 1.2. For automotive applications, storage of compressed H_2 gas is not feasible in most cases, where available space is insufficient for large H_2 tanks (buses and Lorries being among the exceptions). Consequently, alternative methods for storing hydrogen in a liquid or solid form are being explored. Hydrogen can be stored as a cryogenic liquid in pressurized tanks by super cooling (< -253 °C at 1 bar). This increases the energy density to 2.4 kWh dm^{-3} but this is still relatively low and expensive to implement, since sophisticated insulation is

required for the tanks and energy must be consumed during the compression. Storing hydrogen [14]; as a solid ionic-covalent hydride of light elements such as lithium, boron, sodium, magnesium and aluminum can increase the energy density further. However, solid storage methods must be able to rapidly absorb and desorb hydrogen at close to room temperature and pressure as well as being inexpensive to prepare and resistant to poisoning [15]; conditions that are not met by current solid hydrogen storage methods. The difficulties and cost of H_2 storage make it likely that production sites would need to be widespread to reduce the need for transporting H_2 over long distances [16]. Compressed gas and cryogenic H_2 could be delivered to the locations where it is needed or transported in pipes to fuelling stations or homes, in a similar way to natural gas.

Table: I-1: Gravimetric and volumetric energy content of fuels, excluding the weight and volume of the container.

Fuel	Specific energy (kW h kg^{-1})	Energy density (kg h dm^{-3})
Liquid H2	33.3	2.4
H2 gas (200 bar)	33.3	0.5
Liquid naturel gas	13.9	5.6
Natural gas (200 bar)	13.9	2.3
Petrol	12.8	9.5
Diesel	12.6	10.6
Coal	8.2	7.6
LiBH4	6.2	4.0
Methanol	5.5	4.4
Wood	4.2	3.0
Electricity (Li-ion battery)	0.6	1.7

I.4.2. Methane gas

Methane is the main constituent of natural gas and is naturally abundant in many locations around the world. Natural gas and other fossil fuels are formed over millions of years, deep beneath the Earth's surface. Continued extraction of natural gas could eventually lead to depletion of the current sources. Figure 1-2 shows the geographical distribution of proven reserves of natural gas, The statistic shows the leading countries according to their proved reserves of natural gas from 2008 to 2018. In 2018, Venezuela had proved natural gas reserves of 6.3 trillion cubic meters. Russia has one of the world's largest natural gas reserves, and is a leader in natural gas exports.. Environmental concerns as well as uncertainties surrounding the sustainability and cost of future sources of natural gas have led to considerable interest in alternative methane sources. More informations can be found in [17-30].

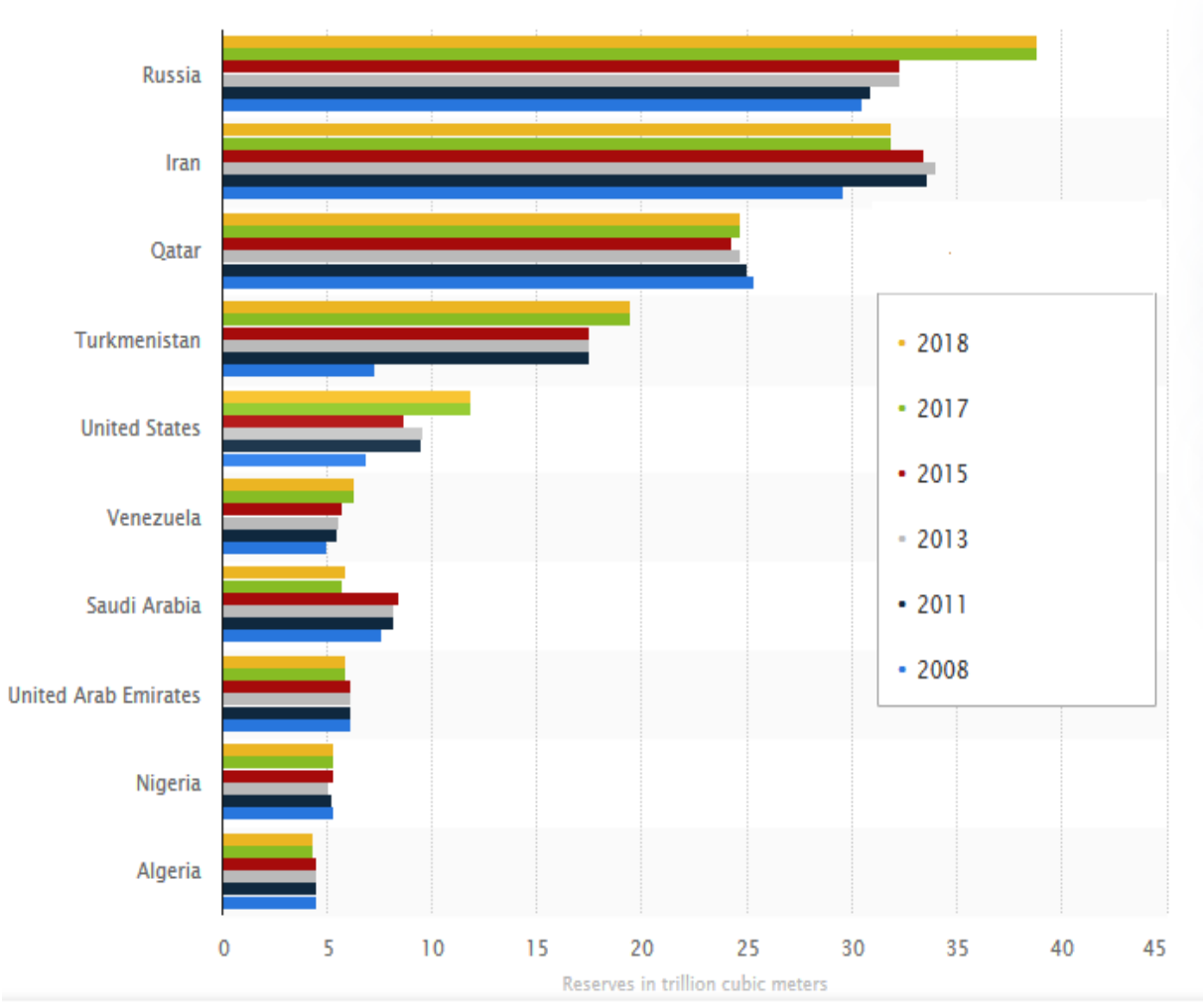

Fig. I-2: Proven world natural gas reserves by geographical region in 2019

Nearly 80% of the world's total proven natural gas reserves are located in ten countries. Russia tops the list, holding about a quarter of world's total gas reserves, followed by Iran and Qatar in the Middle East. From the **Hydrocarbons-technology.com** profiles the top 10 countries with the world's biggest proven gas reserves are:

Russia

Russia holds the largest amount of natural gas reserves in the world. The country was estimated to possess about 1,688 trillion cubic feet (Tcf) of proven gas reserves as of January 2013, accounting for about one fourth of the world's total proven gas reserves. More than half of Russia's gas reserves are located in Siberia. Three of the major Siberian fields, namely Yamburg, Urengoy and Medvezh'ye, account for approximately 45% of the country's gas reserves. The majority of the country's gas reserves under development and production are located in the Nadym-Pur-Taz (NPT) region of upper Western Siberia.

Russia produced 20.916Tcf of natural gas in 2012. The state-run oil and gas company Gazprom dominates upstream gas production in the country. The company accounts for about 80% of Russia's total natural gas output and controls more than 65% of proven gas reserves in the country. Other companies involved in gas production in Russia include Novatek, PSA operators, Lukoil and Rosneft.

Iran

Iran holds the world's second biggest natural gas reserves. Its proved natural gas reserves as of December 2012 stood at 1,187Tcf. Most of these reserves remain undeveloped due to international sanctions and delays in field development. More than 60% of Iran's natural gas reserves are located offshore. Non-associated fields account for around 80% of the country's proven gas reserves. South Pars is the largest gas field comprising 27% of Iran's total proved natural gas reserves and 35% of the country's natural gas output. North Pars, Kish and Kangan are the other major natural gas fields in Iran.

Gross natural gas production of the country in 2012 stood at 8.1Tcf. National Iranian Oil Company (NIOC), through its subsidiaries including National Iranian South Oil Company (NISOC) and Pars Oil & Gas Company (POGC), manages the development and production of natural gas resources in the country. The National Iranian Gas Company (NIGC), another

subsidiary of NIOC, is responsible for natural gas infrastructure, transportation and distribution.

Qatar

Qatar holds the third largest natural gas reserves in the world. Its proven natural gas reserves as of December 2012 were estimated at 885.3Tcf. It accounts for around 13% of the world's total natural gas reserves. Qatar is also the single largest LNG supplier in the world.

A vast majority of the country's natural gas reserves are located in the giant offshore North Field, which covers an area almost equivalent to Qatar itself. North Field is the world's largest non-associated gas field. It is the main source of Qatar's natural gas production. The Barzan gas project, the latest North Field project under construction, is expected to produce an additional 600 billion cubic feet of gas per year upon its completion in 2015.

The gross natural gas production of the country in 2012 stood at 5.7Tcf. The state-owned Qatar Petroleum (QP) is the dominant player in the country's natural gas sector.

The natural gas resources are developed by integrated mega projects in association with foreign players, including ExxonMobil, Shell and Total. QP holds major share in these projects. Qatargas and RasGas are the major LNG companies operating in Qatar.

Turkmenistan

The Central Asian country Turkmenistan holds the world's fourth largest natural gas reserves. The country's proven natural gas reserves as of December 2012 stood at 353.1Tcf. Turkmenistan, however, faces challenges in developing its gas reserves because of far-off end-use markets and a lack of sufficient pipeline infrastructure and foreign investment.

Most of Turkmenistan's proven gas reserves are located in the Amu Darya basin in the south-east and in the Murgab South Caspian basins in the western part of the country. The Dauletabad field in the Amu Darya basin, with estimated gas reserves of 60Tcf, is one of the largest and oldest gas fields in Turkmenistan. The South Yolotan area in the eastern region of Turkmenistan also contains significant gas reserves.

Turkmenistan produced 2.274Tcf of natural gas in 2012. Turkmengaz, one of the five state-run companies for exploration, development, production and distribution of hydrocarbon resources in the country, is responsible for gas production. Russia is the key export market for Turkmenistan natural gas. CNPC of China is the only foreign company directly operating in Turkmenistan with its involvement in Bagtyiarlyk project near the Amu Darya River.

United States of America

The United States ranks as the fifth largest, holding 334.07 Tcf of proven natural gas as of January 2013. The nation's proven gas reserves have steadily increased since 1999 with the expansion of exploration and development activities in its shale formations.

The Barnett play located in Texas and Montana, Haynesville play in the Texas-Louisiana Salt Basin, Marcellus Shale play in the Appalachian Basin, Fayetteville play, Woodford play in Oklahoma and Texas and the Eagle Ford play, in the Western Gulf Basin of South Texas, are the major shale plays contributing to the country's natural gas expansions. Barnett is the largest shale gas reserve in the nation. Other natural gas reserves in the country include the Antrim Shale in Michigan, Caney Shale in Oklahoma, Conesauga Shale in Alabama, Granite Wash Play in Texas and Oklahoma and the onshore and offshore Gulf of Mexico basin.

The US is currently the world's largest producer and consumer of natural gas. It produced 24.06Tcf of natural gas and consumed 25.5Tcf of natural gas in 2012. The country had more than 210 natural gas pipeline systems as of 2012. The interstate and intrastate transmission pipelines exceed 305,000 miles (490,850km) in length.

Saudi Arabia

Saudi Arabia holds the sixth largest natural gas reserves in the world. Its estimated proven natural gas reserves as of December 2012 stood at 290Tcf, including its share of gas reserves in the Saudi-Kuwait Neutral Zone.

Associated gas at the giant oil fields, such as the Ghawar onshore field and the offshore fields Safaniya and Zuluf, account for about 57% of the country's proven gas reserves. The Ghawar field alone accounts for more than 30% of Saudi Arabia's proven gas reserves. Karan gas field, which came online in 2011, is the first offshore non-associated gas field to be developed

in Saudi Arabia. Other major non-associated gas fields under development are the Arabiyah and Hasbah gas fields.

Gross natural gas production in Saudi Arabia in 2012 stood at 3.927Tcf. The country does not import or export natural gas. Its entire gas output is consumed domestically. The state-owned Saudi Aramco is responsible for gas production in the country. The company has partnered with foreign companies such as Lukoil, Sinopec, Eni and Respol for exploring non-associated onshore gas resources especially in Rub al-Khali, the world's largest sand desert.

United Arab Emirates

The United Arab Emirates (UAE) has the seventh biggest gas reserves in the world. The country's proven natural gas reserves as of December 2012 were estimated at 215.1Tcf. Despite the vast gas reserves the country imports natural gas, primarily from Qatar. The UAE imported 616 billion cubic feet of gas in 2011. Around 30% of UAE's gas output is re-injected into oil fields. The power sector of the country too uses natural gas as a major feedstock.

About 94% of the country's proven natural gas reserves are located in Abu Dhabi. Sharjah and Dubai account for four percent and 1.5% of UAE's total gas reserves respectively. The development and processing of the UAE's gas reserves are economically challenging as most of the country's natural gas has relatively high sulphur content.

The UAE's gross natural gas production in 2012 stood at 3Tcf. Individual emirates manage gas production in their respective territories. ADNOC, through its subsidiaries ADCO and ADMA-OPCO, carries out exploration and production of gas resources in Abu Dhabi. The Abu Dhabi Gas Industries (GASCO), a joint venture between ADNOC, Shell, Total and Partex, is responsible for processing onshore natural gas in the country. Abu Dhabi Gas Liquefaction (ADGAS) manages the production and export of liquefied natural gas (LNG) and liquefied petroleum gas (LPG).

Venezuela

Venezuela, the world's biggest oil reserves holding country, possesses the eighth largest gas reserve. The proven natural gas reserves of the country were estimated at 195Tcf as of December 2012. Associated gas accounts for nearly 90% of Venezuela's natural gas reserves.

The country plans to increase its natural gas production up to 14 billion cubic feet per day by 2015.

The existing onshore fields such as Anaco, Barrancas and Yucal Place are being developed for increased gas production. Plataforma Deltana, Marsical Sucre and Blanquilla-Tortuga areas off the north-east coast of Venezuela, and the gas blocks in the Gulf of Venezuela in the north-western part of the country are being developed with involvement of foreign companies including Total, Statoil, Chevron and Gazprom.

The country produced 1.137Tcf of natural gas in 2012. A large share of the country's gas output is re-injected into the oil fields for better crude oil extraction. Venezuela currently imports gas from Colombia and the US in order to meet its growing industrial demand.

Nigeria

Nigeria holds the ninth largest gas reserves in the world. The largest oil producing African country was estimated to contain 182Tcf of proven natural gas reserves as of December 2012. Most of natural gas reserves of the country are located in the Niger Delta. Nigeria produced 1.525Tcf of natural gas in 2012.

Amenam-Kpono, Bonga and Akpo are the major oil and gas fields located in Niger Delta. Gbaran-Ubie, one of the latest integrated oil and gas projects in the country, achieved peak production of one billion cubic feet per day in 2011. Much of the country's natural gas is flared since most of the oil fields lack the infrastructure to produce and market associated natural gas.

Shell is the leading gas producer in the country. It's Soku gas-gathering and condensate plant provides nearly half of the feed gas to the only LNG facility of Nigeria. Total, Eni and Chevron are among the other major foreign companies involved in Nigerian gas production. The Nigerian Gas Company (NGC), a subsidiary of Nigerian National Petroleum Corporation (NNPC), is responsible for the marketing, transmission and distribution of gas. Most of Nigeria's marketed natural gas is exported as LNG.

Algeria

Algeria's gas reserves rank as the tenth biggest in the world. It is also the largest gas producing country in Africa. The proven natural gas reserves of the country were estimated at 159.1Tcf as of December 2012. Algeria's gas production has, however, declined in the recent years with the depletion of some of its mature gas fields.

More than half of Algeria's proven natural gas reserves are contained in the country's largest gas field, Hassi R'Mel. Associated and non-associated fields in the south and south-east regions of the country comprise the remaining gas reserves of the country. Rhourde Nouss, Alrar and Hamra are among the other largest mature gas fields in the country.

The country produced 2.875Tcf of natural gas in 2012. Sonatrach is the leading gas producing company in the country. Other companies involved in gas production in Algeria include Eni, BP, Repsol, GDF Suez and the BG Group. A host of new gas projects including Gassi Touil, In Salah Expansion, Reggane Nord, Timimoun and Touat are under development in the country. Menzel Ledjimet East (MLE), which commenced production in 2013, is the latest gas project to be developed in the country.

I.4.2.1. Chemical and Physical Properties of Methane

The carbon atom central to the methane molecule has 4 valence electrons and thus needs 4 more electrons from four hydrogen atoms to complete its octet. The hydrogen atoms have a 109 degree bond angle giving the molecule a tetrahedral geometry. A principal component of natural gas, methane is significant. Burning one molecule of methane in the presence of oxygen releases one molecule of CO_2 (carbon dioxide) and two molecules of H_2O (water):

$$CH_4 + 2O_2 => CO_2 + 2H_2O \quad \text{(I-1)}$$

The strength of the carbon hydrogen covalent bond in the methane molecule is among the strongest in all hydrocarbons, and thus its use as a chemical feedstock is limited. The search for which one can facilitate C-H bond activation in methane and other low alkanes is an area of research with considerable industrial significance [17].

Pure methane is odorless, but when used as a fuel it is usually mixed with small quantities of strongly-smelling sulfur compounds such as ethyl mercaptan to enable the detection of

leaks. Methane is a greenhouse gas with a global warming potential of 22 (meaning that it has 22 times the warming ability of carbon dioxide). Methane results from the decomposition of certain organic matters in the absence of oxygen. It is therefore also classified as a biogas.

The U.S. Geological Survey has estimated that the United States has 320,000 trillion cubic feet of gas hydrates, some 200 times conventional natural gas resources and reserves in the country. If only 1 percent of the methane hydrate resource could be made recoverable, the United States could more than double its domestic natural gas resource base Principal sources of methane are: decomposition of organic wastes ; natural sources (marshes) : 23 % fossil fuel extraction : 20 % Coal bed methane extraction the processes of digestion of animals (cattle) : 17 % bacteria found in rice plantations : 12 % biomass anaerobic heating or combustion 80% of the world emissions are of human source. They come primarily from agricultural and other human activities. During the past 200 years, the concentration of this gas in the atmosphere doubled, passing from 0.8 to 1.7 ppm.

I.4.2.2. Methane as a Fuel

Methane is important for electrical generation by burning it as a fuel in a gas turbine or steam generator. Compared to other hydrocarbon fuels, burning methane produces less carbon dioxide for each unit of heat released. At about 891 kJ/mol, methane's heat of combustion is lower than any other hydrocarbon but the ratio of the heat of combustion (891 kJ/mol) to the molecular mass (16.0 g/mol, of which 12.0 g/mol is carbon) shows that methane, being the simplest hydrocarbon, produces more heat per mass unit (55.7 kJ/g) than other complex hydrocarbons. In many cities, methane is piped into homes for domestic heating and cooking purposes. In this context it is usually known as natural gas, which is considered to have an energy content of 39 mega joules per cubic meter, or 1,000 BTU per standard cubic foot.

Methane in the form of compressed natural gas is used as a vehicle fuel and is claimed to be more environmentally friendly than other fossil fuels such as gasoline/petrol and diesel. Research into adsorption methods of methane storage for use as an automotive fuel has been conducted.

Liquefied natural gas (LNG) is natural gas (predominantly methane, CH_4) that has been converted to liquid form for ease of storage or transport.

Liquefied natural gas takes up about 1/600th the volume of natural gas in the gaseous state. It is odorless, colorless, non-toxic and non-corrosive. Hazards include flammability after vaporization into a gaseous state, freezing and asphyxia.

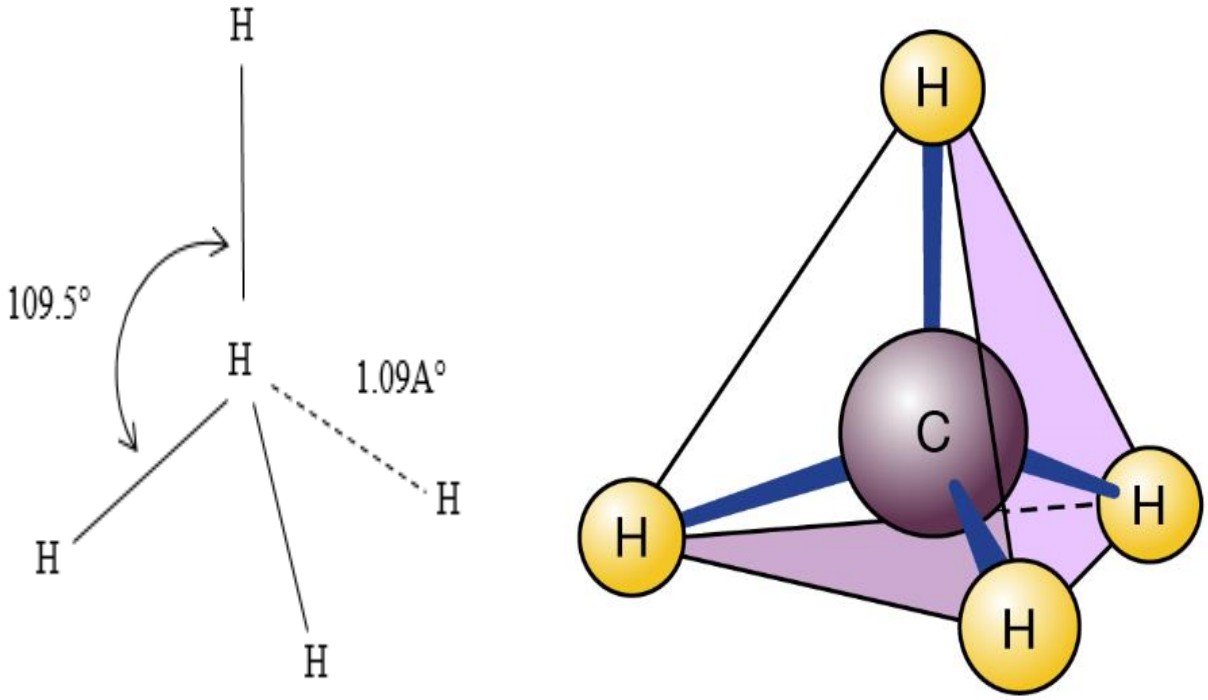

Fig. I-3: Methane molecule structure

The liquefaction process involves removal of certain components, such as dust, acid gases, helium, water, and heavy hydrocarbons, which could cause difficulty downstream. The natural gas is then condensed into a liquid at close to atmospheric pressure (maximum transport pressure set at around 25 kPa or 3.6 psi) by cooling it to approximately −162 °C (−260 °F).

I.5. Hydrogen Energy

The depletion of fossil fuel reserves and the adverse effects of global climate change have led to the emergence of several new energy technologies in recent years. One of which, is the use of H_2 as an energy carrier that can be used to generate electricity by combustion in an internal combustion engine (ICE) or by the use of fuel cells, where chemical energy is converted into electricity using an electrochemical cell. Hydrogen and fuel cells are seen by

many as key solutions for the 21st century, enabling clean efficient production of power and heat from a range of primary energy sources. The latter is favorable, particularly for automotive applications, given that the transfer of chemical energy associated with fuel cells is more efficient than methods of combustion where loss of energy as heat is inevitable.

Like electricity, hydrogen is an energy carrier (not an energy source), meaning it can store and deliver energy in an easily usable form. Although abundant on earth as an element, hydrogen combines readily with other elements and is almost always found as part of some other substance, such as water (H_2O), or hydrocarbons like natural gas (which consists primarily of methane, with the chemical formula, CH_4). Hydrogen is also found in biomass, which includes all plants and animals [31]. Additionally, the use of H_2 as a fuel for ICEs would result in emissions of nitrogen oxides (NO_x) due to the combustion of hydrogen-air mixtures, thus fuel cells are preferable in terms of a cleaner air quality. The oxidation of hydrogen produces zero harmful emissions; H_2O is the only byproduct of both ICE and fuel cell applications. However, for H_2 to be considered as a clean source of energy it should be derived from renewable sources and not from fossil fuels. As with any fuel, issues of safety must be addressed prior to endorsement. H_2 is a flammable gas over a wide range of concentrations (4–75%) and burns with a colorless flame. The ignition temperature of H_2 is higher than petroleum derived fuels and if allowed to leak, H_2 will quickly rise and disperse, lessening the risk of fire. Overall, safety concerns do not prevent the use of H_2 as a fuel.

When it comes to selection the right fuel [32]; Dinçer and Biçer [33] donated the fundamental requirements of air vehicle fuels, and listed the properties of air vehicle fuels as;

- High levels of maximum range or payload heat. This indicates a high specific energy and high energy density.
- Good atomization, rapid evaporation, good burning properties, including the ability to lower high and low risk of explosion.
- High specific heat capacity, pollution-free, low carbon formation.
- Low viscosity and high lubricity, good characteristics of pumped storage, including low freezing point, in order to facilitate the operation amount.
- High stability thermal/chemical stability, wide availability and price acceptable and respects the environment.
- Proper ground and handling characteristics.

I.5.1 Proton Exchange Membrane (PEM) Fuel Cells

A fuel cell is essentially a compact electrochemical "factory" that takes fuel as input and produces electricity as output. Like a factory, a fuel cell will continue to turn out product (electricity) as long as raw material (fuel) is supplied.

Fuel cell technology is expected to play an important role in meeting the growing demand for distributed generation [34].

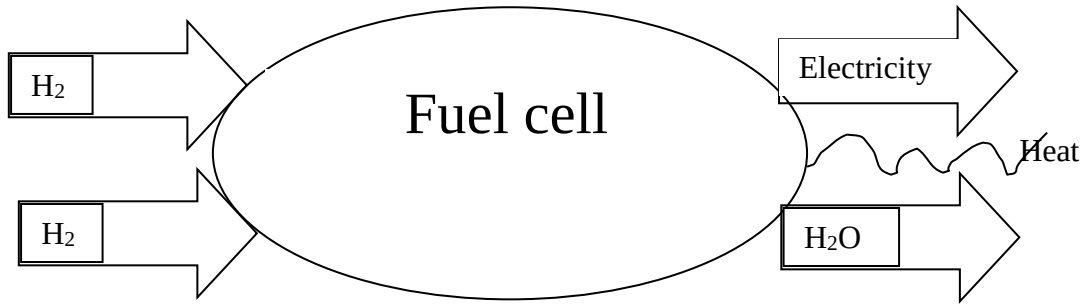

Fig. I-4: Schematic diagram of a PEM fuel cell principal function.

The basic components of a PEM fuel cell are the anode, cathode and a proton exchange membrane sandwiched between layers of catalysts, as shown in Figure I-5. The Proton Exchange Membrane Fuel Cell (PEMFC) is considered a key device in the so-called "hydrogen based energy system" which is a promising alternative to the current fossil fuels based energy system. In the PEMFC, hydrogen (H2) reacts with oxygen (O2) producing electrical energy, heat and water [35].

At the anode, H2 is oxidized and the resulting protons diffuse through the PEM layer. At the cathode, O2 from air is reduced to form H2O. The electrons released travel around an external circuit, providing electricity to the load. The PEM is most commonly a Nafion-based polymeric electrolyte. The membrane has hydrophilic pores of ~ 10 nm in size, which allows the passage of H+ ions only through the membrane. The oxidation and reduction reactions in the fuel cell are promoted by Pt-based catalysts, which are more efficient at higher temperatures. However, the proton-conducting channels in the membrane are also strongly temperature dependent, with high temperatures causing the pore size to shrink, hindering the proton exchange mechanism. These factors limit PEM fuel cells to working temperatures in the range of 80 – 100 °C; this requires the use of efficient cooling systems to prevent overheating of the cells. At these relatively low temperatures, any CO impurities (as low as 50 ppm) in the H2 feed can cause poisoning of the catalysts due to a strong adsorption affinity of

CO towards the Pt catalysts. Therefore, the purity of H2 is critical for the operation of PEM fuel cells.

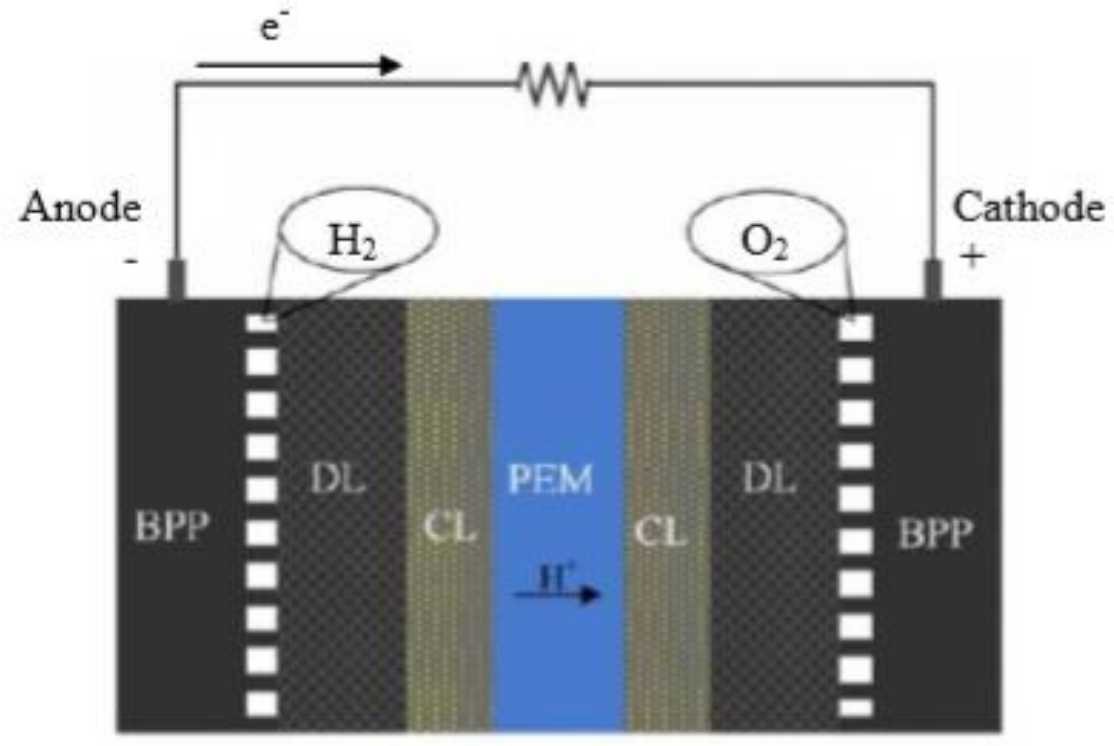

Fig. I-5: Schematic diagram of a PEM fuel cell, CL = catalyst layer, DL = diffusion layer and BPP = bipolar plat.

To amplify the power generation from fuel cells, several units are arranged in series to form a fuel cell stack as illustrated in Figure I-5, where three fuel cell units are integrated, sandwiched between bipolar plates. The bipolar plates act as gas separators between the adjacent cells and must be electrically conductive to assist the flow of current around the integrated circuit. Increasing the number of individual fuel cell units can allow the generation of several hundred volts of electricity. Several leading car manufacturers have developed PEM fuel cell technologies that are sufficiently advanced to be able to power motorized vehicles at acceptable speeds over a 300 mile range, meeting the criteria for commercial vehicles.

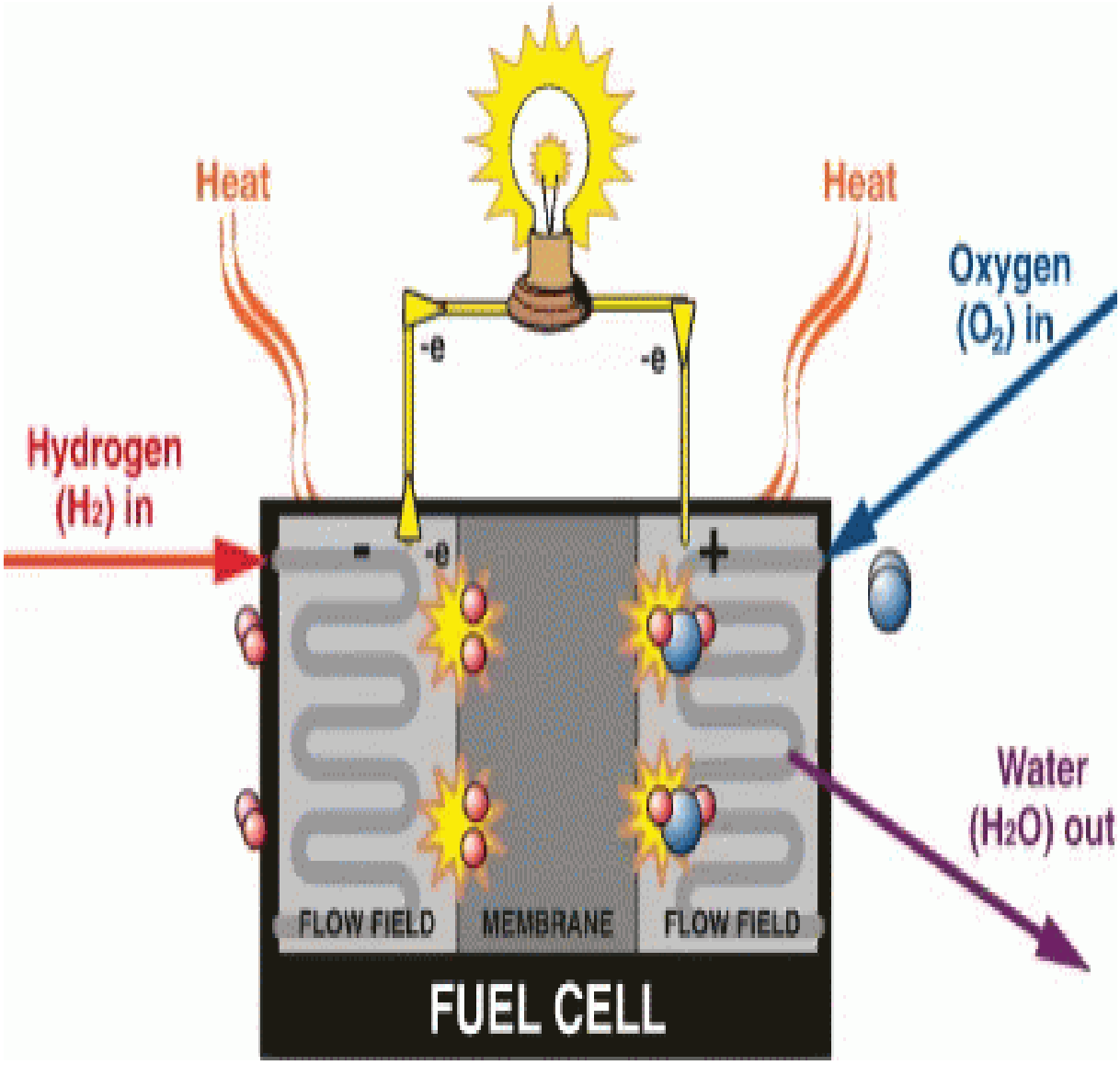

Fig. I-6: Schematic diagram principal function of fuel cell.

The low operating temperatures offer a rapid response, which enables acceptable acceleration and braking to be met. In addition, PEM fuel cells have been reported as 2 – 3 times more energy efficient than the currently employed petrol or diesel ICEs. Several works interested to the study and develop this devie like [34-44].

Sincere attempts are being made world-wide for largescale commercialisation of PEMFCs, and significant advances have indeed been made. In spite of these advances, however, large-scale commercialisation of PEMFCs is still restricted because the materials used (such as ionomer materials and platinum-based catalysts) are expensive and the reliability of the devices is low.

I.6. Conclusion

Global energy demand is growing drastically because energy plays a very important role in our daily lives and socio-economic development. All non-renewable energy resources (fossil fuel) oil, coal and natural gas and renewable energies (solar, wind, hydro, and geothermal) and nuclear energy are envisaged to allow the production of hydrogen.

Hydrogen is currently produced either by electrolysis of water or by thermo-chemical methods such as hydrocarbons or reforming methane, partial oxidation of methane with oxygen and auto-thermal reform, The purpose of this study shows that the cold plasma technologies can produce through methane for different type of discharge. Through this thesis, we will have the opportunity to know the possibility of hydrogen production by using capacitively and inductively Coupled Plasma in methane.

CHAPTER: II

PRELIMINARY CONCEPTS ON COLD PLASMA DISCHARGE

II.1. Introduction

The term "plasma" was proposed by Langmuir in 1929 to describe an ionized gas. In ascending order on the temperature scale, plasmas represent the fourth state of matter after the solid, liquid and gaseous states. More specifically, plasma is a partially or totally ionized gas, consisting of a generally electrically neutral assembly, comprising electrons, positive and negative ions, atoms and molecules. As examples, we can mention, on the one hand, so-called natural plasmas such as flames, the solar corona, nebulae, lightning and aurora, and, on the other hand, so-called industrial laboratory plasmas created in a reactor and maintained by a source of electrical energy. In this chapter, we give a brief reminder about plasmas and their physical properties. Subsequently, we present the different types of existing plasmas as well as the possible collisions in the plasma. Finally, we draw up a state of the art of plasma sources operating at low pressure and at atmospheric pressure for different excitation sources, as well as their fields of application.

II.2. Description of the particles present in a cold plasma

Plasma is a medium composed of stable or excited neutral species (molecules, molecular fragments, atoms) and charged species (electrons, positive or negative ions), so that the whole is free to move in all space directions.

II.2.1 Stable neutrals and Molecular fragments

The neutrals species is the primary sources of plasma ; in order to convert gas « neutral state » into a plasma state it is necessary to to tear away at least some of the electron from the neutrals [6]. The molecular fragments can be either simple atoms (H, N, O, etc.), or more complex molecular edifices among which the radicals of traditional chemistry (CH_3, CH_2, CH, OH, O_3, etc.). The radical term refers to a molecular fragment whose peripheral number of electrons is odd, (for example NO, CH_3, OH, etc.) with pendant bonds that make it very reactive in collisions with other species.

II.2.2 Electrons

Free electrons are the real driver of electric discharge. Because of their very low relative mass, they move much faster than other species and are therefore the first to store energy from the electric field which will then allow them to excite, dissociate and ionize the gaseous

medium. Electrons actually respond to electromagnetic disturbances on timescales 100 to 1000 times shorter than ions. It is also the electrons that, because of their high mobility, are primarily responsible for the electrical conductivity of plasmas.

II.2.3 Positive and negative ions

A ion is defined to be an atom or molecule carrying an electric charge, in particular having won or lost one or more electrons. Generally, the ionization in a cold plasma is due to the electronic impact collision.

II.2.4 Excited states

An atom or a molecule can see, following an excitation, one of its electrons placed on a more energetic orbital. The species is then excited electronically and also the electronic energy levels are quantified. The energy of these levels is several electronvolts. An electronically excited species can range from a lower level to another higher energy absorbing one. In the opposite case, the passage from the upper level to the lower optically permissible level is an excitation which allows the emission of a photon whose energy corresponds to the energy difference between the two levels. The excited species can be:

Rotational excitation: Molecular species can acquire rotational energy. This energy is quantified; the energy jump between levels is low, of the order of 0.01 eV.

Vibration excitation*:* This type of excitation corresponds to a periodic deformation of the molecular structure. One can, in a simplistic way, distinguish between the elongation vibration of a chemical bond and the angular torsional vibrations of two bonds. Here again the molecule can pass from one energy state to another state only by a quantum leap. The order of magnitude of these energy jumps is 0.1 eV.

Electronic excitation: An atom or a molecule can see, following an excitation, one of its electrons placed on a more energetic orbital. The species is then excited electronically and also the electronic energy levels are quantified. The energy of these levels is several electronvolts. An electronically excited species can range from a lower level to another higher energy absorbing one. In the opposite case, the passage from the upper level to the lower optically permissible level is an excitation which allows the emission of a photon whose energy corresponds to the energy difference between the two levels. The electronic excited

species can be in a radiative state which disappears by spontaneous emission in a few hundred nanoseconds or a metastable excited state having a much longer life and usually disappears by collisions that often play an important role in the maintenance of the discharge such as step ionization or ionization Penning or the excitement of Rydberg's levels, etc.

Photons: Photons are most often emitted by de-excitation of the electronic states, so they are well defined energy or line spectra. Our electric discharges can emit photons in a broad spectral band going from the UV until the visible one even infra-red. These spectra, characteristics of the emitting species are therefore carriers of information on the composition of the plasma and are used to characterize the plasma, for example by emission spectroscopy. The amount of photons emitted by the plasma can represent a significant part of the energy dissipated in the discharge. Photons may also influence the chemistry of radiation discharge from gases or surfaces for photochemistry, photobiology or photo-catalysis applications. This is especially true for the VUV component.

II.3. Characteristic quantities of the plasma

II.3.1. Species densities

The density of a given species represents the number of particles contained on average per unit volume around a given space point and at a given moment. Densities are often expressed in cm^{-3} or m^{-3}. In cold plasma, the densities to be determined are the electron density n_e, the density of the positive ions n_i^+, the density of the negative ions n_i^-, the density of the neutrons n_0 and the density of the radicals n_r, and the excited state density n_o^*.

II.3.2. Degree of ionization, dissociation, excitation

The plasma ionization degree τ_i is directly given by: $\tau_i = n_i /(n_i + n_r + n_0)$. It is the ratio of the density of ions to the total density (neutrals density + radicals density + ions density).

The dissociation degree τ_d is defined as the ratio of the density of the fragments (radicals) to the sum of the radicals density and the neutrals density, is given by $\tau_d = n_r /(n_r + n_0)$.

Finally, the excitation degree τ^*, which given by $\tau^* = n^* /(n^* + n_0)$. It is defined as the ratio of the density of the excited particles to the sum of the density of the excited particles

and the density of the neutrals. In the cold plasmas, all these degrees naturally remain well below to 1, generally in the order of 10^{-5} to 10^{-4}.

II.3.3. The macroscopic quasi-neutrality

The quasi-neutrality criterion indicates that a plasma is globally electrically neutral, that is, there are as many positive as negative charges. For plasma consisting of a density of positive ions charged n_i and of electrons of density n_e then we have the relation:

$$\left|\frac{n_e - n_i}{n_e + n_i}\right| \ll 1 \qquad \text{(II-1)}$$

where n_i and n_e are: the ions and the electrons densities, respectively. Virtually neutrality comes in particular from the conservation of the electric charge during ionization processes. This property is observed in the case where the plasma dimensions are much larger than the Debye sphere.

II.3.4. Debye length

It has been seen that the plasma is by definition a medium in which the densities of electrons and ions are sufficiently large that the electric forces associated with these charges maintain a macroscopic neutrality of the medium. More precisely, a plasma medium can support a non-neutrality but only on dimensions whose order of magnitude is fixed by the Debye length. We understand intuitively that the length of Debye is even lower than the plasma density is large, and increases with the temperature of the charged particles. The length of Debye electronics is given by:

$$\lambda_D = \sqrt{\frac{\varepsilon_0 k_B T_e}{e^2 n_e}} \qquad \text{(II-2)}$$

where ε_0 is vacuum permittivity, n_e is the electrons density, T_e is the electron temperature, k_B is the Boltzmann constant, and e is the electron charge.

II.3.5. The mean free path

It is the average distance traveled by a moving species in plasma between two successive collision impacts modifying its direction, its energy or other properties. This quantity is calculated by:

$$\lambda = \frac{1}{n_0 \sigma} \tag{II-3}$$

where n_0 is the neutral density and σ is the cross section. Generally, the cross section depends on the electrons energy.

II.3.6. Landau Length

The length of Landau is the distance for which the potential energy of interaction between two electrons is equal to their kinetic energy of thermal agitation. This distance is given by the following expression:

$$\lambda_L = \frac{e^2}{4\pi\varepsilon_0 k_B T_e} \tag{II-4}$$

where ε_0 is vacuum permittivity, T_e is the electron temperature, k_B is the Boltzmann constant, and e is the electron charge.

II.3.7. Plasma potential

The average electrostatic potential in the plasma is well defined; it is approximately constant in the volume of the plasma in the case of plane-plane geometry. It can be defined from the energy required to transport a particle charged from the plasma to the point where the potential is zero. In general, the plasma potential is greater than the surrounding walls.

II.3.8. Plasma frequency

The collective behavior of plasmas occurs when the plasma is separated from the equilibrium for which densities of charged particles are spatially homogeneous. The medium then returns to equilibrium by oscillating at the electronic plasma frequency.

The plasma frequency is given by the following expression:

$$\omega_p = \sqrt{\frac{e^2 n_e}{\varepsilon_0 m_e}} \tag{II-5}$$

where ε_0 is vacuum permittivity, m_e is the electron mass, n_e is the electrons density, and e is the electron charge.

II.3.9. Distribution function

For a better description of plasma, the distribution function $f(r,v,t)$ is defined; this describes the energetic states of particles especially their speed distribution.

This equation, $f(r,v,t)$, is the solution of the Boltzmann equation which describes the variation of the species kinetics in the plasma, it is valid for weakly ionized plasmas, governed by the collisions between neutral species and charged particles.

The distribution function gives the average number of particles of type s and mass m_s which are in an elementary volume dr^3 around a point r whose extremities of the velocity vector are in a volume of the velocity space dv^3. At thermodynamic equilibrium, the distribution function of velocity is Maxwellian:

$$f_s(r,v,t) = n_s(r,t)\left(\frac{m_s}{2\pi k_B T}\right)^{3/2} \exp\left(-\frac{m_s v^2}{2 k_B T}\right) \quad \text{(II-6)}$$

where k_B is the Boltzmann constant, T is the temperature and $n_s(r, t)$ is the density of the particles of type s around the point r and at time t. The Maxwellian energy distribution function, which corresponds to the number of particles whose energies lie between ε and $\varepsilon+d\varepsilon$, is written as follows:

$$f_s(r,\varepsilon,t) = n_s(r,t)\frac{2}{k_B T}\left(\frac{\varepsilon}{\pi k_B T}\right)^{1/2} \exp\left(-\frac{\varepsilon}{k_B T}\right) \quad \text{(II-7)}$$

Once this distribution function is known, we can easily calculate [45]:

The density

$$n_s = \iiint f_s dv^3 = \int_0^{\infty} 4.\pi.v^2.f_s dv \quad \text{(II-8)}$$

The mean velocity

$$\bar{v} = \frac{1}{n_s}\iiint v f_s dv^3 = \frac{1}{n_s}\int_0^{\infty} 4.\pi f_s v^3 dv = \left(\frac{8\,k_B T}{\pi\, m_s}\right)^{1/2} \quad \text{(II-9)}$$

The most probable velocity

$$v_{pp} = \frac{d}{dv}\left[4\pi v^2 f_s(r,v,t)\right] = \left(\frac{2\,k_B T}{m_s}\right)^{1/2} \quad \text{(II-10)}$$

Root Mean Square Velocity

$$V_{RMS} = \frac{1}{n_s}\sqrt{\iiint v^2 f_s dv^3} = \frac{1}{n_s}\sqrt{\int_0^\infty 4.\pi v^4 f_s dv} = \left(\frac{3k_B T}{m}\right)^{1/2} \quad \text{(II-11)}$$

Mean Kinetic energy

$$\begin{aligned}\varepsilon_c &= \frac{1}{n_s}\frac{1}{2}m_s \iiint f_s\left(v - \bar{v}\right)^2 dv^3 \\ &= \frac{1}{n_s}\frac{1}{2}m_s \int_0^\infty 4.\pi.v^2 f_s\left(v - \bar{v}\right)^2 dv = \frac{3}{2}k_B T\end{aligned} \quad \text{(II-12)}$$

The most probable energy

$$\varepsilon_{pp} = \frac{d}{d\varepsilon}\left[\left(\frac{4\varepsilon}{\pi\left(k_B T\right)^3}\right)^{1/2}\exp\left(-\frac{\varepsilon}{k_B T}\right)\right] = \frac{1}{2}k_B T \quad \text{(II-13)}$$

The particle flow

$$\phi = \iiint_{\vec{u}.\vec{v}>0} f_s\, \vec{v}.\vec{u}\, dv^3 \quad \text{(II-14)}$$

Reaction rate

$$\begin{aligned}R_{su} &= \iiint\iiint v_r.\sigma\left(v_r\right).f_s.f_u.dv_u{}^3.dv_s{}^3 \\ &= n_s.n_u\sqrt{\frac{2}{\pi}}\left(\frac{\mu}{k_B T}\right)^{3/2}\int_0^\infty v_r{}^3.\sigma(v_r).\exp\left(-\frac{\mu v_r{}^2}{2k_B T}\right).dv_r\end{aligned} \quad \text{(II-15)}$$

Reaction rate constant

$$k_{su} = \left\langle\sigma(v).v\right\rangle = \frac{R_{su}}{n_s.n_u} \quad \text{(II-16)}$$

Reaction frequency

$$\upsilon_{su} = n_s\left\langle\sigma(v).v\right\rangle = n_s.k_{su} \quad \text{(II-17)}$$

II.4. Description of reactions in a non equilibrium cold plasma

In this paragraph we will describe and classify some important reactions that occur in our reactive plasmas. The cold plasma is an active field for different reactions, the primary reactions are started by the electronic impact collision because of the electrons are the first to store energy from the source of energy (can be electric field, magnetic field, electromagnetic field, etc.).

In this section we give a fast description with examples of reactions happened in the plasma, and we will detailed these kinds in the chapters III for the methane gas.

II.4.1. Primary reactions

Since electrons are the first to the primary reactions are inelastic collisions between electrons and the neutrals of background-state (bulk plasma). All these primary inelastic collisions have a threshold in energy, the electrons must have an energy higher than this threshold to give rise to the reaction. After the collision, the electron loses the threshold energy. To maintain the electrical discharge, these losses of energy are compensated by the action of the electric field which constantly transfers energy to the electrons.

Ionisation

Exemple : $e + CH_4 \rightarrow CH_4^+ + 2e$

Ionisation dissociative

Example : $e + CH_4 \rightarrow H_2 + CH_2^+ + 2e$

Excitation

Example : $e + CH_4 \rightarrow CH_4^* + e$

Dissociative attachment

Example : $e + CH_4 \rightarrow CH_3 + H^-$

These inelastic collisions may possibly be followed by dissociation and / or emission of a photon.

Example : *Radiative deexcitation* $CH_4^* \rightarrow CH_4 + h\upsilon$

Dissociation $CH_4^* \rightarrow CH_2 + H_2$

Dissociative Emission $CH_4^* \rightarrow CH_2 + H_2 + h\upsilon$

All these primary inelastic collisions have a threshold in energy; the electrons must have an energy higher than this threshold to give rise to the reaction. After the collision, the electron loses the threshold energy. To maintain the electrical discharge, these losses of energy are

compensated by the action of the electric field which constantly transfers energy to the electrons.

II.4.2. Secondary reactions

Side reactions are more diverse and have a longer time scale than primary electronic reactions. They include all reactions between an unstable species more or less directly from a primary reaction and gas, this lead to the formation of new species. Some examples are given below:

Ion – molecule Reaction

Example : $CH_5^+ + CH_2 \rightarrow CH_3^+ + CH_4$

$CH_4^+ + CH_4 \rightarrow CH_5^+ + CH_3$

$CH_3^+ + CH_4 \rightarrow C_2H_5^+ + H_2$

$CH_2^- + CH_3 \rightarrow C_2H_5 + e$

$H^- + CH_4 \rightarrow H + CH_4$

Radical – molecule Reaction

Example : $CH + CH_4 \rightarrow C_2H_4 + H$

Associative Collision Detachment

Example : $C_2^- + H_2$ --- > $C_2H_2 + e.$

Dissociative recombination

Example : $e + O_2^+ \rightarrow O + O$

Detachment by electronic impact

Example : $e + O^- \rightarrow O + 2e$

Reactions between the radicals

Example : $CH_3 + CH_2 \rightarrow C_2H_4 + H$

Collision super-elastic

Example : $e + CH_4^* \rightarrow CH_4 + e$

Excitation of a radical

Example : $e + CH_4 \rightarrow CH_4^* + e$

II.4.3. Reactions with the wall (surface reaction)

The walls and surfaces may be subject to a flow of particles and various chemical species. In this case, they are the seat of a large number of reactions that can result either in a chemical modification of the surface (recombination, passivation, oxidation, nitriding, etc.), or in an erosion of the wall (etching), or finally in thin film formation (deposit). In non-equilibrium cold plasmas at low pressure (in the order of mtorr), recombination reactions at the surface are more important than recombination reactions in the gaseous volume.

II.5. plasmas Classification

Artificial plasmas are currently used in a large number of applications and industrial processes because they make it possible to obtain reactions in the gas phase or with surfaces that would be difficult to achieve by other methods. The use of plasma-assisted processes represents a multibillion-euro market growing steadily. To change to the plasma state, it is necessary to supply the gas with a quantity of energy sufficient to ionize atoms and molecules. Energy input can be in the form of heat (heating), light (laser) or electric (by application of an electric field). Among the artificial plasmas we can distinguish three categories:

II.5.1. Hot plasmas

Studied in the context of civil applications for thermonuclear fusion energy production (fusion by magnetic confinement in tokamaks), or military applications to reproduce thermonuclear explosions (fusion by inertial confinement), or as an intense source of X-ray radiation (Z-pinch). They are totally ionized (τ_i = 1) and the charged species are at very high temperatures of the order of the MeV.

II.5.2. Thermal plasmas

Thermal processes are typically high pressure processes in which the plasmas are in thermodynamic equilibrium (temperatures of the order of the electronvolt). Their main fields

of application are metallurgy (welding and cutting by plasma torch), thermal spray surface coating, plasma torch waste treatment or high intensity lighting (electric arc lamps, etc.).

II.5.3. Cold plasmas

Out of thermodynamic equilibrium, for which the electronic temperature is of the order of a few electronvolts while the neutral ions and species are at ambient temperature. These plasmas are little ionized and can exist at high pressure as at low pressure. The latter have many applications in process engineering for surface treatment (polymerization, nitriding, cementation, ion implantation, deposition and dry etching etc.). The manufacturing processes in microelectronics are therefore widely used for the manufacture of integrated circuits, memories, microprocessors and so on. The manufacturing techniques for flat screens, solar panels or thin-film transistors also rely on plasma processes. Finally, cold plasmas are also used in lighting (fluorescent lamps, luminous signs), in depollution (manufacture of ozone from oxygen in the air, treatment of gaseous effluents).

II.6. Radio Frequency (RF) discharges

Radio Frequency (RF) discharges are discharges operating with an excitation whose frequency range between 1 and 200 MHz, the range in which the electrons respond instantaneously to the variations of the electric field whereas the ions are sensitive only to the average time value of the sheath field.

They are widely used in many field of applications such as thin film processes (PECVD) and microelectronics industry [46-50]. In the radio frequency range, the value of 13.56 MHz is generally used as the excitation frequency or one of its harmonics (27.12 et 40.68, 54.24 MHz, etc.); these values are imposed by international telecommunication regulations with which a certain amount of energy can be emitted without interfering with telecommunications signals.

II.6.1. The coupling of RF excitation

The geometry of the reactor depends on the treatment process envisaged. The coupling between the reactor and the power supply can be by connecting directly the generator to one of the electrodes, or is isolated there from by the presence of a coupling capacitor (capacitive coupling), the second way is to create RF electromagnetic excitation by the circulation of an

alternating current in a conductive coil. The coil is separated from the plasma by a dielectric electrode (inductive coupling).

The impedance adaptation makes it possible to optimize the transfer of energy to the ionized medium by equalizing the output and input impedances of the reactor; this depends on the pressure, the type of gas excited or the type of coupling used.

II.6.2. The main axes of digital modeling of RF discharges

The complexity of the phenomena involved and their coupling makes it extremely difficult to describe the discharge in its entirety. A complete model will have to describe, for example, the transport of the charged particles in the electric field, the kinetics of the neutrons as well as the surface reactions taking into account a real representation of gas flow, its heating, the modification of its chemical composition, the interaction of charged particles with the walls, the influence of the particles sprayed and the external electric circuit. For simplicity, the modeling of a real RF reactor can be divided into three large coupled parts: electrical modeling, kinetic and hydrodynamic modeling and surface reaction modeling. In this part we only deal with the electrical modeling of RF discharges. It provides a self-consistent description of the coupling between the electric field and the transport of charged particles. It is the first step necessary for the development of more complete discharge models (electrical modeling is usually sufficient to obtain an understanding of the basic mechanisms).

II.6.2. 1. The different models

The transport phenomena of charged particles are entirely described by the Boltzmann equation. From this property, an ideal self-consistent electrical model would consist of a system of equations coupling the Boltzmann equation for electrons and for ions with the Poisson equation: indeed the charge carriers move in an electric field which depends on densities itself. However, the numerical resolution of such a seemingly simple system is too complex to implement as it stands. To simplify the problem, there are physical approaches based on degrees of approximation. We can distinguish two main categories of digital discharge models: microscopic models and macroscopic models. For each category of model the term source of creation of particles is a fundamental parameter which must be described as precisely as possible.

- **The microscopic model (particular model)**

The microscopic model provides the spatio-temporal variations of the velocity distribution functions of charged particles, by directly solving the Boltzmann equation with Particle in Cell and Monte Carlo methods in general [51-56]. These particle methods are based on individual treatment of particles subjected to both electric field and collisions. To illustrate how they work, take the example of the Monte Carlo statistical technique. This method considers a finite number of particles representative of all charge carriers (ions, electrons) and follows their movement in the phase space under the effect of the field and the collisions, while solving the Poisson equation. at regular intervals. The moment of the collision, its nature, the angular deviation, the distribution of the energy are determined by the generation of random numbers whose probability densities are related to the total and differential cross sections of collision. If the particle does not make a collision, its trajectory is simply integrated using the equations of classical mechanics. For a given particle type, it is clear that to obtain a correct statistical balance a large number of trajectories must be determined. From a physical point of view, the particle approach is the most accurate, but from a practical point of view this technique is very demanding in terms of calculation time. It is especially suitable for conditions of discharges at very low pressure when the density is not too high.

- **The macroscopic model (fluid model):**

This type of model does not solve the Boltzmann equation. The kinetics of the charged particles are described by a set of average magnitudes, such as density, average directed velocity, or average energy, while their velocity distribution functions are unknown (they are chosen beforehand) [57-58]. These quantities are calculated by replacing the Boltzmann equation in the phase space by its moments which are obtained by multiplying the equation Eq. 2-29 by 1, v, v^2, ..., v^n (1^{st} moment, 2^{nd} moment, second moment) and integrating into space velocities. The rigorous resolution of the problem makes it necessary to solve an infinity of moments of the Boltzmann equation, Which is impossible. To limit the number of moments and close the system, it is necessary to resort to simplifying hypotheses on the moments of higher orders. It is then obvious that the fluid representation is directly limited by the degree of simplification of the velocity distribution function of the charged particles.

In general the average magnitudes are determined from the resolution of the first two or three moments of the Boltzmann equation:

Multiplying by 1 and integrating into velocity space, we obtain the first moment that corresponds to the continuity equation:

$$\frac{\partial n}{\partial t}+\nabla_r.\left(n\bar{v}\right)=\left.\frac{\partial n}{\partial t}\right|_{collision}=S \tag{II-20}$$

For a given species, the term *S* (source term) represents the variation of the density of particles under the effect of collisions (ionization, recombination, attachment, etc.). By imposing the velocity distribution function (for example of the Maxwellian type) it is possible to express the source term as a function of the frequencies of creation and disappearance of particles. Considering an electropositive gas, *S* is written:

$$S=n_e\overline{\nu_i}-Rn_en_i \tag{II-21}$$

with ν_i the frequency of ionization, *R* the frequency of electron recombination. Electrons are created by ionization and disappear by recombination. By multiplying by (*mv*) and integrating into velocity space, we obtain the second moment which corresponds to the momentum transfer equation:

$$\frac{\partial nm\bar{v}}{\partial t}+nm.\left(\bar{v}\nabla_r\right)\bar{v}+\bar{v}\left(\nabla_r nm\bar{v}\right)+\nabla_r P-n\overline{F}=m\left.\frac{\partial v}{\partial t}\right|_{collision} \tag{II-22}$$

F represents the external forces exerted on the particles; *P* is the kinetic pressure tensor which corresponds to the thermal agitation energy density. This equation represents the total temporal change in momentum under the influence of external forces, kinetic pressure and collisions.

$$P=m\int\left(v-\bar{v}\right)\left(v-\bar{v}\right)f\left(v\right)dv^3 \tag{II-23}$$

As for the continuity equation, we can define a momentum exchange frequency ν_m. Moreover developing the left-hand terms of Eq.2-31 and using Eq.2-29 we have:

$$nm\left(\frac{\partial\bar{v}}{\partial t}+\left(\bar{v}\nabla_r\right)\right)\bar{v}=n\overline{F}-\nabla_r P-Sm\bar{v}+nm\overline{\nu_m v} \tag{II-24}$$

Using some simplifications, the momentum transfer equation can be written as a drift term proportional to the electric field and a diffusion term:

$$n\bar{v}=n\left(\frac{q}{m\nu_m}\right)E-\frac{1}{m\nu_m}\nabla_r\left(nk_BT\right) \tag{II-25}$$

with:

$$\mu = \left(\frac{q}{m\nu_m} \right),\ D = \left(\frac{k_B T}{m\nu_m} \right) \tag{II-26}$$

respectively representing the mobility coefficient and the diffusion coefficient of a given particle type.

✓ The first approximation consists in neglecting the drift energy with respect to the thermal stirring energy. It is justified in the plasma (negative glow) where the electric field is weak and the collisions numerous. This is no longer true in the cathodic drop region, where electrons from ion bombardment at the cathode are accelerated in a strong electric field. They have a directed energy of the same order as thermal agitation.

✓ The second simplification consists in neglecting the term of time derivative by supposing that the flux is modulated by the RF signal.

To improve the representation of the ionization processes, a third moment of the Boltzmann equation corresponding to the energy transport equation for the electrons can be added to the system. Thus in this model we can consider that the term source of ionization depends on the energy ($\nu_i(\varepsilon)$) and not on the local field (ν_i(E / p)). The new equation is obtained by multiplying by 1 / 2mv2 the Boltzmann equation and integrating it into the velocity space:

$$\frac{\partial n_e \bar{\varepsilon}}{\partial t} + \frac{5}{3}\nabla\left(n_e \bar{\varepsilon}\bar{\bar{v}} \right) + \nabla Q - n_e e \bar{v} E = -n_e \nu_e \bar{\varepsilon} \tag{II-27}$$

with e the elementary charge, ν_e the frequency of energy exchange by collision, E the electric field, Q the flow of heat.

Although the representation of ionization in the landfill is more accurate, it is not quite accurate. On the one hand, the hypothesis of the isotropic kinetic tensor is not correct for the electrons (coming from the ion bombardment of the electrodes) present in the vicinity of the sheaths and which have high directed velocities, on the other hand, the average energy Electrons are mainly determined by the slow electrons of the plasma whereas ionization is determined by fast electrons (fewer).

By considering the coupling of continuity equations and momentum transfer equations for ions and electrons with the Poisson equation, we have a first, fluid representation of RF discharges.

From approximations, several fluid models describing the spatio-temporal representation of the ionization source term in the discharge can be distinguished.

- **The local equilibrium model**

This model uses the hypothesis of local equilibrium as closure relation: the energy gained in the electric field by the particles is locally compensated by the losses in collisions with the other species of particles. In this approach, the transport coefficients and the ionization source term depend only on the local electric field (E / p, with p the pressure). If this hypothesis is correct for the ions which have a low mobility because of their mass and the electrons of the plasma, it is not totally true for the electrons being in the vicinity of the sheath. Indeed, they can gain energy in the intense field and deposit it further in the negative glow. Model representation of ionization processes in the landfill may be poorly described.

- **The model with two groups of electrons (fast electron, slow electron)**

This model deals, on the one hand, with accelerated fast electrons in the sheaths near the electrodes (they are supposed to form a mono energetic beam moving towards the plasma). on the other hand, the slow electrons of the plasma in equilibrium with the local field. The model can also describe ionization in both regions. Fast electrons are treated by an equation of continuity and energy, and slow electrons by the assumption of local equilibrium (continuity equation + momentum exchange equation). A fast electron joins the group of slow electrons after dissipating most of its energy. Reverse routing is also possible in RF discharges. The flow of electrons emitted by each electrode is obtained by the product between the incident ions flux with the secondary emission coefficient γ.

The main disadvantage of the model is the overestimation of the penetration of the fast electron beam in the negative glow which corresponds to an overestimation of the spatio-temporal variations of the ionization in the discharge.

- **The hybrid model**

The fluid-Monte Carlo mixed model consists of a coupling between a particle model that processes the fast electron group with the Monte Carlo statistical technique and a fluid model that supports slow plasma electrons[59-60]. The representation of the term ion source ion induced by electrons is as accurate as possible. The coupling between the microscopic and

fluid parts of this type of model takes place as follows: the fluid model calculates the spatio-temporal distribution of the electric field of the discharge from the densities (continuity equations). The field distribution is then used as input to the microscopic model that calculates the spatio-temporal variations of the ionization source term (Monte Carlo). The ionization source term is then reinjected into the fluid model and so on. This type of model allows, for a reasonable calculation time, a correct representation of the spatio temporal variations of the ionization source term of the discharge.

II.7. Cross section

To develop the modeling of electrical discharges in a gaseous medium, it must to know a numbers of basic data such as: the electron collision cross sections for particle modeling or the electron swarm parameters in the case of the fluid modeling. The knowledge of all the electron swarm parameters as a function of the reduced electric field is indispensable for the fluid models based on the first and the second moment of the electron energy distribution function.

The cross section is a measure of probability that a specific process will take place in a collision of two particles. Cross section is typically denoted σ (sigma) and is expressed in terms of the transverse area that the incident particle must hit in order for the given process to occur. When two particles interact, their mutual cross section is the area transverse to their relative motion within which they must meet in order to scatter from each other. When a cross section is specified as a function of some final-state variable, such as particle angle or energy, it is called a differential cross section. When a cross section is integrated over all scattering angles (and possibly other variables), it is called a total cross section.

In physics, the concept and measurement of nuclear reaction cross sections has been instrumental for the understanding of nuclear structure and nuclear reactions as well as for practical applications such as the development of nuclear reactors. Chemical reaction cross sections will be quite possibly of similar importance for chemistry.

II.7.1. Scattering cross section

Differential and total scattering cross sections are experimental tools widely used in the study of atomic and subatomic physics. The scattering cross section is used to relate the

impact parameter to the scattering angle of a collision particle with the force field of another particle. In this section, we will discuss the notion of the cross section of the physical side and the mathematical side, taking into account the theory of classical physics and the theory of quantum mechanics.

II.7.1.1. Cross section in classical mechanics

The idea of using a surface to express such a probability of interaction probably dates back to the discovery of the atomic nucleus by Rutherford in 1911, the cross section is the imaginary surface that a target particle should have to reproduce the observed probability collision or reaction with another particle. If we assume that these collisions occur between impenetrable physical objects (hard spheres), as shown in the following figure:

Fig. II-1: *Representation of the cross-section in the case where the atom is considered a sphere and without taking into account the interaction potential*

If the projectile (electron or ion) and the target (atom or molecule of Radius R) are considered hard spheres without potential interaction, the electron-atom cross section ($\sigma_{e\text{-}A}$) and ion-atom cross section can be calculated by the following relations :

$$\sigma_{e-A} = \pi R^2$$
$$\sigma_{A-A} = 4\pi R^2 \qquad \text{(II-28)}$$

Now, if we consider the case of a central interaction potential *U(r)* which depends only on the distance *r* with respect to the center of the potential. The incident beam will be in the direction of the *z* axis and thus the differential cross section will be a function of the axial angle θ only, and not the azimuthal angle φ. The projectile impact parameter *b* is defined as the distance between the projectile trajectory and the axis passing through the center of the target (see Figure I-4) in the region without interaction (at a great distance before the target).

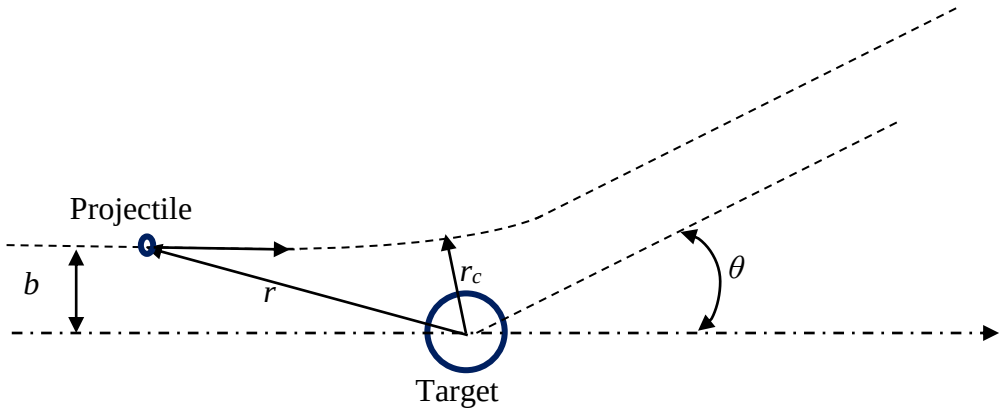

Fig. II-2: Representation of a binary collision with the impact parameter, the deviation in the center of the mass by an angle θ, and the minimum approach distance r_c.

To understand the ideas behind scattering cross sections, it is first necessary to understand the physics behind a particle moving in a central force field. It is known and can be derived from the Lagrangian dynamics applied to a particle moving in a central force field that the kinetic moment of the particle is conserved:

$$p = \mu r\dot{\theta} \Rightarrow \dot{\theta} = \frac{p}{\mu r} \tag{II-29}$$

where μ is the reduced mass of the particle system. In the absence of dissipative forces, the total energy ($E=E_c+U$, where E_c: is the kinetic energy and U: is the potential energy) of the system must also be conserved:

$$E = \frac{1}{2}\mu\left(\dot{r}^2 + r^2\dot{\theta}^2\right) + U\left(r\right) \tag{II-30}$$

By substituting the value of the angular velocity found from the conservation of kinetic moment, the energy takes the following form:

$$E = \frac{1}{2}\mu\dot{r}^2 + \frac{1}{2}\frac{p^2}{\mu\dot{r}^2} + U\left(r\right) \tag{II-31}$$

This equation can be solved for radial velocity:

$$\dot{r} = \pm\sqrt{\frac{2}{\mu}\left(E - U(r)\right) - \frac{p^2}{\mu r^2}} \tag{II-32}$$

According to the chain derivation rule we have:

$$d\theta = \frac{d\theta}{dt}.\frac{dt}{dr}.dr = \frac{\dot{\theta}}{\dot{r}}dr \tag{II-33}$$

It follows that the equations (I-8), (I-11) and (I-12):

$$\theta(r) = \pm\int \frac{\left(p/r^2\right)dr}{\sqrt{2\mu\left(E - U(r) - \dfrac{p^2}{2\mu r^2}\right)}} \tag{II-34}$$

From equation (I-11), the radial velocity disappears at the roots of the radical. This indicates to these points that the particle knows a turning point. These two roots represent the maximum and minimum rays reached by the orbit. The angular change of the orbit is twice that which would result from a displacement of the minimum to the maximum:

$$\Delta\theta = \pm\int_{r_{min}}^{r_{max}} \frac{\left(p/r^2\right)dr}{\sqrt{2\mu\left(E - U(r) - \dfrac{p^2}{2\mu r^2}\right)}} \tag{II-35}$$

This last equation will be used in the analysis of the scattering angle of a particle as it approaches the central force field. The differential scattering cross section is defined as the number of interactions per target particle leading to scattering in a solid angle element at a given angle divided by the number of incident particles per unit area. The following analysis is performed in the mass center referential. In Figure I-5, an incident particle with the impact parameter *b* is deflected by an angle θ into a detector located at a large distance *L* from the scattering center *O*. The differential specific surface of the detector is represented by *dS*.

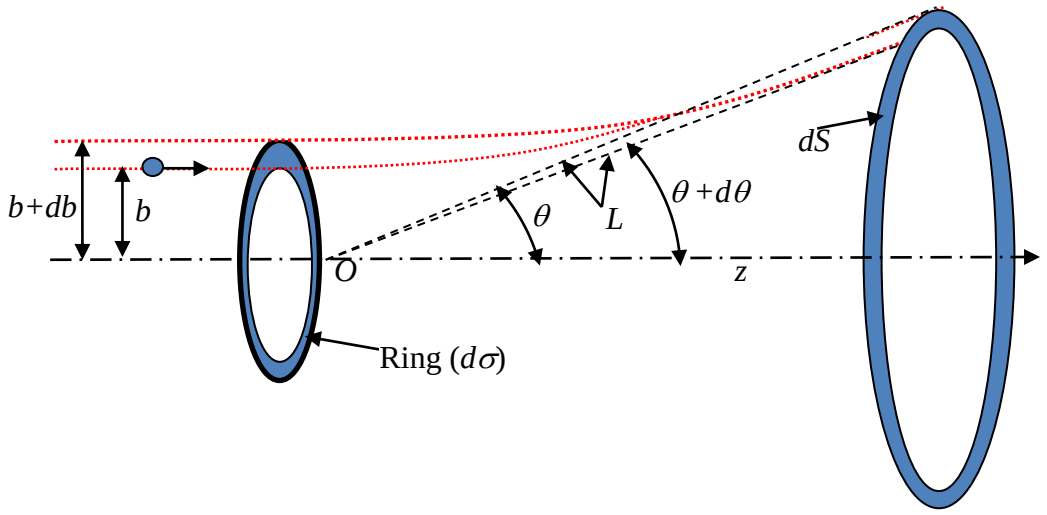

Fig. II-3: *Schematization of the interaction in a center of mass referential.*

The solid angle through which the particles are deflected in Figure I-5, is represented by $d\Omega$ and can be obtained by the relation I-15. It is important to look at Figure I-5 to understand the relationship between the differential surface dS and the deflection angle.

$$d\Omega = \frac{dS}{L^2} = \frac{\left(L.|d\theta|\right)\left(2\pi L\sin\theta\right)}{L^2} = 2\pi\sin\theta|d\theta| \qquad \text{(II-36)}$$

The differential cross section is defined as the ratio between the surface of the ring $d\sigma$ and the solid angle $d\Omega$, it is expressed by the following relation:

$$\frac{d\sigma}{d\Omega} = \frac{2\pi b.|db|}{2\pi\sin\theta|d\theta|} = \frac{2\pi b.|db|}{2\pi\sin\theta|d\theta|} = -\frac{b}{\sin\theta}.\frac{db}{d\theta} \qquad \text{(II-37)}$$

where the equation is negative because an increase in db in the impact parameter means that less force is exerted on the particle, which causes a decrease in the scattering angle. The expression that relates the impact parameter and the scattering angle of a two-particle system undergoing a central force field collision in the center of mass reference is given as follows [8]:

$$\theta = \pi - 2b\int_{r_c}^{\infty} \frac{\left(b/r^2\right)dr}{\sqrt{1-\left(\frac{b}{r}\right)^2-\left(\frac{U(r)}{E_c}\right)^2}} \qquad \text{(II-38)}$$

r_c is the pole of the equation (I-17), it satisfies the following equation:

$$\left(\frac{b}{r_c}\right)^2+\left(\frac{U(r_c)}{E_c}\right)^2=1 \tag{II-39}$$

Now, the transfer cross-section of quantity σ_m of the movement can be obtained by integrating the product of the differential cross section by the term (1-cosθ) on the solid angle:

$$\sigma_m(E_c)=2\pi\int_0^{2\pi}\frac{d\sigma(E_c,\theta)}{d\Omega}(1-\cos\theta)\sin\theta d\theta \tag{II-40}$$

So far, discussions have focused on mathematics, but it is important to understand them to use the idea of the diffusion cross section in a practical way, where one of the most notable uses of this idea comes from the Rutherford diffusion equation. Using the method described in the mathematical part, it is quite simple to derive an equation for the scattering cross section of a particle undergoing interaction with a nucleus where the interaction potential is Colombian of the form V_0/r. The equation for this section is:

$$\frac{d\sigma(E_c,\theta)}{d\Omega}=\frac{V_0^2}{(4E_c)^2}\cdot\frac{1}{\sin^4\left(\frac{\theta}{2}\right)} \tag{II-41}$$

II.8. Reaction Rate and Activation Energy

Studies of reaction rates and molecular structure are two main branches of chemical research. Certainly, there has been some advance in recent years toward an understanding of the forces which act during a chemical reaction and their effects on the rates of reactions. In general, rate constants depend on the temperature.

Two species of molecules are at concentration n1 and n2. (typical unit: molecules/m3). They are confined to a volume V and at temperature T. They undergo a binary reaction, with cross section σ(v), where v is the relative velocity of the molecules. The reaction rate is:

$$R=V\,n_1 n_2\int d^3\boldsymbol{v}_1\int d^3\boldsymbol{v}_2\,\sigma(\boldsymbol{v}_1-\boldsymbol{v}_2)(\boldsymbol{v}_1-\boldsymbol{v}_2)\,f_2(\boldsymbol{v}_1,\boldsymbol{v}_2) \tag{II-42}$$

In (1) f_2 is the joint probability density function for two values of the velocity. The inner integral (over v_2 in this case) counts the number of particles moving at velocity v_2 while the second counts and weighs those at a given v_1-v_2

In the case of a dilute gas at equilibrium, this joint probability density function is the product of the values of Maxwell-Boltzman distribution at the the two velocity values.

$$R = V\, n_1 n_2 \left(\frac{m_1}{2\pi k T}\right)^{3/2} \left(\frac{m_2}{2\pi k T}\right)^{3/2} \int d^3\mathbf{v}_1 \int d^3\mathbf{v}_2 \sigma(\mathbf{v}_1 - \mathbf{v}_2)(\mathbf{v}_1 - \mathbf{v}_2) \exp\left(\frac{-m_1 v_1^2}{kT}\right) \exp\left(\frac{-m_2 v_2^2}{kT}\right) \quad \text{(II-43)}$$

After some calculations we obtain this relation

$$r \propto T^n \exp\left(\frac{-E_A}{kT}\right) \quad \text{(II-44)}$$

In the case of chemical reactions,the usual references restrict *n* to between ±1so try a different simplifying assumption for the dependence of cross section on relative speed: The cross section is zero up to a minimum relative energy then rises to a constant value and stays there for all higher relative speeds.

A detailed description of cross sections and reactions rate was made in the work of Kuppermann, A., & Greene, E. F. (1968) [61].

II.8. Conclusion

In this chapter, we have presented a general view on plasmas by giving some basic notions and the main characteristics of electrical discharges, and then we have detailed the different physicochemical processes that occur in the plasma volume. A study of the characteristics and operating principle of capacitance (CCP) and inductively coupled (ICP) radiofrequency discharges which will be the subject of our study. We have thus presented the different models used for modeling of plasmas. The rest of the thesis is divided into other three chapters; the chapter III is devoted to the description of the data necessary for the modeling of methane plasma while the chapter IV and V is for the results simulation for the Capacitively Coupled Plasma (CCP) and the Inductively Coupled Plasma (ICP) configurations.

CHAPTER III

ELECTRON COLLISION CROSS SECTIONS FOR METHANE MOLECULE

III.1. Introduction

The methane molecule is the simplest polyatomic hydrocarbon and it is present in the atmosphere of most planets and on the interstellar surface [62-64]. It is also used in plasmas in many fields of technology and is considered a good test gas. Several studies have taken place that were interested experimentally [65-75] and numerically in pure methane [76-86], and other studies have mixed methane with other gases such as H_2, N_2, etc. [87-96]. The study and the modeling of a plasma require knowledge of the physical processes; these last are based on elementary microscopic mechanisms such as ionization, excitation, attachment, recombination, dissociation, and elastic collisions. Indeed, it is known that knowledge of the cross-sections relating to these mechanisms is indispensable to obtain the electron energy distribution function (EEDF), the electron transport coefficients, and the rates of the different reactions. It is known that the first process happened for the formation of plasma is the electronic impact reaction. In this chapter we present a complete set of electron collision cross-sections for the methane molecule by revising all of the collision cross-sections and adding the partial collision cross-sections data relating to dissociation by electron impact. For the latter there are no available measurements data for each channel of dissociation and no validated recommended data for use in the modeling, although these data are very important in order to determine the different species in methane plasma. The rate coefficients of the partial dissociative collisions into neutrals and the partial ionization collisions are also calculated, and when fitted, these can be used as input for fluid models. This work is concluded by the validation of our set of data through a comparison between the transport coefficients calculated by using our data and the measurements of the transport coefficients that already exist in the literature.

III.2. Overview

In the literature, there are several studies regarding the elastic and inelastic cross-sections; among these works, we are interested in the cross-sections that lead to reproduction of the transport coefficients in accordance with the measurements. Either experimentally or numerically, many authors have contributed to the determination of the electron transport coefficients in methane, whether for pure methane or as a mixture with other gases, generally hydrogen. Chronologically, we can cite for example the works of Duncan et al. 1972 [97], Winter 1975 [98], Tashibana et al.1984 [86], Jones et al. 1984 [99], Haddad 1985 [100],

Davies et al. 1989 [101],Schmidt 1991[102], Nakano et al [103], Rhallabi et al.1991 [83], Gogolides et al.1994 [104], Nagayama et al. 1998 [80], MiYong Song et al. 2015[105], and Korolov et al. 2016 [106]. Duncan [97] measured the diffusion coefficient and evaluated cross-sections consistent with these measurements. Winters [98] reported the total cross-section for methane dissociation at electronic energies between 10 and 500 eV. Jones et *al.* [99] measured the total effective cross-section at electronic energies between 1.3 and 50 eV. The analysis of Haddad [100] is based on measurements of the drift velocity and transverse diffusion by using the multi-term solution of the Boltzmann equation to derive the elastic and inelastic cross-sections. Schmidt [102] presented an analysis at a low energy, he used the transport coefficients, including longitudinal diffusion, to find the elastic and vibration cross-sections, and demonstrated that elastic anisotropic scattering has a significant influence and that, therefore, it must be taken into account to achieve a good description of the transport coefficient for methane. Davies et *al.* [101] measured the drift velocity as a function of the reduced field *E*/*N* from 10 to 1000Td, and also measured the ion mobility and the ionization coefficient for a reduced field of between 80 and 1000 Td. These authors used swarm data to derive the electron cross-sections. In their work, all of the dissociation cross-sections are taken to be equal above 13 eV, and the probability of each fragment from the excited state of CH_4 is not resolved. The last work on the e-CH_4 collision cross-sections is that of Mi-Yong Song *et al.* [105], where the authors reported the cross-sections for various collision processes that was carried out until 2014. They recommended a set of collision cross-sections but without including the dissociative cross-sections.

III.3. Electron collision cross section for methane

After a bibliographic research, we found a many authors who have spoken about the dissociation of methane by electronic impact [107-115]. When the molecule contains at least three atoms, the number of dissociative excitation channels, ionization and recombination increases drastically. For example, electron impact on the H_2 molecule yields only two fragments, and for CH4 can produce CH_3 + H, CH_2 + 2H (or H_2), CH + 3H (or H + H_2), C + $2H_2$ (or 2H + H_2), where the atomic and the molecular products both being in excited states (electronic and / or vibratory). The processes of molecular fragmentation lead to a multiplication of molecular species in the plasma and to chains of long reactions before the complete dissociation of the initial molecule is accomplished. Unfortunately to this day, it there are no effective electron dissociation cross sections of methane to the following

channels CH_3 + H, CH_2 + H_2, CH + H_2 + H and C + $2H_2$. Mi-Song Yong *et al.* [109] confirm that for the dissociative channels; (1): CH_3 + H, (2): CH_2 + H_2, (3): CH_2 + 2H, (4): CH + H_2 + H, there is no practical measure that distinguishes between (2) and (3) and no direct estimate of (4). Erwin *et al.* [66], [114] presented a semi-empirical method to estimate the dissociative cross sections, but without including the dissociation to C + $2H_2$ (or 2H + H_2). As determined from the literature [101, 96, 105, 110, 116, 117]. The important electron CH_4 molecule collisions are resumed in table III-1:

Table III-1: Electron–CH_4 collisions.

N°	Collision	Threshold (eV)	Ref
1	e+ CH_4=> e + CH_4	---	
2	e+ CH_4=> e + CH_4	0.162	105, 117
3	e+ CH_4=> e + CH_4	0.362	105, 117
4	e+ CH_4=> e +CH_3 +H	8.8	96, 116
5	e+ CH_4=> e + CH_2+H_2	9.4	96, 116
6	e+ CH_4=> e + CH+ H_2+H	12.5	96, 116
7	e+ CH_4=> e + C+2 H_2	14	96, 116
8	e+ CH_4=> 2e + CH_4^+	12.63	96, 110, 116
9	e+ CH_4=> 2e + CH_3^+ + H	14.25	105, 116
10	e+ CH_4=> 2e + CH_2^+ + H_2	15.1	116
11	e+ CH_4=> 2e + CH^++ H_2+H	19.9	116
12	e+ CH_4=> 2e + C^+ + 2 H_2	19.6	116
13	e+ CH_4=> 2e + H_2^+ + CH_2	20.1	116
14	e+ CH_4=> 2e +H^+ + CH_3	18.0	116

III.3.1. Momentum transfer cross section

The momentum-transfer cross section gives a measure of momentum transfer during the elastic collision. It is better to use this cross section for plasma simulation, because it not requires the knowledge of the differential cross section to calculate the diffusion angle during the elastic collision. This cross section can be calculated by the following expression:

$$\sigma_m(\varepsilon) = 2\pi \int_0^{\pi} \frac{d\sigma_{el}(\varepsilon,\chi)}{d\chi} \sin(\chi)\left(1-\cos(\chi)\right) d\chi \qquad \text{(III-1)}$$

where $\sigma_m(\varepsilon)$ and $\sigma_{el}(\varepsilon,\chi)$ are the momentum and the elastic cross section as a function of electron energy ε, and χ is the diffusion angle. The measurements of Cho et *al.* [118], Boesten *et al.* [119] , Sakae *et al.* [120], Sohn *et al.* [121], Iga *et al.* [122], Vuskovic *et al.* [110], Tanaka *et al.* [123], Shyn *et al.* [124], and Bundschu *et al.* [125] are reviewed by Song

et al. [105]. In this last study, the momentum transfer cross sections have been collected and reviewed, the data derived from swarm experiments are also considered for the recommended values. In the study of Davies *et al.* [101], the cross section set includes a momentum transfer cross section which is based primarily on theirs and previous drift velocity measurements. Shmidt *et al.* [102] determined a set of elastic and inelastic scattering cross sections up to 3 eV based on a comprehensive set of transport parameters of electrons in methane derived from single electron spectra in the range of field 0.01-15 Td. In figure III-1 we show the electron-CH_4 theoretical and the measured data of momentum transfer cross section, the red continuous line represents our recommended data in the figure III-1.

$$\sigma_m(\varepsilon) = \begin{cases} a_1.\varepsilon^{a_2}.e^{-a_3(\varepsilon-a_4)} + \dfrac{a_5}{a_6 + e^{a_7.\varepsilon}}; & \varepsilon \le 4\text{eV} \\ \displaystyle\sum_{i=1}^{7} b_i.\varepsilon^{7-i}\ ; & 4\text{eV} < \varepsilon \le 15\text{eV} \\ \displaystyle\sum_{i=1}^{5} c_i.\varepsilon^{5-i}\ ; & 15\text{eV} < \varepsilon \le 30\text{eV} \\ 3.5.\left(\dfrac{\varepsilon}{30}\right)^{-1.2116}\ ; & 30\text{eV} < \varepsilon \le 1000\text{eV} \end{cases} \qquad \text{(III-2)}$$

where σ_m is the momentum transfer cross section in Å^2, and ε is the electron energy in eV, where the minimum Ramsauer is taken at 0.3eV with value of 0.394 Å^2. The momentum transfer cross section recommended in this work is expressed by equation III-2, where the fitted parameters are reported in table III-2.

Table III-2: Fitted data for the momentum transfer cross section.

	i=1	i=2	i=3	i=4	i=5	i=6	i=7
a_i	2.06	1.63	0.14	0.05	7.72	-0.68	14.1
b_i	-1.57E-5	4.67E-4	-1.83E-4	-0.102	0.726	1.547	-0.368
c_i	-2.67E6	5.72E5	-4.28E4	1.48E3	-16.2		

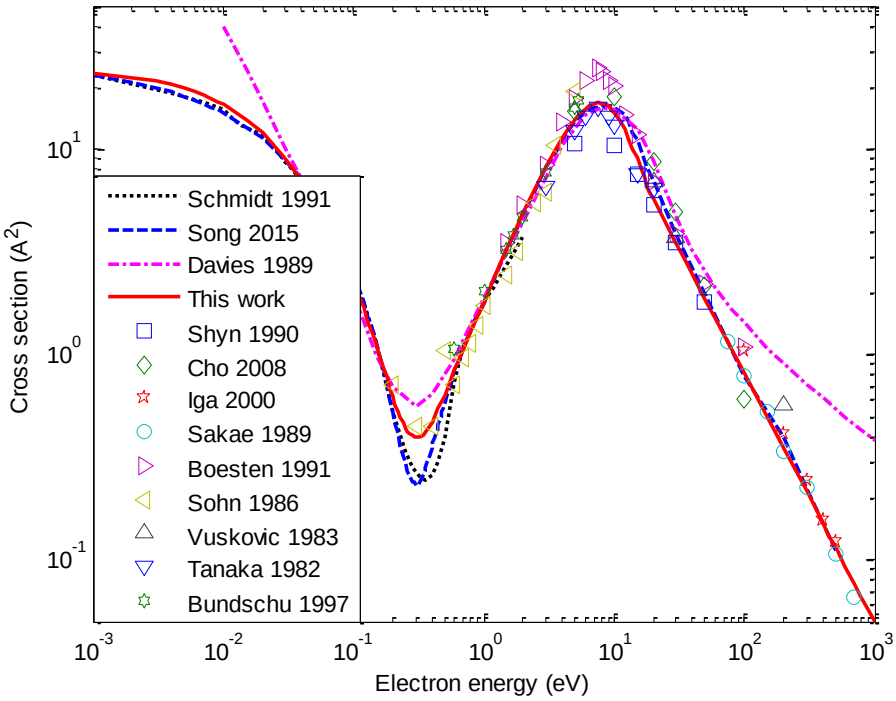

Fig. III-1: Electron–CH_4 Momentum transfer collision cross sections, the measurement data from references [110], [118-125].

III.3.2. Vibration cross section

In the plasma, the processes of the vibrational excitations of the neutrals have a major contribution to activate the chemical kinetics, because of theirs lowers thresholds. Methane molecules have four normal modes of vibrational excitation ν_1 at 0.362 eV, ν_2 at 0.190 eV, ν_3 at 0.374 eV, and ν_4 at 0.162 eV [117]. It is very difficult to measure these four modes separately; all the measurements found in the literature give the measurements for two composite modes ν_{24} at 0.362 eV, and ν_{13} at 0.36 eV. Figure III-2 and Figure III-3 show the original measurements data of Shyn [126], Tanaka *et al.* [127], Bundschu *et al.* [125] for ν_{24} and ν_{13}, while the data of Sohn *et al.* [117] are digitized from the reference [128], the original measurements are the differential cross section for 35°, 75°, 90°, and 105° as a function of the electron energy from the threshold to 1.2 eV for ν_{24}, and from the threshold to 2 eV for ν_{13}. Curik *et al.* [129] measured the differential cross section from 0° to 180 for 5 eV and 10 eV, and they measured the differential cross section from 0.3 eV to 20 eV for 90°, the reported data are those normalized to the integral cross section for 10 eV. The data of Song *et el.* [105], Davies *et al.* [101], and of Schmidt [102] are derived from the swarm parameters. Our fitted data are reported in table III-3.

Table III-3: Fitted data for the vibration collision with Methane molecule.

Energy (eV)	$\nu 24$ (Å^2)	Energy (eV)	$\nu 13$ (Å^2)
0.162	0.00000	0.362	0.00000
0.17	0.12241	0.38	0.06800
0.18	0.27001	0.4	0.12703
0.19	0.37298	0.42	0.17231
0.2	0.44000	0.45	0.22105
0.21	0.48200	0.47	0.24398
0.23	0.52135	0.5	0.26800
0.25	0.53000	0.55	0.28911
0.27	0.52526	0.6	0.29570
0.3	0.50863	0.65	0.29403
0.35	0.47588	0.7	0.28769
0.37	0.46334	0.75	0.27878
0.4	0.44574	0.8	0.26858
0.45	0.41975	0.85	0.25783
0.5	0.39745	0.9	0.24701
0.6	0.36134	0.95	0.23638
0.7	0.33329	1	0.22610
0.8	0.31073	1.2	0.19952
0.9	0.29209	1.5	0.19055
0.95	0.28392	1.8	0.20210
1	0.27637	2	0.21516
1	0.27637	2.5	0.25374
1.2	0.25394	3	0.29682
1.5	0.23891	3.5	0.35331
1.8	0.24000	4	0.43627
2	0.24734	4.5	0.55295
2.5	0.28315	5	0.69906
3	0.34000	5.5	0.85729
3.5	0.41691	6	1.00000
4	0.51317	6.5	1.09620
4.5	0.62506	7	1.12290
5	0.74417	7.5	1.08000
5.5	0.85765	8	1.01070
6	0.95000	8.5	0.92480
6.5	1.00680	9	0.83120
7	1.02000	10	0.65000
7.5	0.99511	12	0.42439
8	0.96000	15	0.30000
8.5	0.91468	20	0.22000
9	0.86177	100	0.04283
10	0.75000		
12	0.60402		
15	0.47000		
20	0.36000		
100	0.10000		

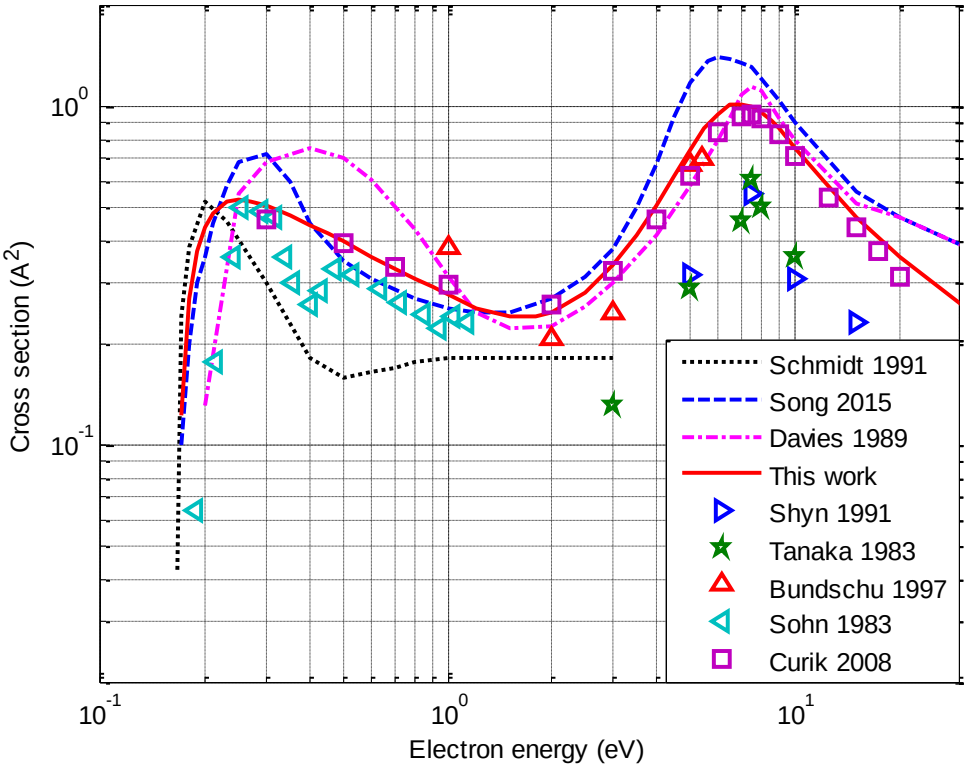

Fig. III-2: Vibration (v24) collision cross sections, the measurement data from references [117], [125-127], [129].

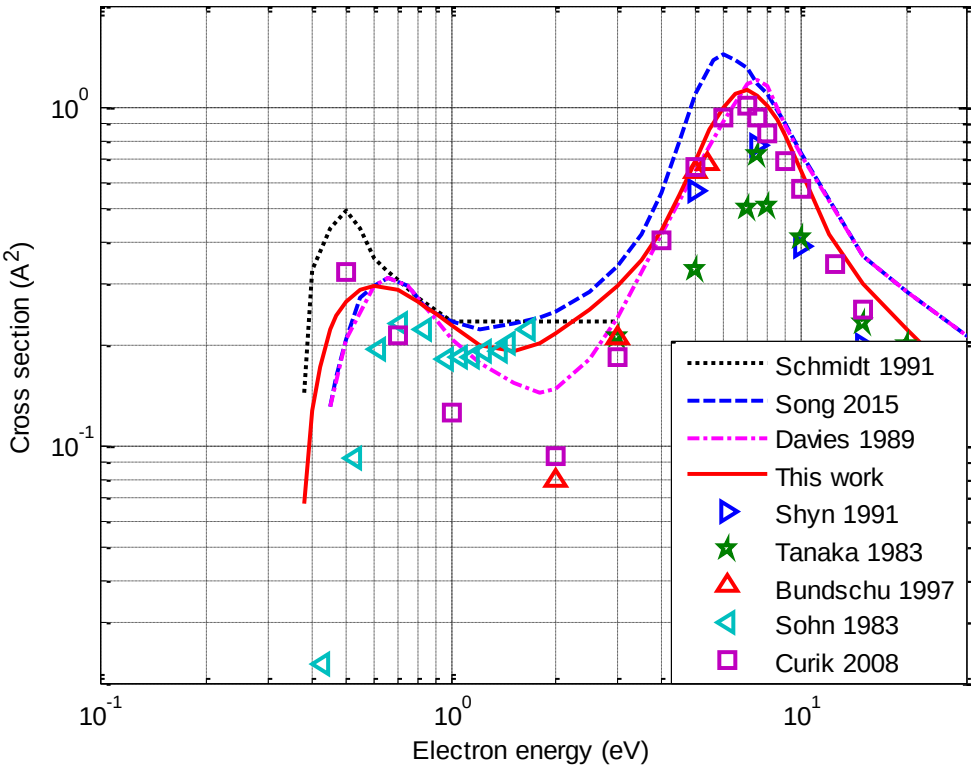

Fig. III-3: Vibration (v13) collision cross sections, the measurement data from references [117], [125-127], [129].

III.3.3. Ionization cross section

The partial ionization cross sections taken in this work are those measured by Straub *et al.*[130], but they are normalized to the total ionization cross sections measured by Rapp and Englander Golden [76] (table III-4). For the reactions 8 and 9, the first cross section measured by Straub *et al.*[75] is at 15 eV, for reaction 10 at 17.5 eV, for reactions 11, 13, 14 at 25 eV, and for reaction 12 the first measurement is taken at 30 eV. In order to complete these data near threshold, we have used the interpolation according to the Wannier threshold law [132].

$$\sigma_i\left(\varepsilon_{th} \le \varepsilon \le \varepsilon_l\right) = a_1\left(\frac{\varepsilon}{\varepsilon_{th}} - 1\right)^{a_2} \qquad \text{(III-3)}$$

where σ_i: is the partial dissociative ionization cross section in $Å^2$(I =8,9,10,11,12,13,14), ε_{th}: threshold energy (eV), ε: electron energy (eV), ε_l: is the energy upper limit, and a_1, a_2 are the interpolation parameters, which they are reported in table III-5.

Table III-4: Partial ionization cross sections by impact electron in Methane

Energy (eV)	CH_4^+ ($Å^2$)	CH_3^+ ($Å^2$)	CH_2^+ (0.1$Å^2$)	CH^+ (0.1 $Å^2$)	C^+ (0.01 $Å^2$)	H_2^+ (0.01 $Å^2$)	H^+ (0.1 $Å^2$)	Total ($Å^2$)
12.63	0.0000							0.0000
13	0.0109							0.0109
13.5	0.0342							0.0342
14	0.0738							0.0738
14.5	0.1216	0.0084						0.1301
15	0.1658	0.0319						0.1978
15.5	0.2176	0.0599	0.0027					0.2778
16	0.2689	0.0905	0.0097					0.3604
16.5	0.3198	0.1231	0.0193					0.4448
17	0.3699	0.1571	0.0309					0.5301
17.5	0.4146	0.1901	0.0439					0.6092
18	0.4682	0.2309	0.0584					0.7050
18.5	0.5162	0.2685	0.0734					0.7921
19	0.5643	0.3057	0.0896				0.0004	0.8791
19.5	0.6188	0.3461	0.1080				0.0011	0.9758
20	0.6676	0.3832	0.1264				0.0028	1.0638
21	0.7562	0.4658	0.1663	0.0004		0.0133	0.0066	1.2396
21.5	0.8053	0.5108	0.1878	0.0013	0.0003	0.0191	0.0101	1.3363
22	0.8434	0.5492	0.2070	0.0028	0.0008	0.0244	0.0143	1.4154
22.5	0.8814	0.5876	0.2263	0.0052	0.0016	0.0295	0.0195	1.4945
23	0.9194	0.6231	0.2726	0.0087	0.0032	0.0346	0.0258	1.5737
23.5	0.9571	0.6585	0.3195	0.0135	0.0055	0.0395	0.0333	1.6528
24	0.9895	0.6903	0.3651	0.0196	0.0089	0.0442	0.0418	1.7231
25	1.0438	0.7468	0.4523	0.0364	0.0238	0.0525	0.0598	1.8462
26	1.0961	0.7967	0.6036	0.0619	0.0396	0.0623	0.0893	1.9693
28	1.1866	0.8875	0.9117	0.1429	0.1189	0.0806	0.1633	2.1979
30	1.2432	0.9537	1.2007	0.2673	0.2750	0.0962	0.2622	2.3737
32	1.2920	1.0022	1.4998	0.4438	0.6964	0.2847	0.4232	2.5407
34	1.3260	1.0396	1.7910	0.6213	1.1250	0.4768	0.5848	2.6814
36	1.3459	1.0604	2.0162	0.7784	1.5906	0.7419	0.7784	2.7869

38	1.3774	1.0847	2.2107	0.9284	2.1209	1.0940	1.0182	2.9100
40	1.4001	1.1020	2.3938	1.0749	2.6467	1.4453	1.2556	3.0155
45	1.4389	1.1350	2.6543	1.2780	3.2800	2.1271	1.8768	3.2089
50	1.4729	1.1657	2.7741	1.3554	4.0572	2.5844	2.4036	3.3583
55	1.4951	1.1942	2.8488	1.4540	4.3667	2.8579	2.8078	3.4726
60	1.5056	1.2136	2.9017	1.5421	4.6445	3.1116	3.1937	3.5605
65	1.5123	1.2245	2.9196	1.5854	4.9345	3.2622	3.4404	3.6133
70	1.5153	1.2323	2.9302	1.6249	5.2123	3.4049	3.6787	3.6572
75	1.5125	1.2329	2.9517	1.6179	5.4038	3.4742	3.8363	3.6748
80	1.5096	1.2335	2.9732	1.6109	5.5966	3.5439	3.9950	3.6924
85	1.5056	1.2331	2.9418	1.6303	5.5881	3.5884	4.0918	3.6968
90	1.4979	1.2298	2.9033	1.6458	5.5662	3.6245	4.1793	3.6924
95	1.4908	1.2223	2.8982	1.6112	5.5650	3.6159	4.1900	3.6748
100	1.4837	1.2148	2.8932	1.5764	5.5638	3.6072	4.2007	3.6572
105	1.4682	1.2080	2.8667	1.5611	5.5801	3.5636	4.2048	3.6309
110	1.4562	1.2042	2.8470	1.5495	5.6100	3.5284	4.2192	3.6133
115	1.4492	1.1962	2.8110	1.5211	5.5690	3.4919	4.1759	3.5869
120	1.4388	1.1854	2.7681	1.4888	5.5144	3.4469	4.1225	3.5518
125	1.4283	1.1746	2.7251	1.4565	5.4596	3.4017	4.0689	3.5166
130	1.4163	1.1639	2.6932	1.4314	5.3752	3.3618	4.0135	3.4814
135	1.4043	1.1533	2.6614	1.4062	5.2907	3.3220	3.9581	3.4463
140	1.3923	1.1426	2.6295	1.3810	5.2060	3.2821	3.9026	3.4111
145	1.3803	1.1319	2.5976	1.3557	5.1212	3.2422	3.8470	3.3759
150	1.3612	1.1154	2.5522	1.3233	5.0098	3.1855	3.7715	3.3232
160	1.3322	1.0944	2.4644	1.2756	4.8042	3.0286	3.6513	3.2441
180	1.2852	1.0599	2.3205	1.1887	4.4574	2.7483	3.4410	3.1122
200	1.2493	1.0300	2.2316	1.1063	4.2248	2.5177	3.2616	3.0067
250	1.1456	0.9497	1.9681	0.9576	3.4565	2.1835	2.7221	2.7166
300	1.0619	0.8793	1.7666	0.8326	3.0270	1.9353	2.3720	2.4880
350	0.9827	0.8047	1.5719	0.7281	2.5458	1.6659	2.0860	2.2682
400	0.9227	0.7458	1.4073	0.6372	2.1109	1.4274	1.8395	2.0924
450	0.8594	0.6992	1.2965	0.5766	1.8821	1.2815	1.6519	1.9429
500	0.8117	0.6654	1.2090	0.5262	1.6866	1.1582	1.4935	1.8286
550	0.7643	0.6254	1.1246	0.4814	1.5572	1.0941	1.3740	1.7143
600	0.7287	0.5950	1.0574	0.4436	1.4513	1.0470	1.2751	1.6264
700	0.6650	0.5416	0.9327	0.3889	1.2757	0.8908	1.0770	1.4682
800	0.6044	0.4979	0.8561	0.3463	1.0228	0.7905	0.9550	1.3363
900	0.5662	0.4614	0.7834	0.3230	0.9811	0.6461	0.8504	1.2396
1000	0.5418	0.4386	0.7359	0.3028	0.9165	0.6170	0.7841	1.1781

The partial ionization cross section normalized to normalized to the total ionization cross sections measured by Rapp and Englander Golden [131], and by taking into account the fitted data near threshold are illustrated in figure III-4.

Table III-5: The fitted parameters of partial ionization cross sections near threshold

	a_1 (Å^2)	a_2	ε_{th} (eV)	ε_l (eV)
Reaction 8	2.4480	1.5041	12.63	15
Reaction 9	1.5127	1.2512	14.25	17.5
Reaction 10	0.0992	1.5727	15.1	19.5
Reaction 11	0.2159	2.8431	19.9	30
Reaction 12	0.0389	3.9286	19.6	30
Reaction 13	0.0020	0.7840	20.1	30
Reaction 14	0.0869	2.5720	18.0	30

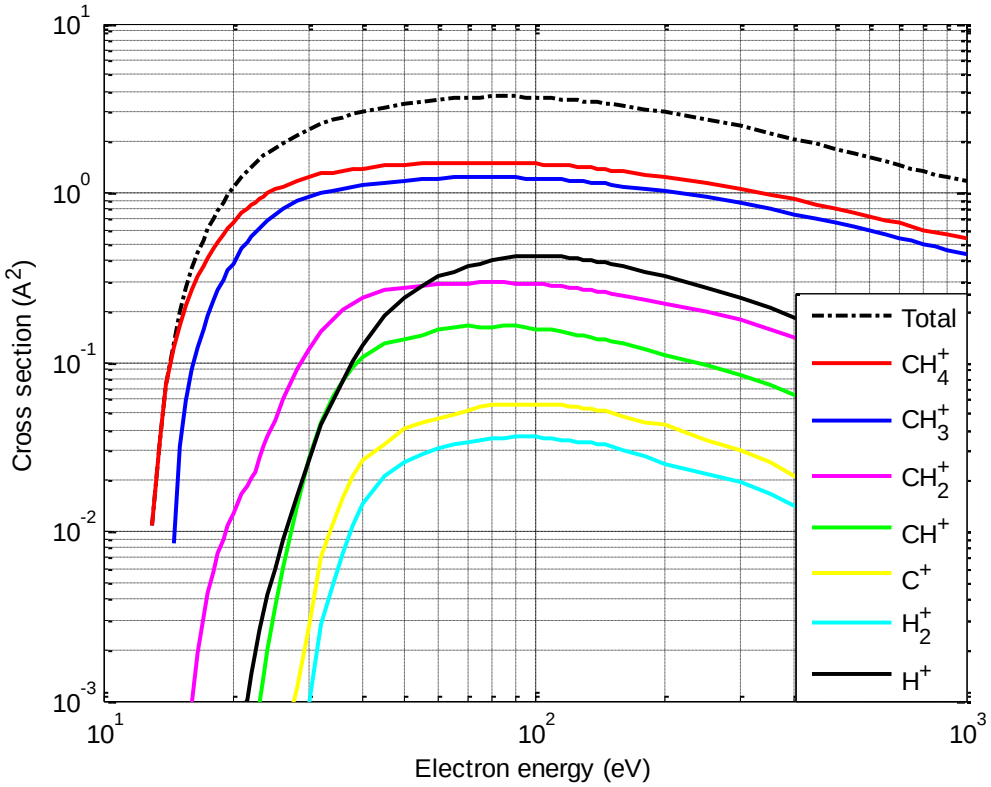

Fig. III-4: Partial dissociative ionization cross sections of the methane molecule

III.3.4. Dissociation cross section

The excited states of methane not live a long time, and all the excited molecules lead to dissociate into fragments [101, 105]. In practice, there are four important channels, which can be defined by the production of CH_3, CH_2, CH, and C. For electron energy higher than 50 eV, Winters 1975 [98] showed that there is a trend between the total dissociative and the total ionization cross sections of the methane molecule, and the dissociative ionization cross section is approximately one half of the total ionization cross section. This is explained by the simple symmetry of the electronic structure of the CH_4 molecule, and by the wide gap between the first excited electronic state and the fundamental state [66]. In the literature, in addition to total dissociative cross section (into neutrals fragments and neutrals ions fragments), we found the measured cross sections for the production of CH_3 [71], which correspond to reactions 4 and 14 in table III-1, the interpolation of this data is shown in figure III-5. By taking into account the remarks of Winters 1975[98] and the work of Erwin *et al.* [66], [114], we have considered that each ratio between the partial dissociative cross section and the total dissociative cross section into neutrals is equal to a corresponding ratio between the partial dissociative ionization cross section and the total dissociative ionization cross section. In table III-1, reaction 4 correspond to reactions 9 and 14, reaction 5 correspond to

reactions 10 and 13, reaction 6 correspond to reaction 11, and reaction 7 correspond to reactions 12. These Homologues allows us to write the following relations:

$$\begin{cases} \dfrac{\sigma_4}{\sigma_{nd}} = \dfrac{\sigma_9 + \sigma_{14}}{\sigma_{id}} \\ \dfrac{\sigma_5}{\sigma_{nd}} = \dfrac{\sigma_{10} + \sigma_{13}}{\sigma_{id}} \\ \dfrac{\sigma_6}{\sigma_{nd}} = \dfrac{\sigma_{11}}{\sigma_{id}} \\ \dfrac{\sigma_7}{\sigma_{nd}} = \dfrac{\sigma_{12}}{\sigma_{id}} \end{cases} \quad \text{(III-4)}$$

where σ_i is the cross section of the reaction i in the table III-1, σ_{nd} and σ_{id} are respectively the total dissociative cross sections to neutrals, and the total dissociative ionization cross sections. For the calculation of the different partial dissociative cross section σ_4, σ_5, σ_6, and σ_7, we must first calculate σ_{nd} by using the first equality of the equations system (III-4).

$$\begin{cases} \sigma_{nd} = \dfrac{\sigma_4}{\sigma_9 + \sigma_{14}} \sigma_{id} \\ \sigma_4 = \sigma_{CH_3} - \sigma_{14} \end{cases} \quad \text{(III-5)}$$

where σ_{CH3} is the cross sections of CH_3 production, which is calculated by the interpolation of the measurement data (Fig. III-5), then σ_5, σ_6, σ_7 can be calculated by using the following relations:

$$\begin{cases} \sigma_5 = \dfrac{\sigma_{nd}}{\sigma_{id}} \left(\sigma_{10} + \sigma_{13} \right) \\ \sigma_6 = \dfrac{\sigma_{nd}}{\sigma_{id}} \sigma_{11} \\ \sigma_7 = \dfrac{\sigma_{nd}}{\sigma_{id}} \sigma_{12} \end{cases} \quad \text{(III-6)}$$

The partial dissociative cross sections obtained are valid for electron energy higher than 50 eV, and to get the data from the threshold, we have used the following interpolation function.

$$\sigma_i(\varepsilon) = a_1 \left(\frac{\varepsilon_{th}}{\varepsilon} \right)^{a_2} \left(1 - \left(\frac{\varepsilon_{th}}{\varepsilon} \right)^{a_3} \right)^{a_4}, i = 4,5,6,7 \quad \text{(III-7)}$$

In equation III-7 σ_i: represent the partial dissociative cross section in $Å^2$, ε_{th}: threshold energy (eV), ε: electron energy (eV), and a_1, a_2, a_3, a_4 are the interpolation parameters, they are reported in table III-6.

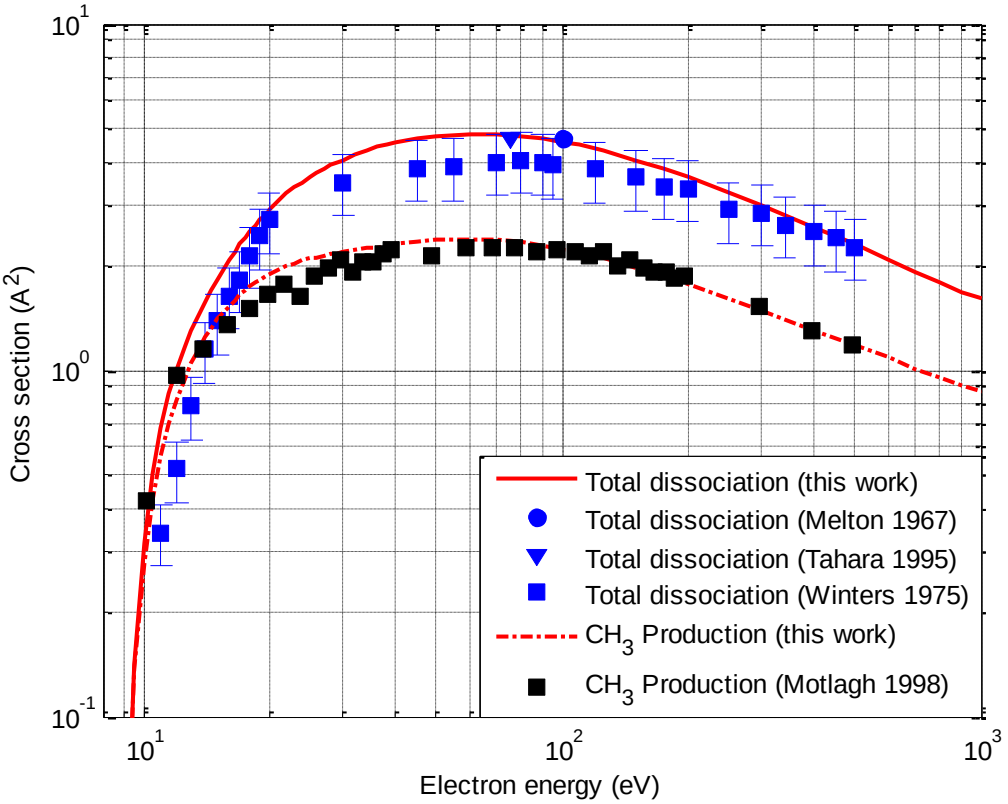

Fig. III-5: Total dissociative and CH_3 production cross sections, the measurement data from references [96], [98], [133].

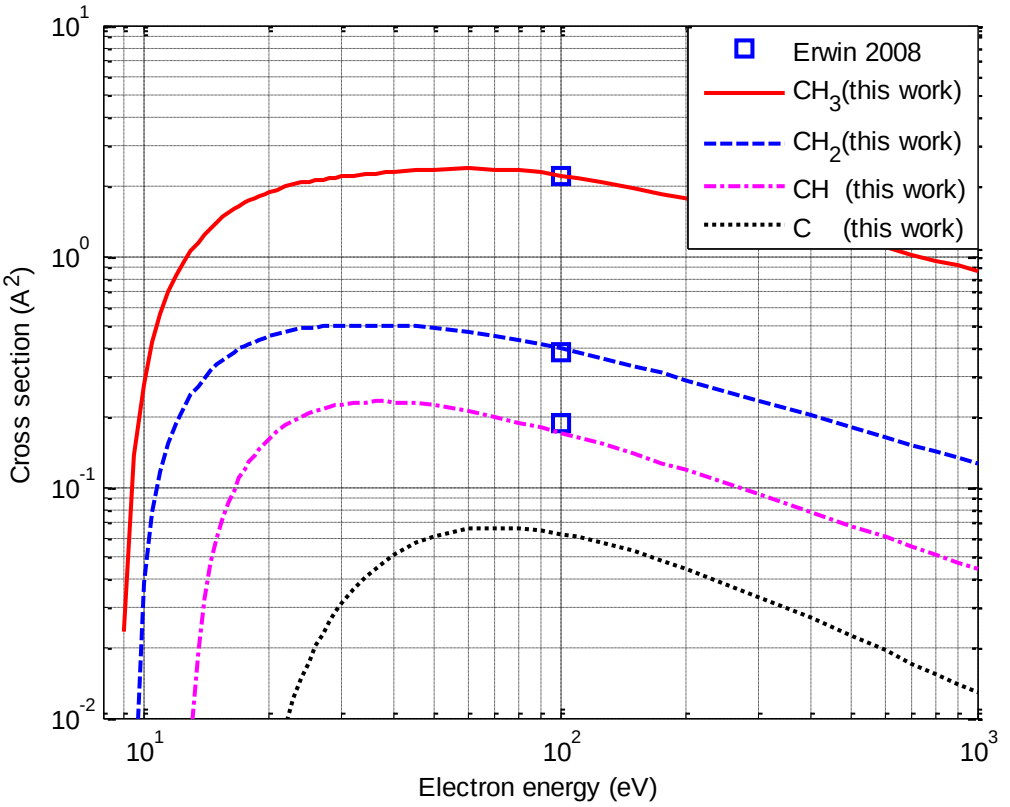

Fig. III-6: Cross section of : CH_3, CH_2, CH, and C production by electron impact dissociative collisions of the methane molecule, square data from references. [114].

Figure III-6 showed the cross sections of CH_3, CH_2, CH, and C production by electron impact dissociative collisions of the methane molecule. Noting that the radical CH_3 can be produced by reaction 4 and by the reaction 14, and the radical CH_2 can be produced by reaction 5 and by the reaction 13, contrary, both of CH and C can be produced only by one reaction for each one, which are respectively reaction 6 and reaction 7.

Table III-6: Fitted parameters of Partial dissociative cross sections

	Reaction 4	Reaction 5	Reaction 6	Reaction 7
ε_{th} (eV)	8.8	9.4	12.5	14
a_1 (Å^2)	4.9441	1.2903	0.7185	0.5681
a_2	0.3863	0.5079	0.6362	0.8807
a_3	1.4973	1.3305	1.5057	4.0006
a_4	1.2794	1.2262	1.2796	1.1164

III.4. Electron swarm parameters in methane

After the choice of the cross sections for different collisional processes between the electrons and methane molecules, and in the order to validate this recommended set of cross sections, we show in the following figures a comparison between the transport coefficients calculated by using our cross-sections to those measured by different authors.

III.4.1. Calculation of the swarm parameters through Boltzmann equation

The Boltzmann equation for a set of electrons in an ionized gas under the electric field effect is given by the following equation:

$$\frac{\partial f_e}{\partial t} = \mathbf{v}.\nabla f_e - \frac{e}{m_e}\mathbf{E}.\nabla_v f_e = C\left[f_e\right] \qquad \text{(III-8)}$$

where f_e is the electron distribution function in the six-dimensional phase space (3 for ordinary space and 3 for velocity components), $\mathbf{v}$ is electron velocity, e is the elementary charge, m_e is the electron mass, E is the electric field, ∇_v the operator of the velocity gradient, and $C[f_e]$ due to the electrons production and loss by electrons collisions with heavy species. The electron distribution function f_e is then symmetrical in the velocity space around the direction of the electric field. In the position space, the distribution function f_e can be varied only in the direction of the electric field. In this condition, and by using the spherical coordinates in the velocity space, equation (III-8) can be written as follow:

$$\frac{\partial f_e}{\partial t}+\upsilon\cos\theta\frac{\partial f_e}{\partial z}-\frac{e}{m_e}E\left(\cos\theta\frac{\partial f_e}{\partial \upsilon}+\frac{\sin^2\theta}{\upsilon}\frac{\partial f_e}{\partial\cos\theta}\right)=C\left[f_e\right] \qquad \text{(III-9)}$$

where υ is the velocity amplitude, θ is the angle between the velocity and the direction of the electric field and z is the position along this direction. The electron distribution function f_e in equation (III-9) depends on four coordinates: υ, θ, t and z. In the case of stable state where the electric field and the electron distribution function are stationary, the distribution can be developed in Legendre polynomial terms of cosθ (expansion of spherical harmonics).

The first two-term approximation of the distribution function f_e can be written as flow:

$$f_e\left(\upsilon,\cos\theta,z,t\right)=f_{e,0}\left(\upsilon,z,t\right)+f_{e,1}\left(\upsilon,z,t\right)\cos\theta \qquad \text{(III-10)}$$

where $f_{e,0}$ is the isotropic part of the electron distribution function f_e and $f_{e,1}$ is the anisotropic perturbation. Note that θ is defined relative to the direction of the electric field, so $f_{e,1}$ is negative, the electron distribution function f_e is normalized as:

$$\iiint_{\upsilon} f_e\,\mathrm{d}^3\upsilon=4\pi\int_0^{\infty}f_{e,0}\upsilon^2\mathrm{d}\upsilon=n_e\left(z,t\right) \qquad \text{(III-11)}$$

where n_e is the electrons density number. By substituting equation (III-10) in equation (III-9), multiplying by the respective Legendre polynomials (1 and cosθ), and integrating on cosθ, we obtained the following equations:

$$\begin{aligned}&\frac{\partial f_{e,0}}{\partial t}+\frac{\gamma}{3}\left[\sqrt{\varepsilon}\frac{\partial f_{e,1}}{\partial z}-\frac{1}{\sqrt{\varepsilon}}\frac{\partial}{\partial\varepsilon}\left(\varepsilon E f_{e,1}\right)\right]=C_0\\&\frac{\partial f_{e,1}}{\partial t}+\gamma\sqrt{\varepsilon}\left[\frac{\partial f_{e,0}}{\partial z}-E\frac{\partial f_{e,0}}{\partial\varepsilon}\right]=-N\sigma_m\sqrt{\varepsilon}\,f_{e,1}\end{aligned} \qquad \text{(III-12)}$$

where $\gamma=(2e/m_e)^{1/2}$ is a constant and $\varepsilon=(\upsilon/\gamma)^2$ is the electron energy in electron-volts, and N is the neutral density. The right side of the first equation (III-12) represents the change of $f_{e,0}$ due to collisions. The right side of the second equation (III-12) contains the total momentum transfer cross-section σ_m consisting of the contributions of all possible processes k with gas particles:

$$\sigma_m=\sum_k p_k\sigma_k \qquad \text{(III-13)}$$

where p_k is the molar fraction of the target species of the collision process; realize that the gas can be a mixture of different species, including excited states. For elastic collisions, σ_k is the

moment transfer cross section [134], taking into account the possible anisotropy of elastic scattering. For inelastic collisions, σ_k is the total cross section, assuming that all momentum is lost in the collision, and after the collision, the remaining electronic velocity collision is scattered isotropically.

The Equation (III-12) can be simplified by making assumptions about the temporal and spatial dependence of $f_{e,0}$ and $f_{e,1}$. In general, f_e cannot be constant in time and space because some collision processes (ionization, attachment) do not retain the total number of electrons. In the references [101, 104, 134, 135] there is a simple technique proposed to roughly describe the effects of net electron production in swarms. By this technique, the distribution function f_e can be separated from its dependence on time and space.

$$f_{e,0,1}(\varepsilon,z,t)=\frac{1}{2\pi\gamma^3}F_{e,0,1}(\varepsilon)n_e(z,t) \tag{III-14}$$

where the electron distribution energy $F_{e,0,1}$ is constant in the time and the space, and its normalization is given by the following expression:

$$\int_0^\infty \sqrt{\varepsilon}F_{e,0}(\varepsilon)\mathrm{d}\varepsilon=1 \tag{III-15}$$

In the case of exponential temporal growth without spatial dependence corresponds to the experiences of Pulsed Townsend [136]. The temporal growth rate of the electrons density is equal to the net production frequency (ν_i), it given by the following equation:

$$\frac{1}{n_e}\frac{\partial n_e}{\partial t}=\overline{\nu_i}=N\gamma\int_0^\infty\left(\sum_{k_i}p_{k_i}\sigma_{k_i}-\sum_{k_a}p_{k_a}\sigma_{k_a}\right)\varepsilon F_{e,0}\mathrm{d}\varepsilon \tag{III-16}$$

where the sum is on the processes of ionization and attachment, we recall that p_k is the molar fraction of the target species of the collision process k. From equation (III-12), the anisotropic part of the electron energy distribution function becomes:

$$\begin{aligned}F_1&=\frac{E}{N}\frac{1}{\tilde{\sigma}_m}\frac{\partial F_{e,0}}{\partial\varepsilon}\\ \tilde{\sigma}_m&=\sigma_m+\frac{\overline{\nu_i}}{N\gamma\sqrt{\varepsilon}}\end{aligned} \tag{III-17}$$

By substituting $F_{e,1}$ (eq.III-17) in isotropic part of equation (III-12), we find:

$$-\frac{\gamma}{3}\frac{\partial}{\partial\varepsilon}\left[\left(\frac{E}{N}\right)^2\frac{\varepsilon}{\tilde{\sigma}_m}\frac{\partial F_{e,0}}{\partial\varepsilon}\right]=\tilde{C}_0+\tilde{R} \tag{III-18}$$

where the collision term is given by the following expression:

$$\tilde{C}_0 = 2\pi\gamma^3\sqrt{\varepsilon}\frac{C_0}{Nn}$$
$$\tilde{R} = -\frac{\bar{\nu}_i}{N}\sqrt{\varepsilon}F_0 \qquad \text{(III-19)}$$

The case corresponds to Steady State Townsend experiments [136]. While the electrons drift against the electric field, their flux and density increase exponentially with a constant spatial growth rate α (Townsend coefficient), which is related to net electron production by:

$$\alpha = -\frac{1}{n_e}\frac{\partial n_e}{\partial z} = -\frac{\bar{\nu}_i}{\omega} \qquad \text{(III-20)}$$

where the average velocity ω is determined by $F_{e,1}$, it is constant in space with a negative value. By substituting α (eq.III-20) in anisotropic part of equation (III-12), we find:

$$F_{e,1} = -\frac{1}{\sigma_m}\left(\frac{E}{N}\frac{\partial F_{e,0}}{\partial\varepsilon} + \frac{\alpha}{N}F_{e,0}\right) \qquad \text{(III-21)}$$

Finally, the isotropic part of the electron energy distribution function (eq.III-12) can be written as follows:

$$-\frac{\gamma}{3}\frac{\partial}{\partial\varepsilon}\left[\left(\frac{E}{N}\right)^2\frac{\varepsilon}{\sigma_m}\frac{\partial F_{e,0}}{\partial\varepsilon}\right] = 2\pi\gamma^3\sqrt{\varepsilon}\frac{C_0}{Nn} + \frac{\alpha}{N}\frac{\gamma}{3}\left[\frac{\varepsilon}{\sigma_m}\left(2\frac{E}{N}\frac{\partial F_{e,0}}{\partial\varepsilon}\frac{\alpha}{N}F_0\right) + \frac{E}{N}F_{e,0}\frac{\partial}{\partial\varepsilon}\left(\frac{\varepsilon}{\sigma_m}\right)\right] \qquad \text{(III-22)}$$

The first Townsend coefficient α can be found by combining equation (III-21) and equation (III-20):

$$\omega = -\frac{1}{3}\gamma\int_0^\infty F_1\varepsilon\,\mathrm{d}\varepsilon = -\mu E + \alpha D = -\frac{\bar{\nu}_i}{\alpha} \qquad \text{(III-23)}$$

This leads to:

$$\alpha = \frac{1}{2D}\left(\mu E - \sqrt{(\mu E)^2 - 4D\bar{\nu}_i}\right) \qquad \text{(III-24)}$$

where μ et D are respectively, the mobility and the diffusion coefficient, then, the reduced mobility μN and characteristic energy (reduced diffusion DN) can be calculated by the following expressions:

$$\mu N = -\frac{\gamma}{3}\int_0^{\infty}\frac{\varepsilon}{\tilde{\sigma}_m}\frac{\partial F_0}{\partial \varepsilon}\mathrm{d}\varepsilon$$
$$DN = \frac{\gamma}{3}\int_0^{\infty}\frac{\varepsilon}{\tilde{\sigma}_m}F_0\mathrm{d}\varepsilon \qquad \text{(III-25)}$$

III.4.2. Comparison between the calculated and measured swarm parameters

Figure III-7 show the calculated reduced electrons mobility as a function of reduced electric field in methane by using our cross sections (red continuous curve) and by using the data of Davies [101] (black dashed curve). The reduced mobility calculated by the Davies cross sections shows a deviation to the measurements for a reduced electric field between 0.1 Td and 1 Td and the same for high reduced electric field (>300 Td), while our recommended data give an acceptable reduced mobility in a comparison with the experiments data.

Figure III-8 shows that the reduced diffusion calculated by our data is in a good agreement with the measurements in a comparison to that calculated by using the cross sections of Davies, where this last shows a deviation with the experiment values for a reduced electric field between 0.1 Td and 1 Td.

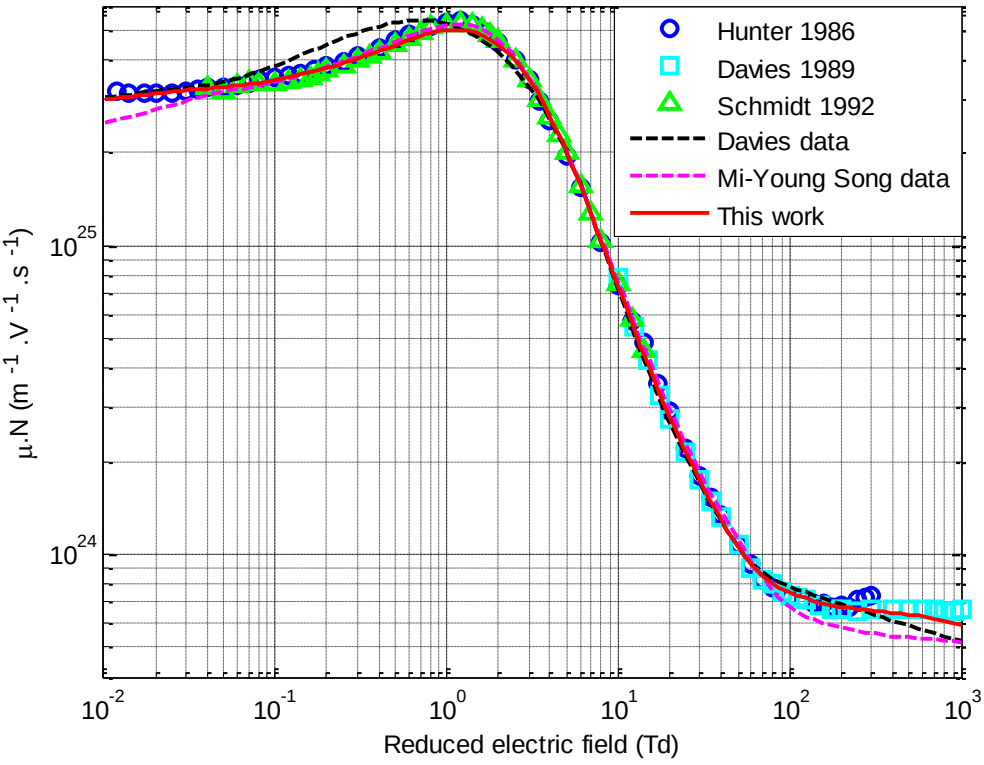

Fig. III-7: Reduced electron mobility as a function of reduced electric field, the measurement data are from references [101], [109], [137].

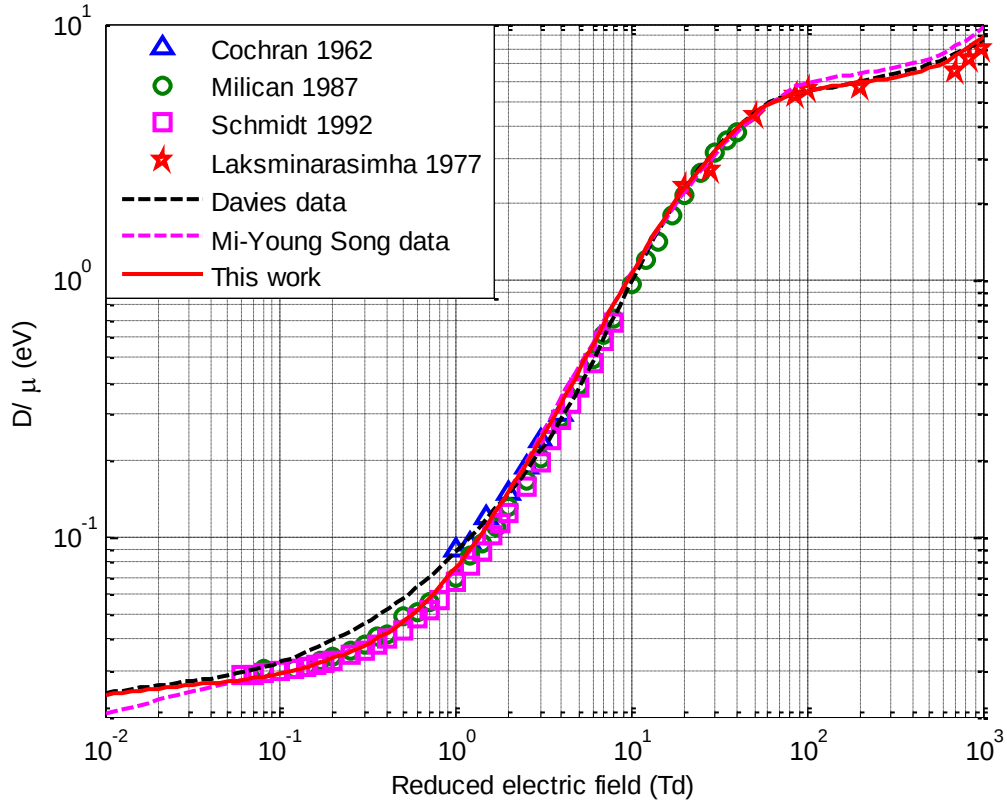

Fig. III-8: Reduced diffusion as a function of reduced electric field, the measurement data are from references [136-138].

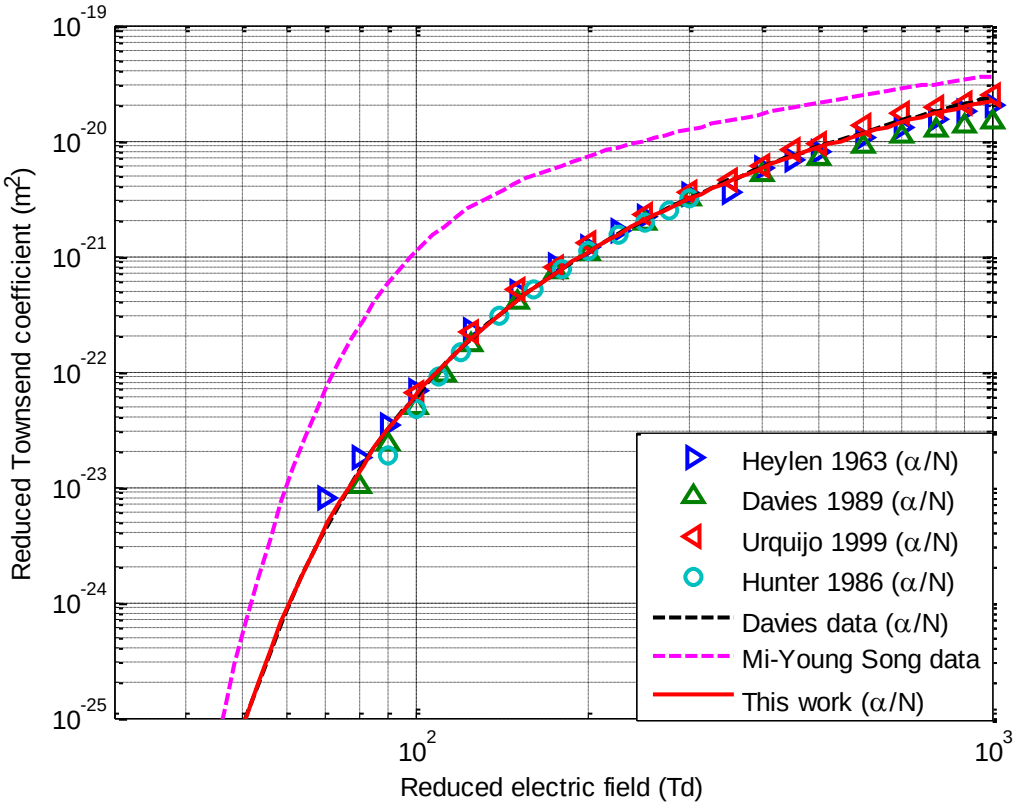

Fig. III-9: *Reduced Townsend ionization coefficient as a function of reduced electric field, the measurement data are from references [101], [109], [138], [139].*

Figure III-9 shows Ionization reduced *Townsend* coefficients as a function of reduced electric field, both of the ionization Townsend coefficients calculated by using our cross sections or by using Davies cross sections are in agreement with experiment values.

Finally, in figure III-10 and figure III-11 we show a partial dissociative rates and partial ionization rates, respectively. These rates are calculated through solving the Boltzmann equation, then they interpolated according to equation (III-26) to use easily in fluid models. The fitted parameters are reported in the table III-7.

$$k\left(T_e\right)=\alpha\left(T_e-T_c\right)^{\beta} e^{-\frac{\gamma}{T_e-T_c}} \quad T_e > T_c \tag{III-26}$$

where α, β, γ: are the fitted parameters, and T_e is the electron temperature in eV.

Table III-7: Parameters of partial dissociative and partial ionization rates

Production	α ($m^3.s^{-1}eV^{-\beta}$)	β	γ (eV)	T_c(eV)
CH_3 +H	6.768E-14	0.0578	9.17	1.167
CH_2+H_2	1.752E-14	0.0073	9.15	1.261
CH+ H_2+H	1.928E-14	-0.2489	13.90	1.359
C+2 H_2	2.011E-15	0.0649	18.04	1.573
CH_4^+	3.446E-14	0.1555	12.12	1.573
CH_3^+ + H	4.277E-14	0.0208	14.40	1.573
CH_2^+ + H_2	3.527E-15	0.3910	16.74	1.689
CH^++ H_2+H	4.954E-15	0.0687	21.47	1.945
C^+ + 2 H_2	1.887E-15	0.0157	24.25	1.945
H_2^+ + CH_2	9.620E-16	0.1709	27.25	1.505
H^+ + CH_3	1.327E-15	0.7529	19.72	1.861

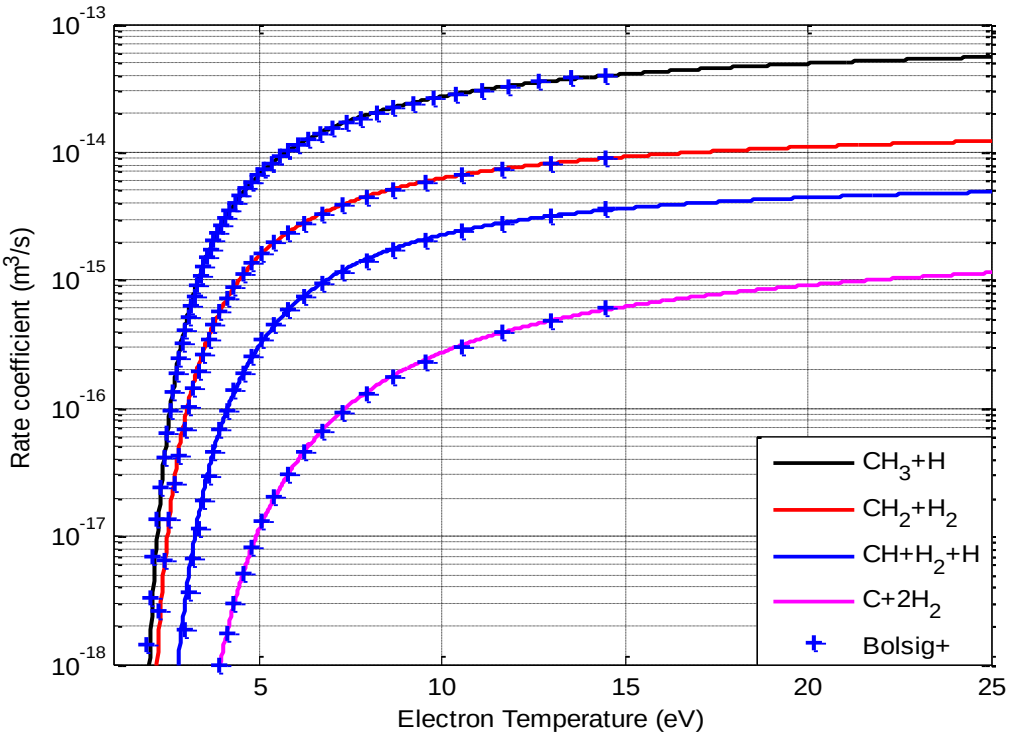

Fig. III-10: Rate coefficients of the partial dissociation into neutrals

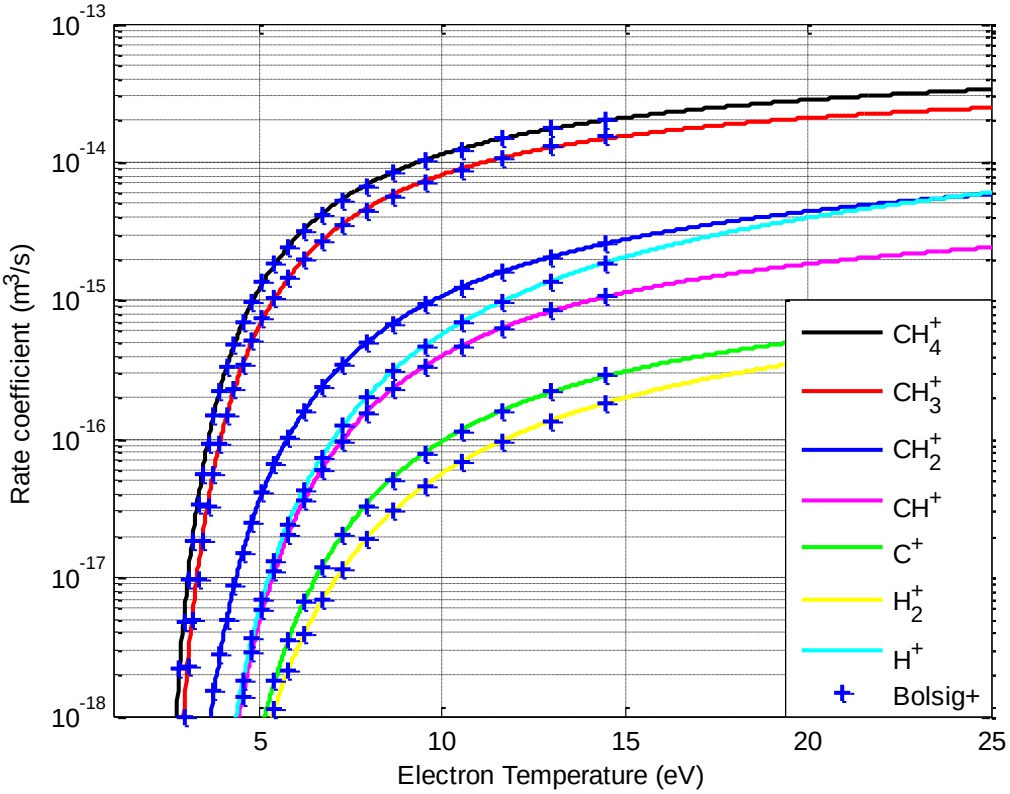

Fig. III-11: Rate coefficients of the partial ionizations

III.5. Conclusion

The main results of this chapter are the revision of the electron collision cross-section for methane molecules, where the collision processes involved are: the elastic momentum transfer, two composite modes of vibration, all partial dissociations, and all partial ionizations. This set of collision cross-sections have been validated through a comparison between the transport coefficients calculated by using this set of data and the measurements published in the literature. The work demonstrates that the calculation of the rate coefficients for the partial dissociative collisions into neutrals and the partial ionization collisions, when fitted, can be used as input for fluid models.

In the next two chapters we use these cross sections and other reactions described for the simulation of the capacitively coupled and inductively coupled discharges in methane plasma.

CHAPTER IV

MODELING OF CAPACITIVELY COUPLED PLASMA IN METHANE

IV.1. Introduction

The Radio-Frequency Capacitive Coupled Plasma RFCCP is used in many applications such as etching, sputtering, plasma enhanced chemical vapor deposition (PECVD), in biomedical and medical applications, such as sterilization, wound healing, semiconductor manufacturing and the production of solar cells [140-148], a detailed overview made by [140,141].

The aim of this chapter is the detailed description and modeling of capacitive coupled discharge plasma in methane by presenting the most existing and dominant species. For this, in this chapter we show a results for 1D simulation and comparison between 300 reactions and 100 reactions in the aim to know the governing reactions. In comparison with 2D, 1D has a great advantage in obtaining the characteristics of the plasma and the density of the species, in addition the reduction of the calculation time [78].For this configuration (CCP) we use the fluid model, in this approach the moments of the Boltzmann equation are coupled by the Poisson equation, this model is very used to predict the dominant reactions and the most existing species in methane. This model is used in many works such as [149-157].

IV.2. Overview about the capacitively coupled plasma in methane

Many works interested to the study of capacitively coupled configuration, either numerically or experimentally for many kind of pure gases or mixture, in this short overview, we interest to some studies of capacitively coupled discharge in methane plasma.

In the study of Chien-Wei Chang et al [158], an implementation of a fluid model including a chemical reaction mechanism for methane plasmas. Employing a finite-difference method, to solve for the low-pressure RF plasma phase in a parallel-plate reactor via the local field equilibrium approximation model, based on which the distribution of the electrons and ions along with the electric potential is obtained. The results show good qualitative agreement with those of N. Nagayama et al [159]. The densities of species are ordered as following CH_4, H_2, H, CH_3, C_2H_5 and CH_4^+.

According to the study of Tachibana et al [86], the most abundant neutrals and radicals are CH_4, H_2, C_2H_4, CH_3, C_2H_2 and H, for ions CH_5^+, $C_2H_5^+$, CH_4^+, CH_3^+ and H_3^+. The result of A.

Rhallabi and Y. Catherine [83] show that CH_4, C_2H_6, H_2, H and CH_3 are the major neutral species, and CH_5^+, $C_2H_5^+$, CH_4^+ and CH_3^+ are the major ionic species.

It is found in the study of D. Herrebout et al [78] that C_2H_6, C_3H_8, C_2H_4, and C_2H_2 are also present at high densities with CH_4 and H_2 (inlet gas). The main radical in the plasma is CH_3. At low pressure (eg 0.14 Torr) the most important ion is found to be CH_5^+, at higher pressure (eg 0.5 Torr) $C_2H_5^+$ becomes the dominant ion.

As we can see that there are no great agreement in the results, for radicals and neutrals, but we conclude that in general the major radical species are H, CH_3, C_2H_5 and C_2H_3. For the neutrals, the most existing are CH_4, H_2, C_2H_4, C_2H_6 and C_2H_2. But there are great agreement for the order of the existing ions; $C_2H_5^+$ or CH_5^+, CH4+ and CH_3^+ are the most major ionic species but in two orders of decades or more lowest than radicals and neutrals.

IV.3. Operating principle of a reactor plasma capacitively coupled

IV.3.1 Schematic diagram

Plasma are produced by supplying energy to matter until a significant fractional ionization is obtained.

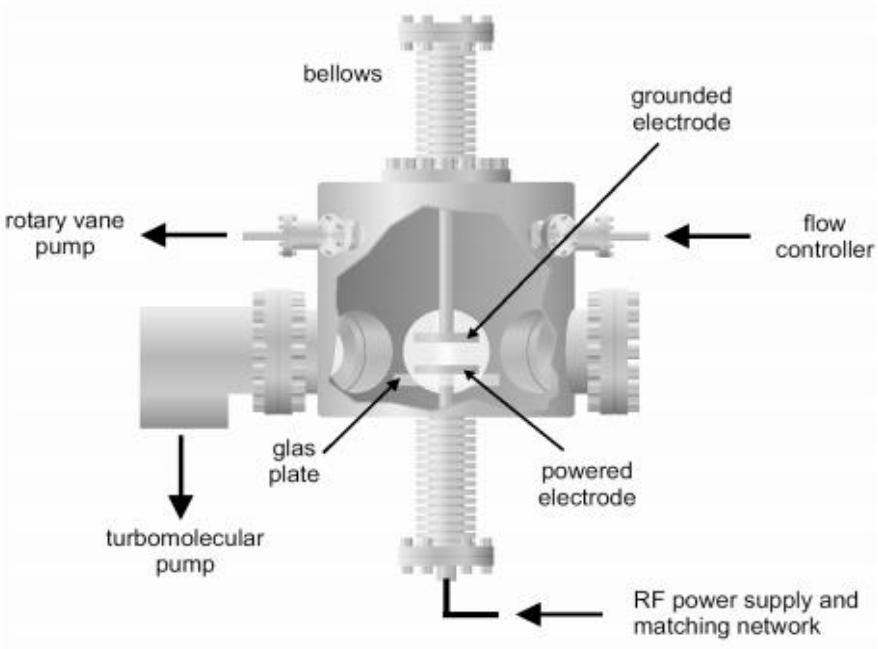

Fig. IV-1 Capacitively coupled plasma reactor..

The gas is transformed to a plasma when the addition of heat or other energies either in electric or electromagnetic form causes a significant number of atoms to release some or all of their electrons, all these elements (electron-neutral, neutral-neutral, and neutral-charged) exhibit collective behavior; this state called plasma.

Capacitive radio frequency (RF) discharges are very popular, both in laboratory research for the production of low-temperature plasmas, and industry, where they are commonly used for thin film deposition and surface etching. The typical capacitive RF discharge consists of two parallel electrodes as shown in the figure IV-2, placed in a vacuum vessel. The electrodes are powered with voltage from a RF power source. The working gas, fed into a system, gets ionized by electrons, accelerated in the RF electric field, producing the weekly-ionized plasma with an ionization degree of about 10^{-6}–10^{-4}. The typical distance between the electrodes is of order 1-10 cm. The driving RF voltage is usually about 100-1000V with a frequency between 1 and 100 Mhz. The pressure of the working gas, depending on application of discharge, varies in the range of 1-1000 Pa [160-164].

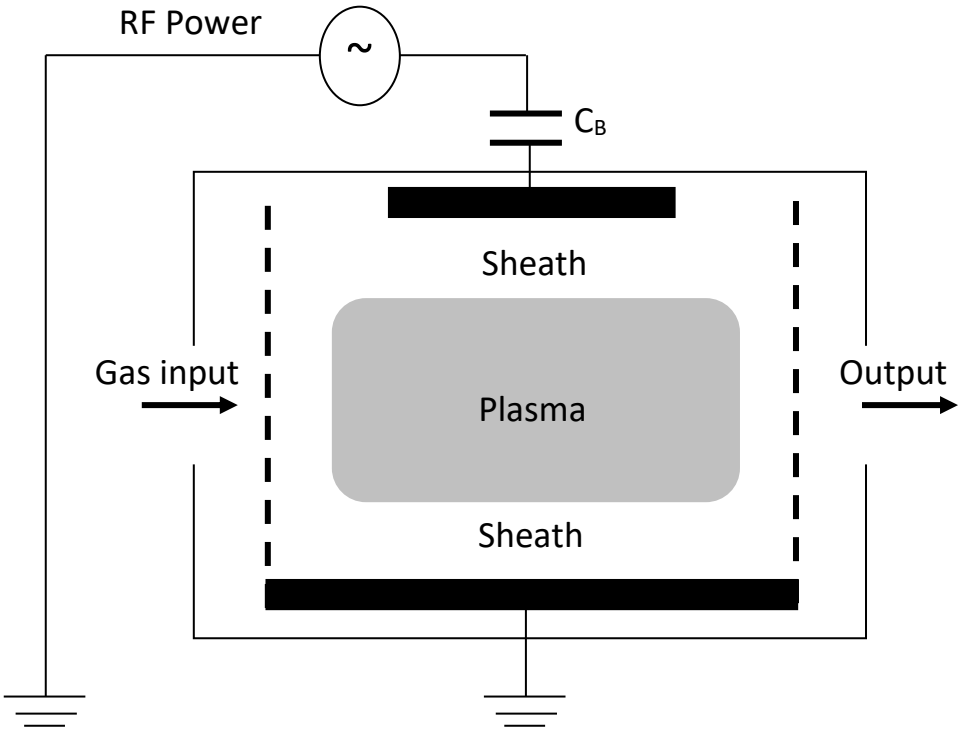

Fig. IV-2: Diagram of a capacitively coupled reactor

An RF CCP is driven by RF power supply, typically at 13.56 MHz. As shown in Figure IV-2, one of the electrodes is connected to the power supply, the other is grounded.

Figure IV-1 presents the scheme of one such set-up, which is used in the Laser and Plasma Physics Group, Bochum University for the investigation of plasma-chemistry processes in low temperature plasmas. In this set-up the disk electrodes with spacing d = 4 cm are powered with RF voltage with frequency 13.56 MHz. RF power input in the system varies in the range of 5-100 W. Mixtures of methane and oxygen at Pressures 10-1000 Pa are normally used as the working gas. For the typical operation parameters a plasma with density n_e~10^9-10^{10}cm-3 and electron temperature T_e~3 eV is obtained in the discharge. The electrodes in an CCP reactor are parallel and in general circular and separated by a distance of few centimeters and placed in a vacuum chamber which is introduced a gas (or a mixture of gases) of low pressure. The discharge is limited by the reactor walls, which can be conductor or insulating. Through the electrode connected to the electric power, an electric field is generated between electrodes, the atoms and molecules are ionized and release electrons. An electronic avalanche is produced when the electric field is strong enough and the gas becomes electrically conductive, this appears in form of light emission from excited atoms and molecules in the gas and several process are produced like ionization, dissociation, excitation…etc. From the schematic diagram we can distinguish the following parameters of the control of the capacitive discharge:

- The excitation frequency; The frequency range is usually between 1 and 100 MHz. In the radio frequency domain, the international telecommunications authorities authorize the use of a frequency of 13.56 MHz, as well as all its harmonics.
- the pressure (or the density N of the gas) of the reactor; These sources operate at high pressures between 50 mTorr and 10 Torr (from a few mTorr in the case of etching to Torr for deposit applications)
- The electronic density; the electronic density is in the range of 10^8 -10^{10} cm^{-3}.
- The composition of the gas mixture; It can be, for example, inert gases such as argon (Ar) or helium (He) or reactive gases such as air, oxygen (O2), hydrogen (H2), nitrogen (N2), methane (CH4), silane (SiH4) or sulfur hexafluoride (SF6). Note that these two last gases are widely used in microelectronics.
- The gas flow.
- The geometry and the size of the reactor.
- The nature of the electrodes and the inter-electrode distance (as a rule of a few mm to a few cm);

IV.3.2. Operating Principle

When a radiofrequency voltage $V(t) = V_0 \sin(\omega t)$ is applied between the two electrodes of the reactor of Fig. IV-2, (V_0 is of the order of a few hundred to a few thousand volts), gets an operating regime that depends on the pulsation ω. When ω is varied from zero, first we obtain a behavior of a continuous DC discharge at each half-period. The process of secondary electrons ensures the maintenance of the discharge. For higher frequencies (f ~ Mhz), the system then progressively changes to a situation in which the secondary emission is not necessary to initiate the discharge. In this case, the majority of the electrons oscillates and maintains the discharge by gaining, cumulatively between the successive collisions on the neutrons, the kinetic energy necessary for the ionization. The electric field is the one that ensures the equilibrium between the ionization and the losses by recombination in volume or on the walls limiting the discharge. Since the radiofrequency voltage is constant throughout the circuit, it is convenient to enter it as a control parameter, and the other macroscopic adjustable parameters that ensure the operation of radio frequency discharges are [165-170]:

- the excitation frequency;
- the composition of the gas mixture;
- The pressure (or the density of the N gas) of the reactor;
- the gas flow;
- the geometry and the size of the reactor;
- the nature of the electrodes and the inter-electrode distance ;
- the heating or cooling of the electrodes (of the substrate).

IV.3.3. Equivalent electrical circuits

The discharge can be described in the form of an electrical circuit whose elements depend on parameters such as the pulsation ω, the surface of the electrodes, the density of the plasma, the size of the plasma [171,172,173,174]. The simplest model was developed by Godyak and Lieberman in the case of a homogeneous sheath where $n_i = n$ and $n_e = 0$, this model is shown in figure IV-3. In the symmetrical capacitive radiofrequency discharges, three zones will be distinguished between two coplanar electrodes; A central plasma zone (positive column) of thickness dP where there is a quasi electrical neutrality and a plasma density n and two other zones near the electrodes (sheaths) of positive space charge.

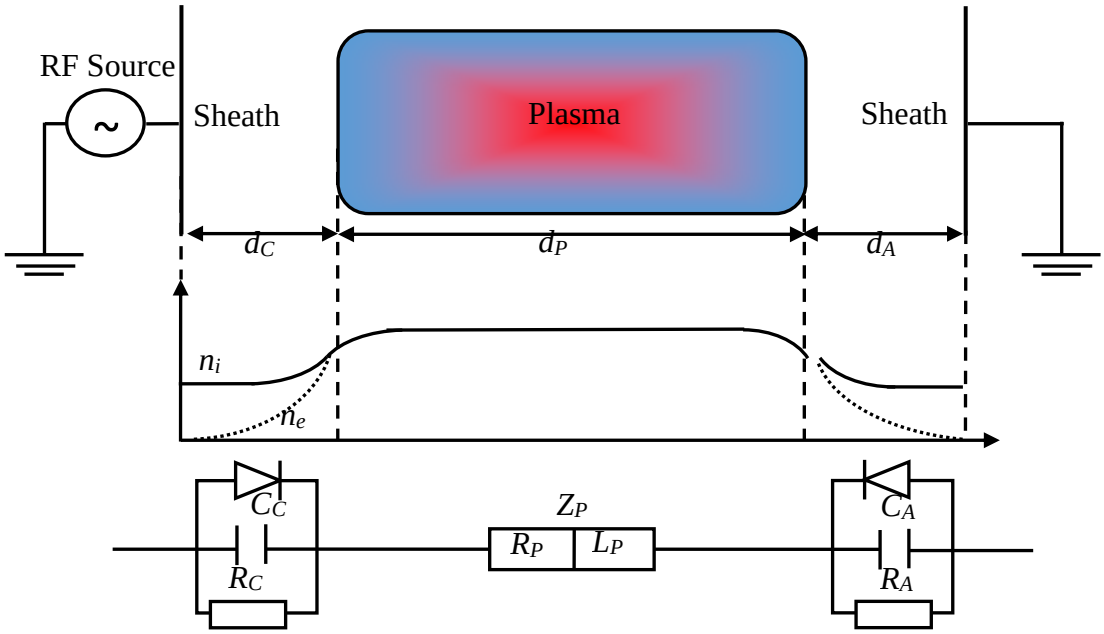

Fig. IV-3: model of a symmetrical capacitive discharge with its equivalent electrical circuit.

These sheaths are characterized by thicknesses *dC* for the cathode, and *dA* for the anode, where: $d=dP(t)+dC\ (t)+dA(t)$ constant representing the inter-electrode space. For the equivalent electrical scheme of the capacitively coupled discharge, the plasma is assigned a resistive and inductive impedance Z_p (equation III-5).

$$Y_P = \frac{1}{Z_P} = j\omega_{rf} C_P + \frac{1}{R_P + jL_P\omega_{rf}} = j\omega_{rf} C_P + \frac{1}{\frac{d_p m_e \nu_m}{n_e e^2 A_P}\left(1 + j\frac{\omega_{rf}}{\nu_m}\right)} \qquad \text{(IV-1)}$$

where : ν_m is the electron-neutral collision frequency, A_p is the area of the plasma section perpendicular to the inter-electrode axis, L_P is the inductance of the plasma, R_P the resistance of the plasma and Y_P is the admittance of plasma. The characteristic impedance Z_g of a sheath (g = C, A) can be represented by capacitance and resistance in parallel, with a diode preventing the plasma potential from falling below the potential of the electrode potential. For a pulsation ω are represented by:

$$C_g = \frac{\varepsilon_0 A_g}{d_g}$$
$$R_g = \frac{V_g}{A_g \overline{J_i}} \qquad \text{(IV-2)}$$
$$Z_g = \frac{R_g}{1 + j\omega C_g}$$

where: d_g average sheath thicknesses, A_g"effective" areas of the electrodes, R_g are derived from average values of the potential V_g, the average ion conduction current density J_i through

the sheath. The parameters (R_g, C_g and Z_g) of equivalent electrical circuit can be determined by using an identification method, the ratio of I_{depl} displacement and I_{cond} conduction currents for non-collisional sheaths is expressed by the Child-Langmuir law and the Bohm criterion :

$$\frac{I_{depl}}{I_{cond}} = R_g C_g \omega_{rf} = \frac{V_g \varepsilon_0 \omega_{rf}}{J_i d_g} \approx \frac{1}{\sqrt{2}} \left(\frac{q v_g}{k T_e} \right)^{\frac{1}{4}} \left(\frac{\omega_{rf}}{\omega_{pi}} \right) \quad \text{(IV-3)}$$

The current flowing in the plasma is therefore a conduction current. With regard to the spac charge sheath, the nature of the current depends on the excitation frequency:

- ✓ In low frequency;$\omega \ll \omega_{pi}$, the displacement current in the sheath is low compared to the conduction current, in this case the sheath is said to be resistive ($R_g C_g \ll 1$).
- ✓ In high frequency;$\omega \gg \omega_{pi}$, the mainstream is the displacement current, so the sheath is essentially capacitive ($R_g C_g \gg 1$)

IV.3.4. Main mechanisms for priming and maintaining a capacitive discharge

The maintenance of a discharge is the compensation of the losses of charged particles; electrons and ions, by mechanisms of creation ionization. Electron-ion recombination and ambipolar wall diffusion and the phenomenon of attachment in electronegative gases are the main causes of particle losses in plasma. When the creation of particles charged by ionization by electronic impact compensates for the losses, the plasma is said to be self-sustaining. The production of new charged particles takes place if the kinetic energy of the electron is greater than the atomization potential of the atom so that the energy transfer from the electron to the atom allows the ionization. In the opposite case, the collision can be translated simply by an excitation of the atom. In general, the kinetic energy of the electron may become insufficient to ensure new ionization processes. It is therefore necessary to continuously supply energy to the electrons of the plasma. In a capacitively coupled RF discharge, electrons acquire their energy through heating mechanisms that can be collisional or non-collisional.

Ohmic or collisional heating occurs when electrons exchange momentum by collision with the population of neutrals in the central plasma. The electric field in the plasma core is quite small in comparison with the field in the sheaths. This weak field is enough to "heat" the electrons, which provide additional ionization and compensate for losses. Under these conditions the positive column regime is similar to a Joule heating. The power density averaged over time, responsible for the heating of electrons in the plasma, is written:

$$P_{\Omega} = \frac{J^2 R_e}{2\sigma_p} \quad \text{(IV-4)}$$

where J is the current density and σ_p is the conductivity of the plasma.

Non-collisional heating is a phenomenon associated with sheath, for much lower pressures, the free electronic path being greater than the length of the sheath. If the electron has an initial velocity V_0 that is directed towards the sheath and that this expands with a velocity V_g, the reflected electron is accelerated by the electric field which prevails in the sheath expanding towards the plasma with a velocity $V_0 + 2Vg$. This regime is also called stochastic heating (or electron-sheath collision mechanism) because the electrons can gain but also lose energy depending on their speed relative to the sheath.

At greater pressure, we talk about the effect of surfing or waveriding. The electrons that reach from the plasma to the edge of the sheath see it move like a wave. Some of them will be carried by this wave and sent back to the plasma, when the sheath is so they will acquire kinetic energy taken to the wave. They are then very effective ionization agents.

The effect of surf and the stochastic heating are related to the oscillating movement of the sheaths. The resulting ionization, in both cases, is localized near the plasma sheath interface. The total power absorbed by the electrons in a capacitive radiofrequency discharge is therefore the sum of two powers coming from two processes, one collisional and the other non-collisional, the total power is given by:

$$P_{tot} = P_{stok} + P_{\Omega} \quad \text{(IV-5)}$$

IV.3.5. Limitations of radiofrequency capacitively coupled discharges

In this type of discharge, the densities of charged particles obtained are often low (10^8 to 10^{10} cm^{-3}), which leads to low degrees of dissociation of the plasma gas (what we will see in the simulation results in our case for methane). As a result, the ionization coefficient is low and the ion flux is therefore also low.

For other applications such as surface treatment, the substrates to be treated and the metal electrodes are immersed in the same environment, which is also the place of creation of energetic species.

Indeed, the bombardment of the electrodes by high energy ions and reactive neutrals generally leads to a considerable erosion of the surface. The reaction products are thus found in the plasma, which represents an important source of contamination. These contaminations of all kinds can be incorporated in the deposit [175-177].

IV.4. Fluid model equations of RF capacitively coupled plasma in CH_4

By applying sinusoidal electrostatic potential ($V(t)$=200sin (2π.13.56×$10^6 t$)), across a gap of 6 cm filled with low pressure (P=80 mTorr), for the methane gas.

4.1. Fluid model equations

The electron density and mean electron energy is computed by solving a pair of drift-diffusion equations.

$$\begin{aligned} &\frac{\partial}{\partial t}(n_e) + \nabla.\Gamma_e = R_e \\ &\Gamma_e = -n_e(\mu_e.E) - D_e.\nabla n_e \\ &\frac{\partial}{\partial t}(n_\varepsilon) + \nabla.[-n_\varepsilon(\mu_\varepsilon.E) - D_\varepsilon.\nabla n_\varepsilon] + \mathrm{E}.\Gamma_e = R_\varepsilon \end{aligned} \qquad \text{(IV-6)}$$

R_e is the electron source term and is given by

$$R_e = \sum_{j=1}^{M} x_j k_j N_n n_e \qquad \text{(IV-7)}$$

where x_j is the mole fraction for the target species for the reaction j, k_j is the rate coefficient for reaction j (SI unit: m^3/s), and N_n is the total neutral number density (SI unit: $1/m^3$). And R_ε is the electron energy loss is obtained by summing the collisional energy loss over all reactions.

$$R_\varepsilon = \sum_{j=1}^{p} x_j k_j N_n n_e \Delta\varepsilon_j \qquad \text{(IV-8)}$$

where $\Delta\varepsilon_j$ is the energy loss from reaction j (SI unit: V). The rate coefficients can be computed from cross section data by the following integral:

$$k_k = \gamma \int_0^\infty \varepsilon \sigma_k(\varepsilon) f(\varepsilon) d\varepsilon \qquad \text{(IV-9)}$$

where $\gamma=(2q/m_e)^{1/2}$ SI unit: $C^{1/2}/kg^{1/2}$), *me* is the electron mass (SI unit: kg), ε is energy (SI unit: V), σ_k is the collision cross section (SI unit: m^2), and f is the electron energy distribution function. In this case a Maxwellian EEDF is assumed.

For ions, only this two following equations are solved for each ion *k*

$$\frac{\partial}{\partial t}(n_k)+\nabla.\Gamma_k = R_k$$
$$\Gamma_e = -n_k(\mu_k.E)-D_k.\nabla n_k \qquad \text{(IV-10)}$$

The electrostatic field is computed by the following equation:

$$\nabla.(\varepsilon_r \nabla V) = -\frac{e}{\varepsilon_0}\left(\sum_{k=1}^{N} Z_k n_k - n_e\right) \qquad \text{(IV-11)}$$

The ions mobility is calculated by using the Dalgarno formula:

$$\mu_k = \frac{0.0438}{\sqrt{\alpha_n m_{kn}}}\frac{2.69\times10^{25}}{N_n} \qquad \text{(IV-12)}$$

where $M_{kn}=M_k.M_n/(M_k+M_n)$ is the reduced mass and α is the polarizability of the neutral.

As boundary conditions, we have the electron flux at the walls is given by the following expression:

$$n.\Gamma_e = \left(\frac{1}{2}v_{e,th^{n_e}}\right) \qquad \text{(IV-13)}$$

and the electron energy flux is calculated by:

$$n.\Gamma_\varepsilon = \left(\frac{5}{6}v_{e,th^{n_\varepsilon}}\right) \qquad \text{(IV-14)}$$

IV.4.2. Chemical model reactions

We take into account 34 species shown in Table 1 and 107 electronic impact reactions (14 with CH_4, 10 with CH_3, 8 with CH_2, 4 with CH, 1 with C, 20 with H_2, 4 with H, 17 with C_2H_6, 16 with C_2H_4 and 11 with C_2H). The model contains, in aggregate, 320 reactions (reactions and Rate Coefficient table 2 and wall reactions table 3). The electronic impact collision with methane are described in detail in the work of A. Gadoum and D. Benyoucef [180].

The rate coefficient is calculated by: $k=A.T_g^n.\exp(-E_a/RT_g)$, where T_g is the gas temperature, *R* is the gaz constnt, and *A*, *n*, and E_a are given in the table.

Table IV-1 : Reactions with Rate coefficient

N	Reaction	Rate Coefficient			Ref
		A[m^3/s.mol]	E[J/mol]	n	
1	$CH_4 + CH_2 => CH_3 + CH_3$	0.0713E-16	41988	0	184
2	$CH_4 + CH => C_2H_4 + H$	153E-16		-0.9	183
3	$CH_4 + H => CH_3 + H_2$	2.2E-26	33632	3	182
4	$CH_3 + CH_3 => C_2H_6$	4.66E-16		-0.37	184
5	$CH_3 + CH_3 => C_2H_4 + H_2$	170E-16	133030		181
6	$CH_3 + CH_3 => C_2H_5 + H$	0.5E-16	56540		184
7	$CH_3 + CH_2 => C_2H_4 + H$	0.7E-16			184
8	$CH_3 + CH => C_2H_3 + H$	0.5E-16			181
9	$CH_3 + C => C_2H_2 + H$	0.83E-16			181
10	$CH_3 + H2 => CH_4 + H$	1.1E-26	39410	2.74	183
11	$CH_3 + H => CH_2 + H_2$	1E-16	63190		184
12	$CH_2 + CH_2 => C_2H_4$	0.017E-16			185
13	$CH_2 + CH_2 => C_2H_2 + 2H$	1.8E-16	3326		183
14	$CH_2 + CH_2 => C_2H_2 + H_2$	26.3E-16	50000		183
15	$CH_2 + CH_2 => CH_3 + CH$	4E-16	41572		183
16	$CH2 + CH => C_2H_2 + H$	0.66E-16			185
17	$CH_2 + C => C_2H + H$	0.83E-16			185
18	$CH_2 + H_2 => CH_3 + H$	0.19E-16	53212	0.17	183
19	$CH_2 + H => CH + H_2$	2.2E-16			183
20	$CH + CH => C_2H_2$	2E-16			184
21	$CH + C => C_2 + H$	0.66E-16			183
22	$CH + H_2 => CH_2 + H$	5.46E-16	16155		183
23	$CH + H => C + H_2$	1.31E-16	665		184
24	$C + H_2 => CH + H$	6.64E-16	97278		184
25	$CH_4 + + CH_4 => CH_5^+ + CH_3$	11.5E-16			186
26	$CH_4^+ + H2 => CH_5^+ + H$	1.086E-16	-300	-0.14	183
27	$CH_4^+ + H => CH_3^+ + H2$	0.1E-16			183
28	$CH_5^+ + CH_2 => CH_3^+ + CH_4$	9.6E-16			183
29	$CH_5^+ + CH => CH_2^+ + CH_4$	120E-16		-0.5	183
30	$CH_5^+ + C => CH^+ + CH_4$	12E-16			183
31	$CH_5^+ + H => CH_4^+ + H_2$	1.5E-16			183
32	$CH_3^+ + CH_4 => C_2H_5^+ + H_2$	9.6E-16			186
33	$CH_3^+ + CH_2 => C_2H_3^+ + H_2$	9.9E-16			183
34	$CH_3^+ + CH => C_2H_2^+ + H_2$	123E-16		-0.5	183
35	$CH_3^+ + C => C_2H^+ + H_2$	12E-16			183
36	$CH_3^+ + H => CH_2^+ + H_2$	7E-16	87800		183
37	$CH_2^+ + CH_4 => C_2H_5^+ + H$	2.88E-16			187
38	$CH_2^+ + CH_4 => C_2H_4^+ + H_2$	5E-16			187
39	$CH_2^+ + CH_4 => C_2H_3^+ + H_2 + H$	2.64E-16			187
40	$CH_2^+ + CH_4 => C_2H_2^+ + 2H_2$	1.44E-16			187
41	$CH_2^+ + C => C_2H^+ + H$	12E-16			183
42	$CH_2^+ + H_2 => CH_3^+ + H$	7.2E-16			186
43	$CH_2^+ + H => CH^+ + H_2$	10E-16	58866		183
44	$CH^+ + CH_4 => C_2H_4^+ + H$	0.77E-16			187
45	$CH^+ + CH_4 => C_2H_3^+ + H_2$	10.57E-16			187
46	$CH^+ + CH_4 => C_2H_2^+ + H_2 + H$	1.55E-16			187
47	$CH^+ + CH_2 => C_2H^+ + H_2$	10E-16			183
48	$CH^+ + CH => C_2^+ + H_2$	128E-16		-0.5	183

49	CH^++C=>C_2++H	12E-16			183
50	CH^++H_2=>CH_2^++H	10.1E-16			187
51	CH^++H=>C^++H_2	74.75E-16	241	-0.37	183
52	C^++CH_4=>$C_2H_3^+$+H	10.3E-16			183
53	C^++CH_4=>$C_2H_2^+$+H_2	4.2E-16			187
54	C^++CH_3=>$C_2H_2^+$+H	13E-16			183
55	C^++CH_3=> C_2H^++H_2	10E-16			183
56	C^++CH_2=> C_2H^++H	5.2E-16			183
57	C^++CH_2=>CH_2^++C	5.2E-16			183
58	C^++CH=>C_2^++H	65.8E-16		-0.5	183
59	C^++CH=>CH^++C	65.8E-16		-0.5	183
60	C^++H2=>CH^++H	1E-16	38579		183
61	H_3^++CH_4=>CH_5^++H_2	10.3E-16			183
62	H_3^++CH_4=>CH_3^++2H_2	10.3E-16			183
63	H_3^++CH_3=>CH_4^++H_2	21E-16			183
64	H_3^++CH_2=>CH_3^++H_2	17E-16			183
65	H_3^++CH=>CH_2^++H_2	207E-16		-0.5	183
66	H_3^++C=>CH^++H	20E-16			183
67	H_2^++CH_4=>CH_4^++H_2	14E-16			183
68	H_2^++CH_4=>CH_5^++H	1.1E-16			183
69	H_2^++CH_4=>CH_3^++H_2+H	22.8E-16			183
70	H_2^++CH_2=>CH_2^++H_2	10E-16			183
71	H_2^++CH_2=>CH_3^++H	10E-16			183
72	H_2^++CH=>CH^++CH_2	123E-16		-0.5	183
73	H_2^++CH=>CH_2^++H	123E-16		-0.5	183
74	H_2^++C=>CH^++H	24E-16			183
75	H_2^++H_2=>H_3^++H	21E-16			183
76	H_2^++H=>H^++H_2	6.4E-16			183
77	H^++CH_4=>CH_4^++H	15.2E-16			183
78	H^++CH_4=>CH_3^++H_2	22.8E-16			183
79	H^++CH_3=>CH_3^++H	34E-16			183
80	H^++CH_2=>CH_2^++H	14E-16			183
81	H^++CH_2=>CH^++H_2	14E-16			183
82	H^++CH=>CH^++H	329E-16		-0.5	183
83	$C_2H_4^+$+H=>$C_2H_3^+$+H2	3E-16			183
84	CH_4 + C_2H_3=>C_2H_4+CH_3	2.41E-30	22860	4.02	184
85	CH_4+C_2H =>C_2H_2+CH_3	0.03E-16	2079	0	184
86	CH_3+C_2H_6=>C_2H_5+CH_4	0.9E-30	34670	4	184
87	CH_3+C_2H_5=>C_3H_8	8.11E-16		-0.5	184
88	CH_3+C_2H_5=>C_2H_4+CH_4	0.019E-16			184
89	CH_3+C_2H_3=>C_2H_2+CH_4	8833E-16	2494	-1.5	183
90	CH_2+C_2H_3=>C_2H_2+CH_3	0.3E-16			182
91	CH_2+C_2H =>C_2H_2+CH	0.3E-16			182
92	CH+C_2H_6=>C_2H_4+CH_3	4.8E-16	242.7	-0.52	183
93	H_2+C_2H =>C_2H_2+H	3.9203e-25	1081	2.57	183
94	H+C_2H_5=>+C_2H_6	0.6E-16			185
95	H+C_2H_5=>CH_3+CH_3	0.6E-16			162
96	H+C_2H_5=>C_2H_4+H_2	0.03E-16			162
97	H+C_2H_4=>C_2H_5	0.14E-20	4150	1.49	184
98	H+C_2H_4=>C_2H_3+H_2	2.2E-24	51220	2.53	183
99	H+C_2H_3=>C_2H_2+H_2	0.332E-16			183

100	$H+C_2H_2 \Rightarrow C_2H+H_2$	3.8E-16	113359		183
101	$C_2H_6+C_2H \Rightarrow C_2H_5+C_2H_2$	0.067E-16	-515	0.28	182
102	$C_2H_5+C_2H_5 \Rightarrow C_2H_6+C_2H_4$	0.024E-16			184
103	$C_2H_5+C_2H_5 \Rightarrow C_4H_{10}$	0.19E-16			184
104	$C_2H_5+C_2H \Rightarrow C_2H_4+C_2H_2$	0.03E-16			184
105	$CH_4^+ + C_2H_6 \Rightarrow C_2H_4^+ + CH_4 + H_2$	19.1E-16			186
106	$CH_4^+ + C_2H_4 \Rightarrow C_2H_4^+ + CH_4$	13.8E-16			183
107	$CH_4^+ + C_2H_4 \Rightarrow C_2H_5^+ + CH_3$	4.23E-16			183
108	$CH_4^+ + C_2H_2 \Rightarrow C_2H_2^+ + CH_4$	11.3E-16			183
109	$CH_4^+ + C_2H_2 \Rightarrow C_2H_3^+ + CH_3$	12.3E-16			183
110	$CH_5^+ + C_2H_4 \Rightarrow C_2H_5^+ + CH_4$	15E-16			183
111	$CH_5^+ + C_2H_2 \Rightarrow C_2H_3^+ + CH_4$	16E-16			183
112	$CH_5^+ + C_2H \Rightarrow C_2H_2^+ + CH_4$	9E-16			183
113	$CH_5^+ + C2 \Rightarrow C_2H^+ + CH_4$	9.5E-16			183
114	$CH_3^+ + C_2H_6 \Rightarrow C_2H_5^+ + CH_4$	14.8E-16			183
115	$CH_3^+ + C_2H_4 \Rightarrow C_2H_3^+ + CH_4$	3.5E-16			183
116	$CH_3^+ + C_2H_3 \Rightarrow C_2H_3^+ + CH_3$	51.9E-16		-0.5	183
117	$C^+ + C_2H_6 \Rightarrow C_2H_5^+ + CH$	2.31E-16			183
118	$C^+ + C_2H_6 \Rightarrow C_2H_4^+ + CH_2$	1.16E-16			183
119	$C^+ + C_2H_6 \Rightarrow C_2H_3^+ + CH_3$	4.95E-16			183
120	$C^+ + C_2H_6 \Rightarrow C_2H_2^+ + CH_4$	0.825E-16			183
121	$C^+ + C_2H_5 \Rightarrow C_2H_5^+ + C$	5E-16			183
122	$C^+ + C_2H_4 \Rightarrow C_2H_4^+ + C$	0.17E-16			183
123	$C^+ + C_2H_4 \Rightarrow C_2H_3^+ + CH$	0.85E-16			183
124	$H_3^+ + C_2H_6 \Rightarrow C_2H_5^+ + 2H_2$	34E-16			186
125	$H_3^+ + C_2H_5 \Rightarrow C_2H_6^+ + H_2$	14E-16			183
126	$H_3^+ + C_2H_4 \Rightarrow C_2H_5^+ + H_2$	14.4E-16			183
127	$H_3^+ + C_2H_4 \Rightarrow C_2H_3^+ + 2H_2$	21.6E-16			183
128	$H_3^+ + C_2H_3 \Rightarrow C_2H_4^+ + H_2$	346E-16		-0.5	183
129	$H_3^+ + C_2H_2 \Rightarrow C_2H_3^+ + H_2$	35E-16			183
130	$H_3^+ + C_2H \Rightarrow C_2H_2^+ + H_2$	17E-16			183
131	$H_3^+ + C_2 \Rightarrow C_2H^+ + H_2$	18E-16			183
132	$H_2^+ + C_2H_6 \Rightarrow C_2H_6^+ + H_2$	2.94E-16			183
133	$H_2^+ + C_2H_6 \Rightarrow C_2H_5^+ + H_2 + H$	13.7E-16			183
134	$H_2^+ + C_2H_6 \Rightarrow C_2H_4^+ + 2H_2$	23.5E-16			183
135	$H_2^+ + C_2H_6 \Rightarrow C_2H_3^+ + 2H_2 + H$	6.86E-16			182
136	$H_2^+ + C_2H_6 \Rightarrow C_2H_2^+ + 3H_2$	1.96E-16			182
137	$H_2^+ + C_2H_4 \Rightarrow C_2H_4^+ + H_2$	22.1E-16			183
138	$H_2^+ + C_2H_4 \Rightarrow C_2H_3^+ + H_2 + H$	18.1E-16			183
139	$H_2^+ + C_2H_4 \Rightarrow C_2H_2^+ + 2H_2$	8.8E-16			183
140	$H_2^+ + C_2H_2 \Rightarrow C_2H_2^+ + H_2$	48.2E-16			183
141	$H_2^+ + C_2H_2 \Rightarrow C_2H_3^+ + H$	4.8E-16			183
142	$H_2^+ + C_2H \Rightarrow C_2H^+ + H_2$	10E-16			183
143	$H_2^+ + C_2H \Rightarrow C_2H_2^+ + H$	10E-16			183
144	$H_2^+ + C_2 \Rightarrow C_2^+ + H_2$	11E-16			183
145	$H_2^+ + C_2 \Rightarrow C_2H^+ + H$	11E-16			183
146	$H^+ + C_2H_6 \Rightarrow C_2H_4^+ + H_2 + H$	14E-16			183
147	$H^+ + C_2H_6 \Rightarrow C_2H_3^+ + 2H_2$	28E-16			183
148	$H^+ + C_2H_5 \Rightarrow C_2H_4^+ + H_2$	16.5E-16			183
149	$H^+ + C_2H_5 \Rightarrow C_2H_3^+ + H_2 + H$	30.6E-16			183
150	$H^+ + C_2H_4 \Rightarrow C_2H_3^+ + H_2$	30E-16			183

151	$H^+ + C_2H_4 => C_2H_2^+ + H_2 + H$	10E-16			183
152	$H^+ + C_2H_4 => C_2H_4^+ + H$	10E-16			183
153	$H^+ + C_2H_3 => C_2H_3^+ + H$	346E-16		-0.5	183
154	$H^+ + C_2H_3 => C_2H_2^+ + H_2$	346E-16		-0.5	183
155	$H^+ + C_2H_2 => C_2H_2^+ + H$	5.4E-16			183
156	$H^+ + C_2H => C_2H^+ + H$	15E-16			183
157	$H^+ + C_2H => C_2^+ + H_2$	15E-16			183
158	$H^+ + C_2 => C_2^+ + H$	31E-16			183
159	$C_2H_5^+ + H => C_2H_4^+ + H_2$	0.1E-16			183
160	$C_2H_4^+ + C_2H_3 => C_2H_5^+ + C_2H_2$	86.6E-16		-0.5	183
161	$C_2H_4^+ + C_2H_3 => C_2H_3^+ + C_2H_4$	86.6E-16		-0.5	183
162	$C_2H_3^+ + C_2H_6 => C_2H_5^+ + C_2H_4$	2.91E-16			183
163	$C_2H_3^+ + C_2H_4 => C_2H_5^+ + C_2H_2$	9.3E-16			186
164	$C_2H_3^+ + C_2H_3 => C_2H_5^+ + C_2H$	86.6E-16		-0.5	183
165	$C_2H_3^+ + C_2H => C_2H_2^+ + C_2H_2$	86.6E-16		-0.5	183
166	$C_2H_3^+ + H => C_2H_2^+ + H_2$	0.68E-16			183
167	$C_2H_2^+ + C_2H_6 => C_2H_4^+ + C_2H_4$	2.62E-16			183
168	$C_2H_2^+ + C_2H_6 => C_2H_5^+ + C_2H_3$	1.31E-16			187
169	$C_2H_2^+ + C_2H_4 => C_2H_4^+ + C_2H_2$	4.0E-16			183
170	$C_2H_2^+ + C_2H_3 => C_2H_3^+ + C_2H_2$	57E-16		-0.5	183
171	$C_2H_2^+ + H_2 => C_2H_3^+ + H$	10E-16			183
172	$C_2H^+ + CH_4 => C_2H_2^+ + CH3$	3.74E-16			183
173	$C_2H^+ + CH_2 => CH_3^+ + C2$	4.4E-16			183
174	$C_2H^+ + H_2 => C_2H_2^+ + H$	7.8E-16			186
175	$C_2^+ + CH => CH^+ + C_2$	55.4E-16		-0.5	183
176	$C_2^+ + CH_4 => C_2H_2^+ + CH_2$	1.82E-16			183
177	$C_2^+ + CH_4 => C_2H^+ + CH_3$	2.38E-16			183
178	$C_2^+ + CH_2 => CH_2 + + C_2$	4.5E-16			183
179	$C_2^+ + C => C^+ + C_2$	1.1E-16			183
180	$C_2^+ + H_2 => C_2H^+ + H$	11E-16			183
181	$C_2H_6^+ + C_2H_6 => C_3H_8^+ + CH_4$	0.08E-16			182
182	$C_2H_6^+ + C_2H_4 => C_2H_4^+ + C_2H_6$	11.5E-16			183
183	$C_2H_6^+ + C_2H_2 => C_2H_5^+ + C_2H_3$	2.22E-16			188
184	$C_2H_6^+ + H => C_2H_5^+ + H_2$	1E-16			183

Table IV-2: Wall reactions with Sticking coefficient, see ref [185]
(for ions we assume that the sticking coefficient is 1).

N	Wall reaction	Sticking coefficient
01	CH_2	0.026
02	CH_3	0.001
03	CH_4	0.01
04	C_2H	0.8
05	C_2H_3	0.3
06	C_2H_5	0.01
07	H	0.07
08	C	1
09	C_2	1

IV.5. Results and discussion

The modeling is performed for a pure CH_4 discharge. The neutral gas distribution is assumed uniform during the simulations, and the gas temperature is set to 300 K. The gap between two electrodes is set to d= 6 cm.

The aim of this study is the calculation of the different species densities in methane plasma, and known the most existing species. Other information can be obtained such as the electric field, and plasma potential. The results shown in this section are the electrons density, neutrals and ions densities as a function of the gap distance. In this study we concentrate on the densities of species for the determination of the dominate elements in the methane plasma using the fluide model which is based on the moments of the Boltzmann equation [188-192].

Figure IV-4 shows the electron density, we can see that the density in the bulk plasma stay nearly stable, but at the sheath changes strongly for the four phases (0T, 0.25T, 0.5T, 0.75T) of RF cycle, it shows that the electrons can almost instantaneously follow the variations of the electric field because of their low inertia. At the beginning of the radiofrequency cycle, the electrons are attracted to the left electrode (anode) giving a negative space charge which decreases the electric field in the vicinity of this electrode and which causes the contraction of the sheath. Then during the evolution of the RF cycle, the electrons are pushed back to the plasma region (in the center of the discharge) which leads to a positive space charge in the sheath. This appearance of the positive charge in the vicinity of the electrode (cathode) leads to the increase of the electric field at this location causing the expansion of this sheath. Therefore, the motion of the electrons by covering and uncovering the positive space charge in the ducts is the basis of the formation and oscillation of the ducts. The contraction and expansion of the sheaths are themselves the basis of the movement of the electrons. This is indeed a mutual effect that strongly couples the transport of electrons and the variation of the electric field.

Figure IV.5 shows the spatiotemporal variation of the potential in the discharge during the RF cycle. In the plasma region in the center of the discharge, the potential is always greater than that of the electrodes which constitutes an effective barrier to maintain the stability and neutrality of the plasma. In fact, this average value is close to half of the applied peak voltage

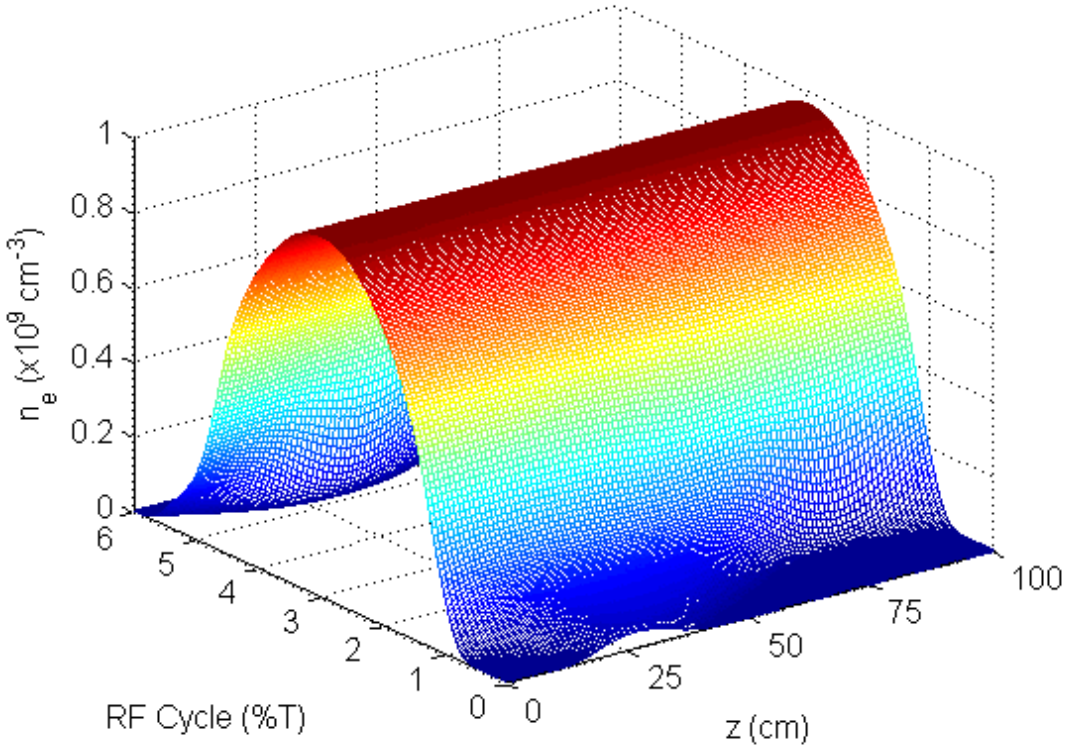

Fig. IV-4: Spatiotemporal variation of electrons density

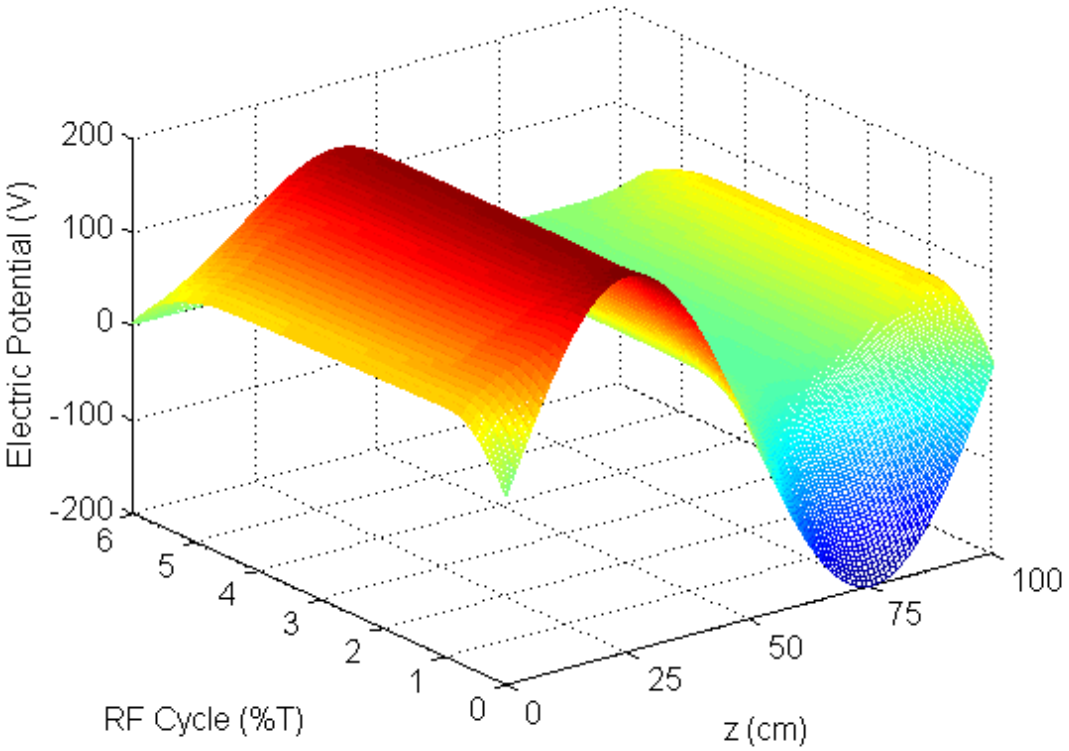

Fig. IV-5: Spatiotemporal variation of plasma potential

because the self-bias voltage is zero in the case of a symmetrical discharge which is studied in this section.

Figure IV.6 shows the spatio-temporal variation of the electronic temperature T_e, is more or less constant throughout the bulk plasma, except near the electrodes. The rapid change in the electronic temperature near the electrodes is due to the frequent collisions between the electrons and neutrals that hinder the energetic electrons from moving the electrode gap distance. This temperature is important in the sheaths particularly at the moments when the radiofrequency voltage passes by its extremes.

Figure IV.7 shows the spatio-temporal variation of the electric field as a function of the position and the different instants of the cycle of the applied radio frequency voltage. The field is very weak in the plasma because of the electrical neutrality whereas it is important in the sheaths for the reasons already mentioned concerning the oscillatory movement of the electrons compared to those of the ions.

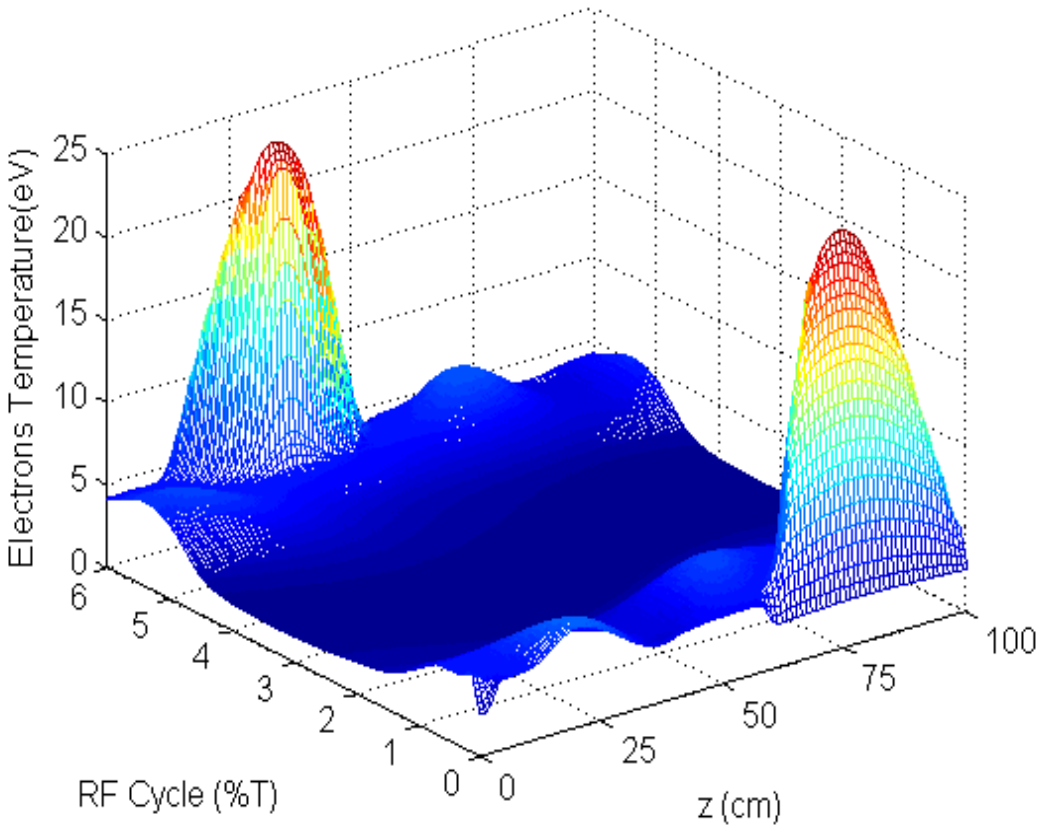

Fig. IV-6: Spatiotemporal variation of electrons Temperature

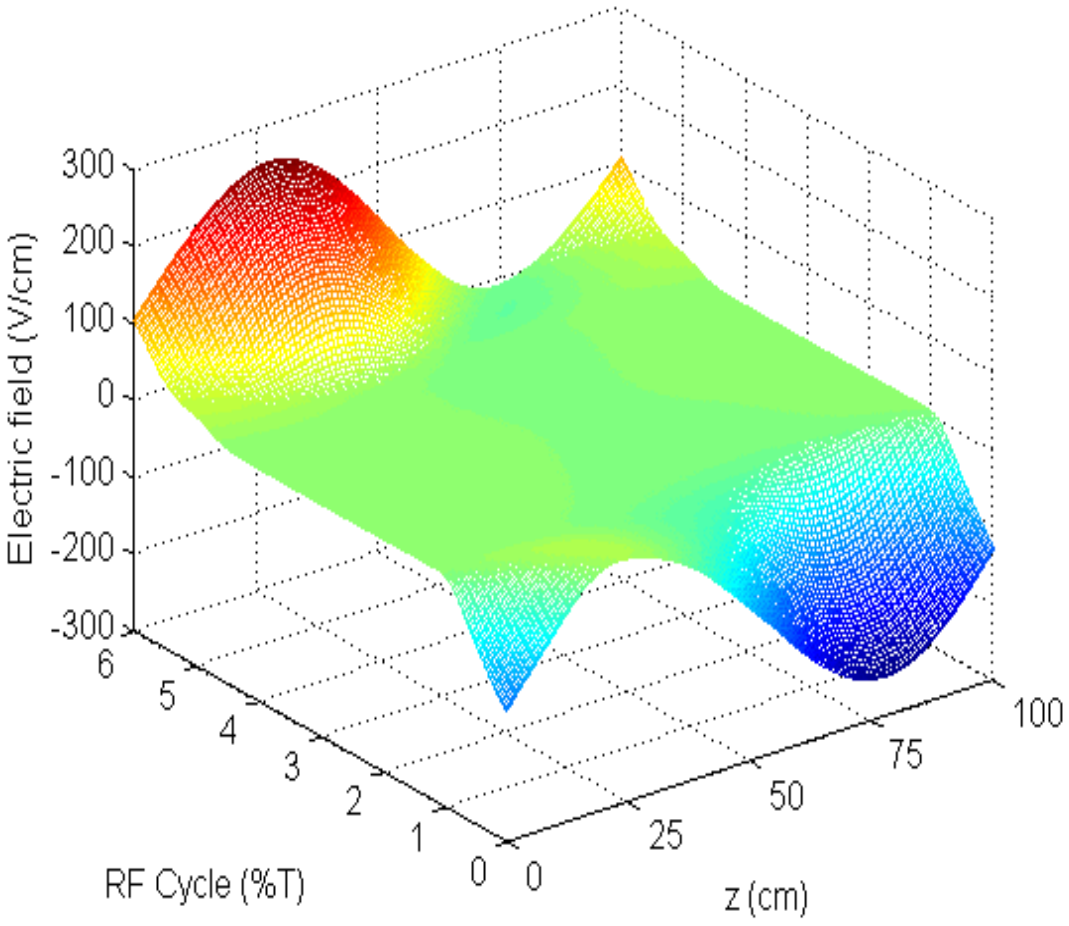

Fig. IV-7: Spatiotemporal variation of Electric field

At the electrodes, the electric field, which is by definition the gradient of the potential, logically follows a sinusoidal variation of the same frequency as the radiofrequency voltage applied. We recall that the radiofrequency voltage Vrf (t) is applied to the left electrode (z = 0 cm) while the right electrode is grounded (z = 6 cm).

Figure IV-8 shows the neutrals densities as a function of the position; we see that the H atoms are largely produced, because of Hydrogen atom H is produced by electron impact collision (see in table III-1 reactions 1, 3, 6 and 8). The Hydrogen molecule H_2 is also produced a lot (see in table III-1, reactions 2, 3, 4, 7, 8, and 9).

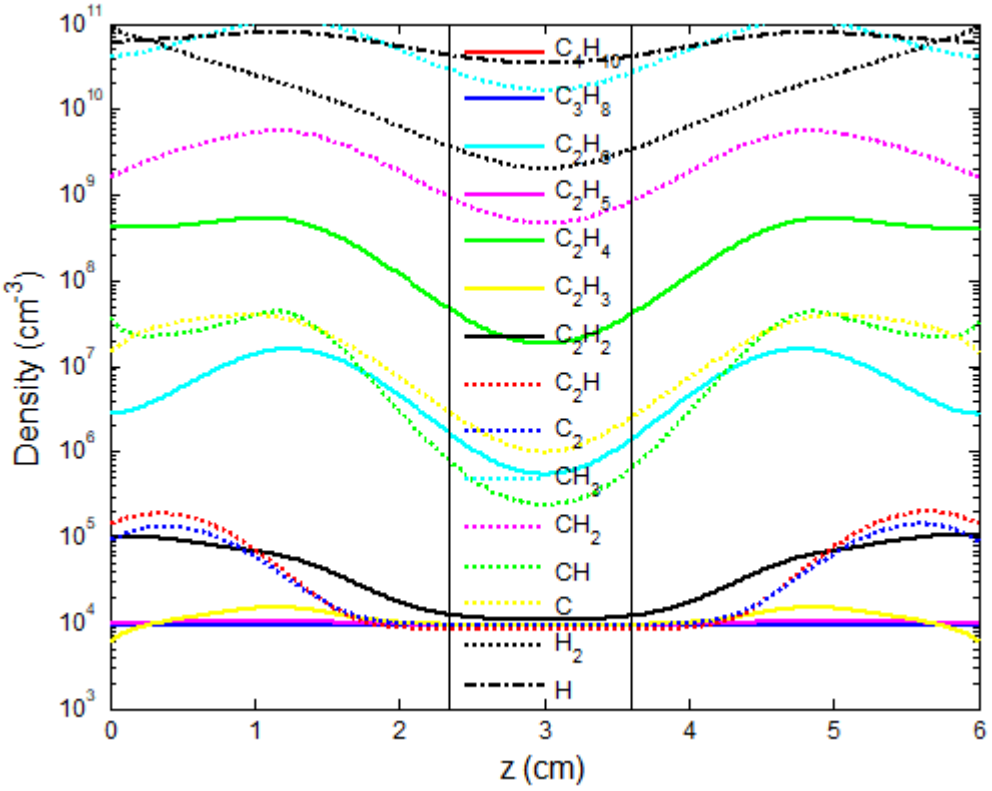

Fig. IV-8: Neutral species densities

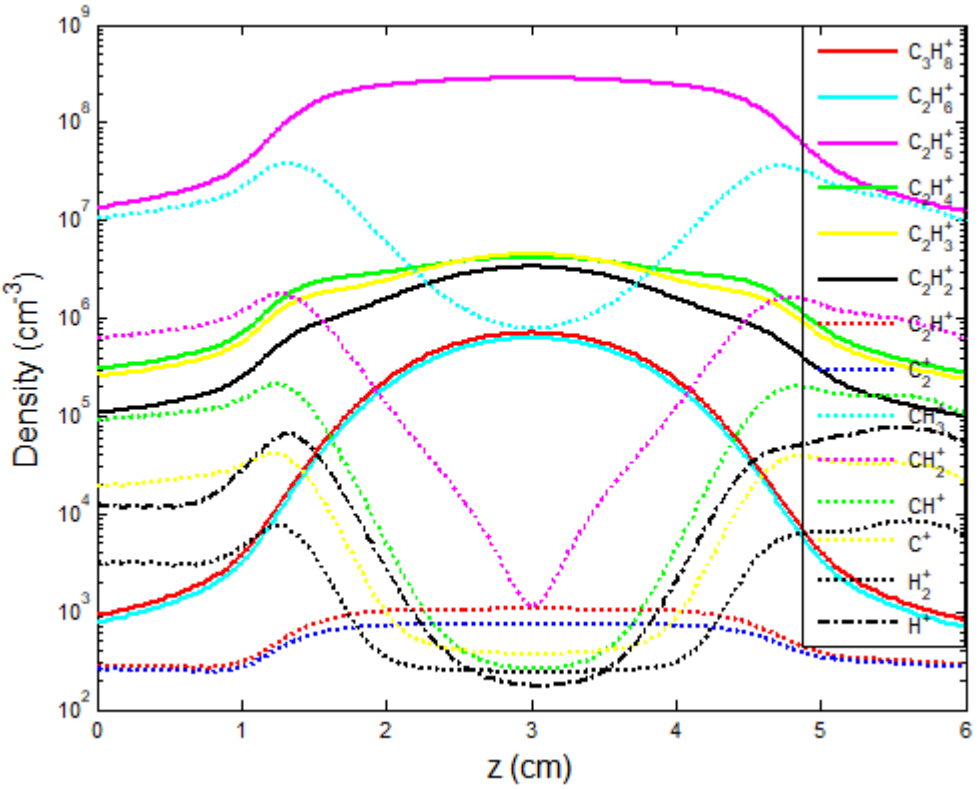

Fig. IV-9: Ions species densities

We can see that H_2 is most abundant than CH_3 and H at the sheaths, because of the H_2 is mainly formed through the wall reactions, CH_2 comes in fourth position, and this due to the reactions 5, and 13 (table III-1). The C_2H_4 molecules are essentially produced by the reaction $CH_3+CH_2=>C_2H_4+H$, $CH_2+CH_2=>C_2H_4$, CH4+CH=>C_2H_4+H.

The densities of others molecules are little than 0.1% of H density. We note that C_2H_6 molecule is produced by the reaction $CH_3+C_2H_5$ by $CH_3+C_2H_6=>C_2H_5+CH_4$, C_3H_8 by $CH_3+C_2H_5$, C_4H_{10} by $C_2H_5+C_2H_5$.

The observed ions species densities (figure IV-9) gives CH_5^+ and $C_2H_5^+$ followed by CH_4^+ and CH_3^+ as the most abundant ions, which is in agreement with the study of A.Rhallabi and Y.Cathrine [83]. $C_2H_5^+$ ions are produced essentially by the reaction $CH_3^+ + CH_4 => C_2H_5^+ + H_2$, and CH_5^+ ions are produced essentially by the reaction $CH_4^+ + CH_4 => CH_5^+ + CH_3$, these two latter equations caused the diminution in CH_4^+ ions density and CH3+ions density at the discharge center. The same behavior for CH+ and CH_2^+; decreasing in the center and contribute to the formation of $C_2H_5^+$, $C_2H_4^+$, C_2H_3+, and C2H2+through the following reactions:

$CH_2^+ + CH_4 => C_2H_5^+ + H$

$CH_2^+ + CH_4 => C_2H_4 + H_2$

$CH_2^+ + CH_4 => C_2H_3^+ + H_2 + H$

$CH_2^+ + CH_4 => C_2H_2^+ + 2\,H_2$

$CH^+ + CH_4 => C_2H_4^+ + H$

$CH^+ + CH_4 => C_2H_3^+ + H_2$

$CH^+ + CH_4 => C_2H_2^+ + H_2 + H$

The charged species H_2^+, H^+ and C^+ are produced by collision of electron CH_4 with large quantities, but the destruction rate by ions-molecule reactions is large, in fact their number densities in the plasma is very small.

IV.6. Conclusion

The study achieved out during this work concerns the numerical modeling of capacitively coupled cold electric discharge plasma. The adopted model considers the plasma as a continuous fluid medium. In this model, the ions are described by the first two moments of Boltzmann equation, the electrons are described by the first three moments of Boltzmann equation, and all of these equations are coupled with Poisson equation. The work carried out has highlighted a number of phenomena taking place in the methane plasma especially the densities of existing species. The most abundant neutrals species in the methane plasma are CH3, H, H_2, CH_2 and C_2H_4, and the most abundant for ions are: CH_5^+, $C_2H_5^+$, CH_4^+, and CH_3^+. These results are in agreement with the results of Tachibana et al. [86] and Chien-Wei Chang [85] for the neutral species and with A. Rhallabi and Y. Catherine [83] for the charged species. The small differences found in orders of magnitude resulting of differs choice of the boundary conditions and transport parameters (mobility coefficient, diffusion, ionization, etc.). These need further study to correlate more adequately with the different physical parameters of the discharge such as gas pressure, applied voltage, and secondary emission coefficient. The small differences found in orders of magnitude are resulting of the different selection of the boundary conditions and transport parameters (mobility coefficient, diffusion, ionization coefficient, etc.). These need further study to correlate more adequately with the different physical parameters of the discharge such as gas pressure, applied voltage, and secondary emission coefficient.

CHAPTER V

MODELING OF INDUCTIVELY COUPLED PLASMA IN METHANE

V.1. Introduction

As we saw in the previous chapter that the dissociation of the methane is very weak and consequently the production of the hydrogen is very weak too. Inductively coupled plasmas are one of the most used alternatives to solve the problems of the plasma density limit, where a very low discharge can be generated by generating a low power.

In an Inductively Coupled Plasma (ICP), the radiofrequency (RF) currents in the coil (inductive element) generate an rf magnetic flux, which penetrates the plasma region. The time-varying magnetic flux density induces a solenoidal RF electric field, which accelerates the free electrons and sustains the discharge [191-192].

Due to the high density and low operating pressure; inductively coupled plasma (ICP) sources are particularly used for applications that depend on high electron density such as etching and deposition, etc. [193-200].Another typical advantage that leads to a growing interest for this type of discharge is the low energy of the ions that leave the discharge. For sensitive applications, such as diamond deposition, automatic polarization voltage and therefore ionic energy should not exceed a certain level to ensure optimal growth conditions[201]. For these reasons ICP is extensively studied experimentally as [202-204] and analytically by modeling and simulation as [205-207].

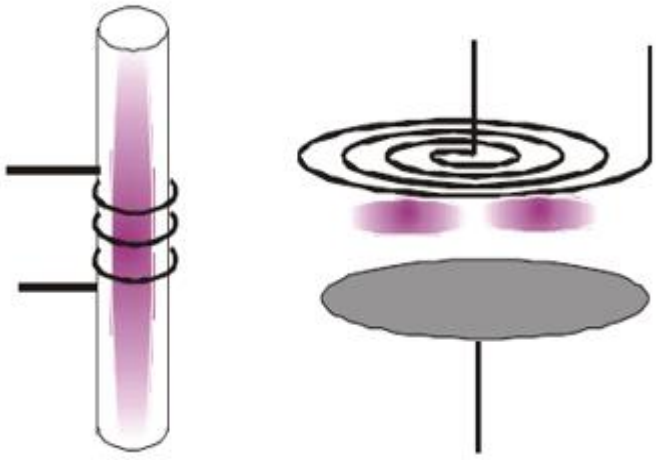

Fig. V-1: principal schema of ICP reactors

In this study we are interested in the 2D modeling of low pressure plasma methane radiofrequency for the ICP GEC configuration.

V.2. Overview about the inductively coupled plasma

A self-consistent two-dimensional radio frequency inductively coupled glow discharge model has been developed in cylindrical coordinates using a fluid model by K. Bera et al [208].

Emre Turkoz and Murat Celik [209] developed a numerical model for the inductively coupled plasma in radio frequency (RF) ion thruster discharge chamber to evaluate the plasma parameters for a 2-D axisymetric domain.

Yu-Ru Zhang et al [210] employed Multiphysics Analysis for Plasma Sources-ICP (MAPS-ICP) solver accompanied with the MAPS-sheath module, to investigate the bias effect on the discharge mode transition and plasma characteristics in an ICP reactor at various ICP currents, bias voltages, and bias frequencies.

L Lallement et al [211] developed a global model for low-pressure (3–20 mTorr), radio-frequency (13.56 MHz) inductively coupled plasmas (ICPs), produced in SF_6/Ar mixtures. The model is based on a set of mass balance equations for all the species considered, coupled to the discharge power balance equation and the charge neutrality condition.

Vernon H. Chaplin and Paul M. Bellan [212] describe a two-fluid model for a high density ($ne > 10^{19}$ m^{-3}) pulsed argon ICP in a high aspect ratio cylindrical discharge tube.

In the experiment and numerical study of C S Corr et al [213] the neutral and charged particle dynamics in both the capacitive and inductive modes of an inductively coupled oxygen discharge are presented. Langmuir probes, laser-assisted photo detachment and two-photon laser-induced fluorescence are employed to measure plasma parameters in the 13.56MHz system for a range of plasma powers and gas pressures.

In this study, modeling is done for more than 300 reactions; a set of 83 electronic impact collision with CH_4, CH_3, CH_2, CH, C, H, H_2, C_2H_2, C_2H_4, C_2H_6, and the neutral-neutral and ion-neutral reactions, we consider also the wall reactions. As well as two modules are combined; laminar flow and ICP for a good description of the phenomena existing in this type of plasma.

V.3. Inductively Coupled Plasma Reactors

Inductively coupled plasmas are one of the most used alternatives to solve the problems of the plasma density limit, where a very low discharge can be generated by generating a low power. The plane configuration also known as TCP (coupled plasma transformation) seems more attractive because it can process silicon wafers of larger surface at low pressure while maintaining the homogeneity of the plasma in front of the substrate (see Figure V-2). On the other hand, the cylindrical configuration can be easily used to carry out a surface treatment or deposition by the low pressure PECVD technique (from 7.5 to 75 mTorr) on small diameter planar samples placed in downstream (see Figure V-3). For these configurations, the plasma is created by the action of the RF magnetic field. The inductive coupling ensures a high rate of ionization at very low pressure (≈4mTorr). The substrate can be placed in a separate chamber below the source. In practice, the substrate holder is powered by a radiofrequency (RF) or continuous (DC) source independent of the power source, in order to independently control the sheath voltage.

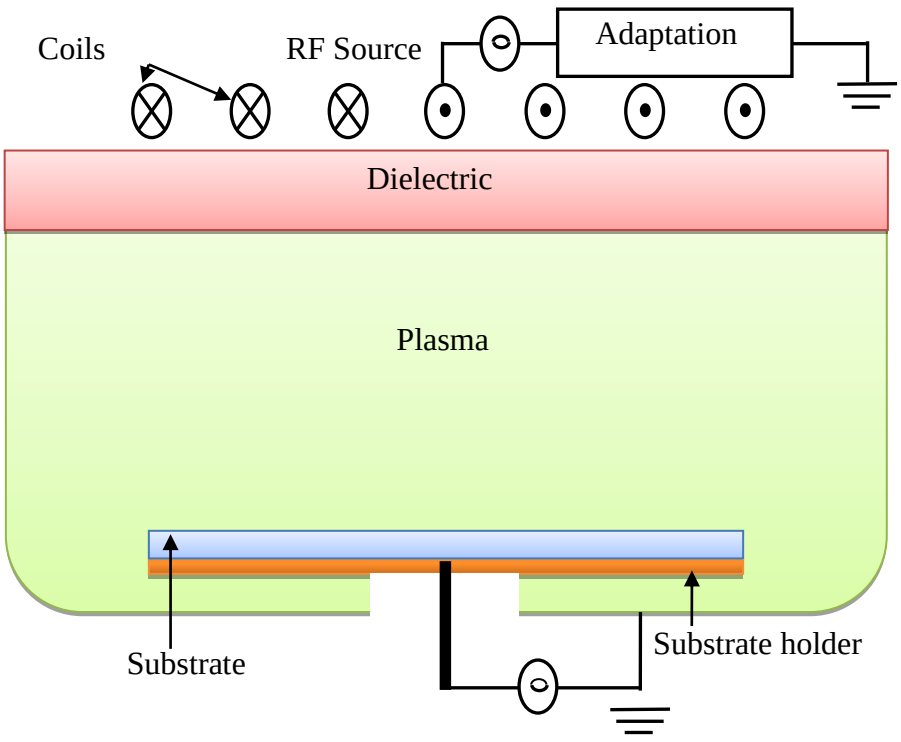

Fig. V-2: Schematic of a ICP type inductive reactor with planar configuration

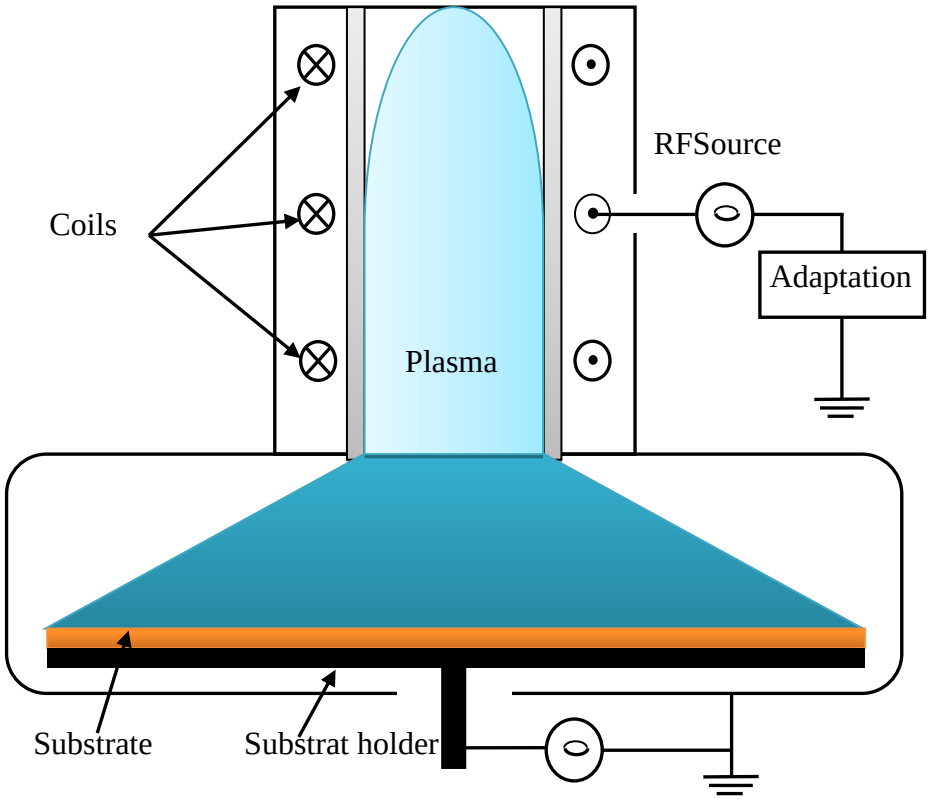

Fig. V-3: Schematic of a ICP type inductive reactor with planar configuration

V.3.1. Operating principle

A simple ICP reactor is a cylindrical chamber of radius R and height h in which the gases are injected. These sources are maintained at low pressure (between 5 and 50 mTorr) by external alternating electric fields, the frequency range is typically between 1 and 100 MHz. In these systems, an antenna separated from the plasma by a dielectric wall and connected to a high frequency power supply (generally at 13.56 MHz). The RF current flowing in the antenna generates a variable magnetic field B in the enclosure in the form of lines induced in loops, a matching circuit is used to reduce the impedance of the coil and maximize the coupling thereof with the plasma. In order to limit the capacitive coupling, a dielectric window is placed between the plasma and the coil. The gases are evacuated by a pumping system, usually a primary pump associated with a turbo-molecular pump. The current injected into the coil creates a radiofrequency magnetic field (see Figure V-4) which in turn induces a toroidal electric field in a small region called "skin thickness" and located just below the dielectric window (it is mentioned by δ in Figure V-4). In this zone, the electrons are accelerated by the electric field and collide with the neutrons, creating ions and dissociating the molecules in the case of a molecular gas such as H_2, O_2, N_2, CH_4, etc.

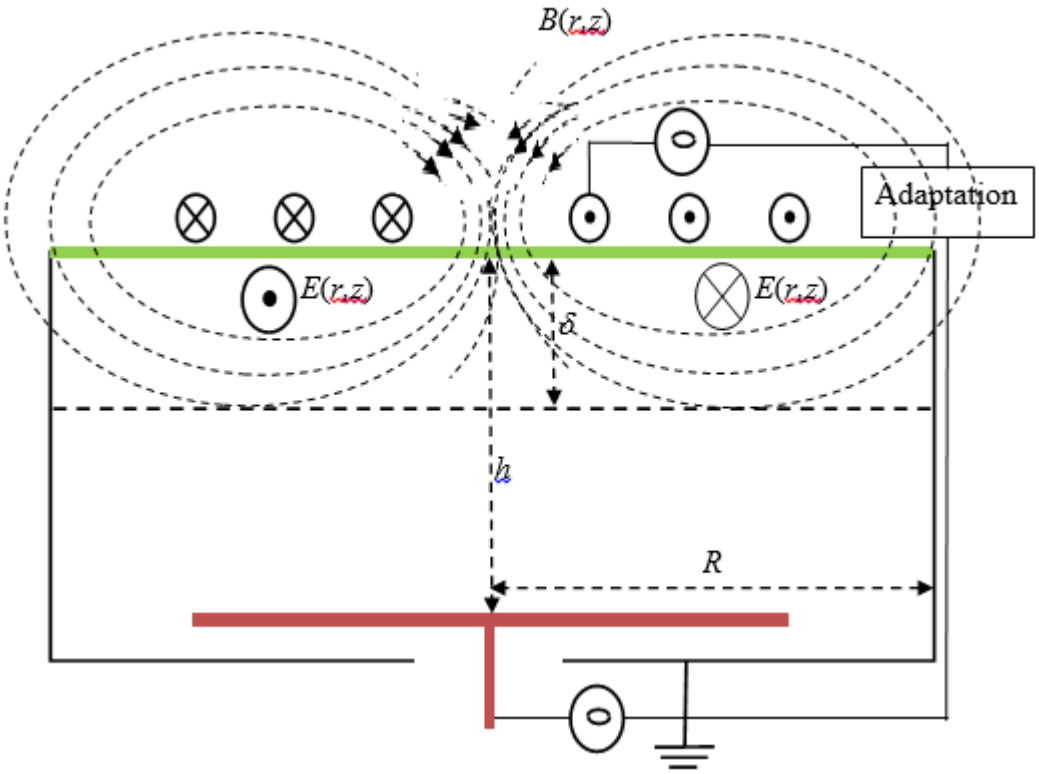

Figure V-4: Electromagnetic field lines in a planar reactor

The variable magnetic field induces an electric field E (according to the Faraday law), and consequently a current density *J* azimuthal in the plasma through a dielectric window ($J=\sigma E$), this field *E* makes it possible to accelerate the electrons and thus transmits the energy necessary for the maintenance of the discharge. The determination of the electric field coupled to the magnetic field can be obtained by solving the Maxwell equations. However, ohmic heating is not the only possible process in inductively coupled reactors because it is possible to create and maintain a non-colliding plasma at very low pressure [214]. At very low pressure, the average free path of the electrons is of the order of magnitude of the skin thickness. When an electron enters this region of skin, close to the dielectric window, it will be accelerated under the effect of the electric field towards the heart of the plasma, and then it will be returned, but with a higher energy than it had before entering the skin thickness. The inductive regime actually only operates at sufficiently high powers. To initiate the plasma at low power, the capacitive regime is essential [215]. In the latter regime, the coil acts as a conventional electrode and generates the plasma in the same way as a capacitive reactor. As the power increases, a transition between capacitive and inductive mode occurs, giving rise to instabilities. Although it is necessary to start the plasma, the capacitive regime can cause the

appearance of a too large electric field to the walls of the reactors. The role of the dielectric windows is to reduce this capacitive effect. The plasma created within the skin thickness then diffuses into the reactor. The lower the pressure, the more active charged species will be able to spread far. A substrate holder is generally disposed at the bottom of the reactor. A radiofrequency source can be used to energize the substrate holder to modify the electric field of the sheath close thereto, and in this way it is possible to independently control the density of the plasma, the flow of ions to the sheaths. and the energy of ion bombardment.

An inductively coupled plasma (ICP) can be generated by directing the energy of an RF generator (typically 13.56 MHz) to the gas used [216]. The principle of eddy current heating is well known in the heating of metals, and it applies in the same way to ionized gases. A cooled induction coil generates a variable magnetic flux over time and cuts a conductor (in our case is the plasma), it can cause an electromotive force and an induced power. Fast electrons collide with atoms or gas molecules and produce additional ionization, resulting in a significant increase in temperature. Since the electrical conductivity of the plasma is relatively high, the oscillating electromagnetic field can not penetrate further into the plasma, especially at high frequencies. This phenomenon is quantified by introducing the notion of skin effect. In plasma as in a metal heated by electromagnetic induction, the induced currents, which flow in the opposite direction to the primary current of the inductor, they are in the outer shell of the conductor. The skin thickness δ which is a function of the frequency has the following expression:

$$\delta = -\frac{c}{\omega}.\frac{1}{\sqrt{\mathrm{Im}(\varepsilon_r)}} \qquad \text{(V-1)}$$

with c, ω, and $\mathrm{Im}(\varepsilon_r)$: are respectively, the speed of light, the pulsation of the source, and the imaginary part of the relative permittivity of the plasma ε_r, where it is expressed as follows:

$$\varepsilon_r = 1 - \frac{\omega_p^2}{\omega(\omega - j\nu_m)} \approx -\frac{\omega_p^2}{\omega^2(1 - j\nu_m/\omega)} \qquad \text{(V-2)}$$

where ω_p, and ν_m : are the plasma pulsation and the transfer collision frequency of the amount of motion respectively. According to the ratio ν_m/ω, the skin thickness can be expressed by the following relationships:

$$\delta_p = \sqrt{\frac{m_e}{e^2 n_e \mu_0}} \quad si \ \frac{\nu_m}{\omega} << 1$$
$$\delta_c = \delta_p \cdot \sqrt{\frac{2\nu_m}{\omega}} = \sqrt{\frac{2}{\mu_0 \sigma \omega}} \ si \ \frac{\nu_m}{\omega} >> 1 \qquad \text{(V-3)}$$

where μ_0 is the vacuum permeability and $\sigma = e^2 n_e / m_e \nu_m$ is the conductivity of the plasma. There is a third situation for which the electrons incident on a skin layer of thickness δ_e satisfy the following condition:

$$\frac{\upsilon_e}{2\delta_e} >> \omega, \nu_m \qquad \text{(V-4)}$$

with υ_e: is the electrons mean velocity, the interaction time of the electrons with the skin layer is short in comparison with the RF period or with the collision time. By analogy with collisionless heating on a capacitive sheath, the stochastic collision frequency ν_{stoc} can be defined as follows:

$$\nu_{stoc} = \frac{C_e \upsilon_e}{4\delta_e} \qquad \text{(V-5)}$$

where C_e is a quantity of order unity that depends weakly on υ_e, δ_e, and ω. Now we replace ν_m with ν_{stoc} in equation (V-2) taking into account the condition $\nu_{stoc} >> \omega$, we obtain:

$$\delta_e = \left(\frac{C_e \upsilon_e}{2\omega\delta_p} \right)^{\frac{1}{3}} \delta_p \qquad \text{(V-6)}$$

For typical low-pressure discharges, we are generally in the regime for which the order of frequencies $\omega \sim \upsilon_e / 2\delta \geq \nu_m$ such that the depth of the skin is approximately δ_p.

V.3.2. Operating regimes of inductively coupled plasmas

A real inductive discharge can operate in two different main regimes; these two regimes are separated by an intermediate regime:

The high power regime called the inductive regime (H): For larger powers, an induced azimuth electric field below the antenna which is responsible for the generation of the plasma. The energy absorbed by the electrons is important which leads to densities of charged particles much larger than those of capacitive discharges. The skin thickness then becomes small in front of the reactor dimensions $\delta << R,h$ (R, h: are respectively the radius and the

reactor height) and very large in front of the thickness of the sheath. The plasma is in a high density regime, the energy coupling is in inductive mode and characterized by a relatively low plasma potential [217]. In this regime of high density and for a given current I_{rf}, we see that the total power absorbed by the electrons of the plasma (inductive heating) decreases with the increase of the electron density:

$$P_{abs} \propto \frac{I_{rf}^2}{\sqrt{n_e}} \quad \text{(V-7)}$$

The low power regime called capacitive regime (E): At low power, the skin thickness is very large in front of the reactor dimensions $\delta >> R, h$ and very small in front of the size of the sheath. In this case the induced electromagnetic field is not significantly absorbed in the plasma, the inductive coupling is very inefficient and the heating mechanism is similar to the capacitively coupled discharges. Due to its origin from the electrostatic field E, this mode is called mode E. In the low electron density regime, the power absorbed is proportional to the density ne.

$$P_{abs} \propto I_{rf}^2 n_e \quad \text{(V-8)}$$

The intermediate regime (E-H) is the jump between the capacitive and inductive modes.

The figure V-5 shows these operating conditions in the case of an O_2/Ar mixture (90%/10%) under a total pressure of 10 mTorr. It clearly shows that at low radiofrequency power, the electron density is low, and then the plasma operates in capacitive regime (mode E), When increasing the power of the source, the coupling between the coil and the plasma is more efficient, and the discharge goes from the capacitive regime to the inductive high density mode (mode H). Generally, the predominance of one mode over the other depends on several parameters such as the RF power applied, the pressure in the reactor or the gas used [218,219].

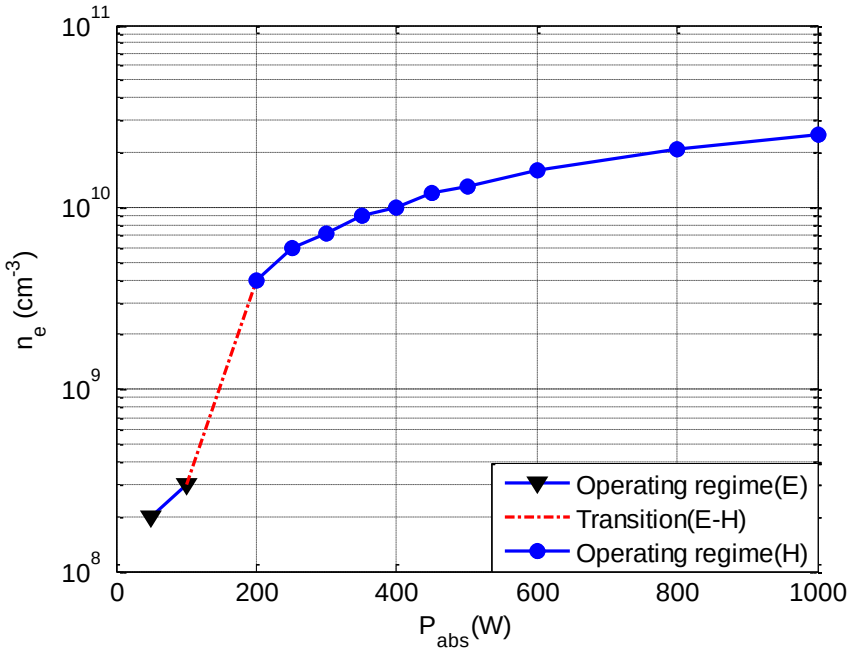

Fig. V-5: Evolution of the electronic density as a function of the power in an O_2 / Ar plasma (90% -10%) in an ICP reactor for a pressure of 10 mTorr [219,220].

V.3.3. Equivalent electrical circuits

Each element of the equivalent circuit depends on the characteristic of the discharge and the geometry of the reactor. In the case of a plane-type geometry, this is commonly used in industry (Fig. V-2) [220-223], the transmitted power to the plasma is not only by the inductive coupling, but also by the capacitive coupling, and in these conditions, it is very difficult to find an electric circuit equivalent to the discharge. On the other hand, in the case of pure inductive coupling, the parameters of the equivalent electrical circuit can easily be found. The current Ip flowing in the plasma takes the opposite direction of the excitation current Irf, and this is similar to an electrical transformer. As a result, the exciter coil and the plasma behave like a transformer whose coil represents the primary circuit (*La*, *Ra*) and the plasma represents the secondary circuit (*Lp*, *Rp*) of a transformer. The coupling between the coil and the plasma is then represented by two inductances coupled by a mutual *M* as shown in Fig.V-6. For the capacitive operating mode, the power is coupled with the plasma through the capacitance dielectric C_d and the sheath in contact with the capacitance dielectric C_g and resistance R_g.

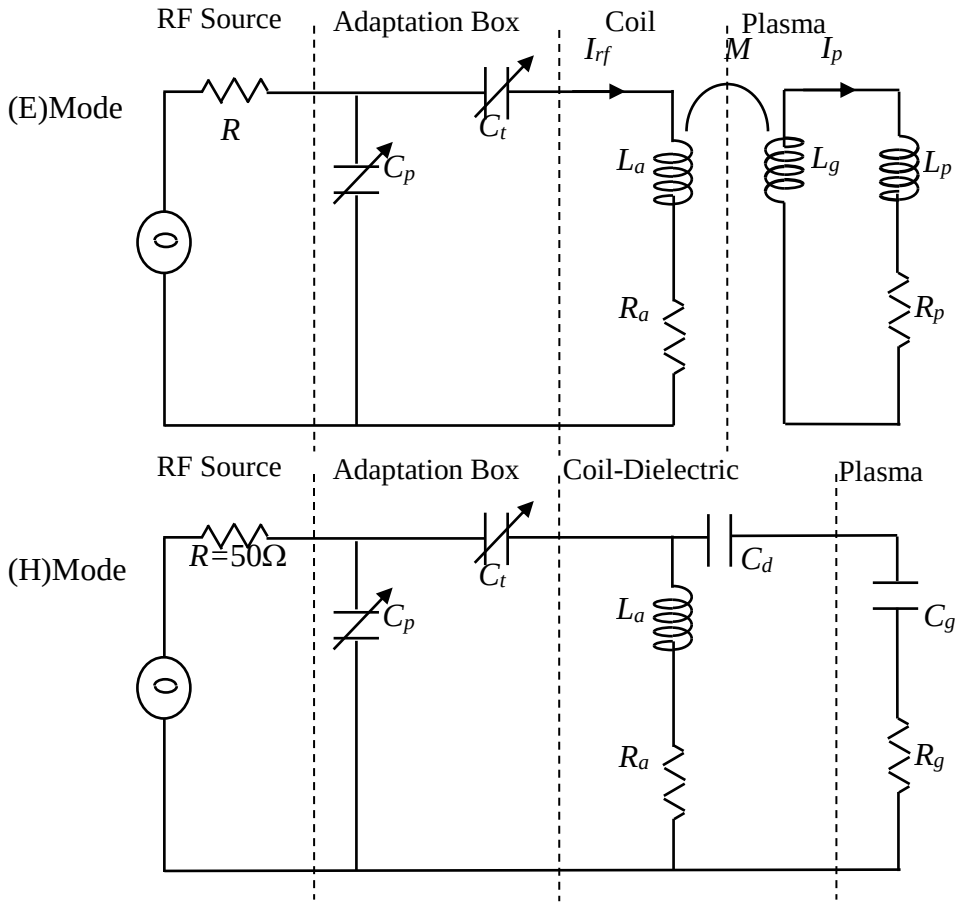

Fig. V-6 : Equivalent Electric Model of Inductive Plasma Mode (H) and Mode (E)

V.4. Description of the model used for the simulation of the inductively coupled plasma in methane

The ICP reactor configuration used in our simulation is that of Gaseous Electronics Conference (GEC) RF Reference Cell, which is developed by Miller *et al.* [224]. Here we will give the adapted dimensions: the quartz window with 10 mm of thickness and distant from the lower electrode by 40.5 mm, the diameter of the stainless-steel lower electrode plate is equal to 165 mm, and the inner diameter of the cell chamber is equal to 251 mm. The coil consists of a five-turn spiral coil outer diameter 102 mm; it is made of copper with 3 mm of diameter.

The center of the coil was powered with a frequency of 13.56 Mhz and the outside winding was grounded. Since the coupling of the coil to the plasma is very sensitive to the positioning and spacing between the coil and coupling window, the coil was pressed against the quartz plate and fixed in place by a slotted five-arm holder that was mounted on the top of the cell.

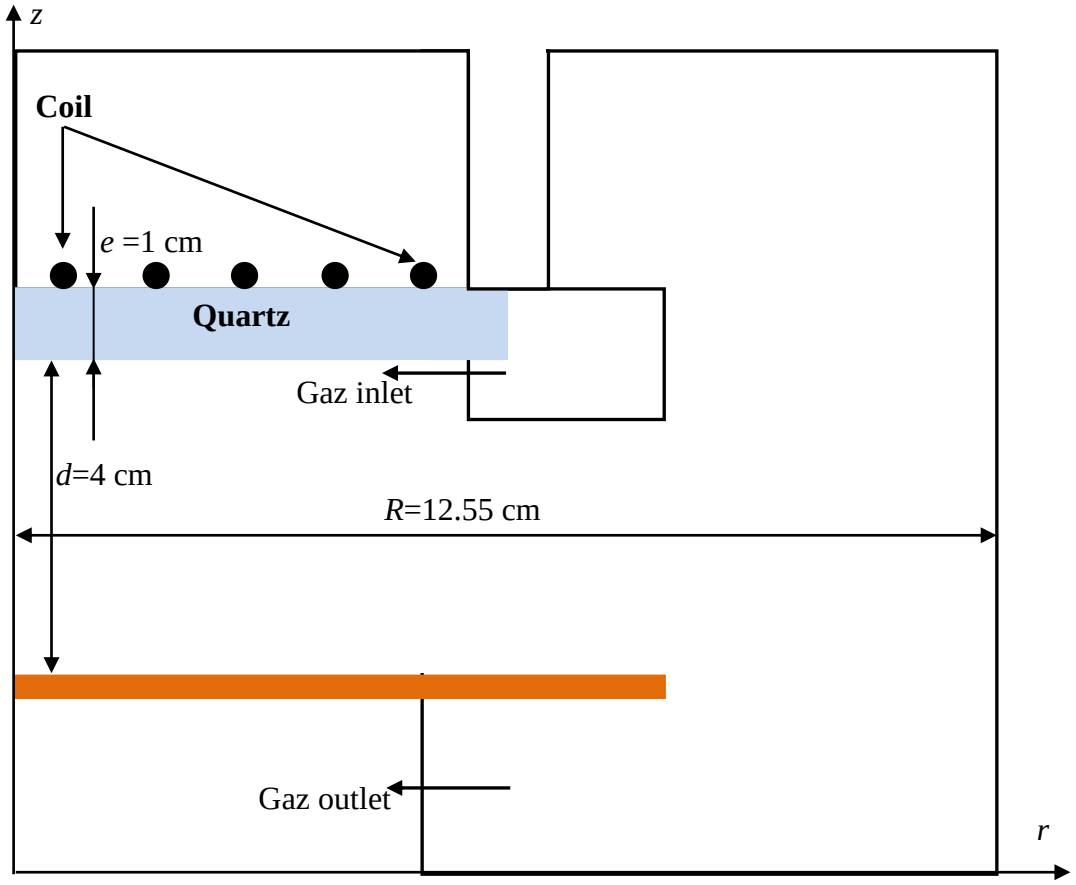

Fig. V-7: Schematic cross section diagram of the inductive reactor to be modeled

The model of the inductively coupled discharge that will be detailed in the following operates in an autonomous way, whose fluid model of species is associated with the electromagnetic equations, to calculate the electric field caused by the temporal variation of the magnetic induction of the coil. In this model we will include the gas flow from the inlet to the outlet by using the Navier-Stokes equation.

V.4.1. Equations of the plasma species

In fluid models, each species is treated as a separate fluid to satisfy mass conservation over the entire area of computation. For electrons, a Maxwellian distribution is considered. This is an appropriate assumption when the electronic energy is less than 15 eV at low pressure . The existence of a high energy tail of the electronic energy distribution function (EEDF) will cause a discrepancy between model predictions and practice. In these models the equations considered are: continuity, momentum and energy for the electrons, while for the ions only the equation of continuity and momentum. All of these equations are closed by the Poisson equation connecting the space charge to the electrostatic potential for inductively coupled

discharges. The equation of continuity and momentum of electrons are given by the following relations:

$$\begin{aligned}&\frac{\partial n_e}{\partial t}+\nabla.\Gamma_e=S_e\\&\frac{\partial\left(\frac{3}{2}n_e k_B T_e\right)}{\partial t}+\nabla.\boldsymbol{\Gamma}_\varepsilon+e\boldsymbol{\Gamma}_e.\mathbf{E}=P_{ind}+W_e\end{aligned}\tag{V-9}$$

where the flow of electrons is given by the following relation:

$$\Gamma_e=-n_e\mu_e\mathbf{E}-\frac{1}{m_e\nu_{en}}\nabla\left(n_e k_B T_e\right)\tag{V-10}$$

and the energy flow of the electrons is given by the following relation:

$$\boldsymbol{\Gamma}_\varepsilon=\frac{5}{2}\left[\boldsymbol{\Gamma}_e k_B T_e-\frac{n_e k_B T}{m_e\nu_{en}}\nabla\left(n_e k_B T_e\right)\right]\tag{V-11}$$

here, n_e is the electron density, m_e is the electron mass, μ_e is the electron mobility, ν_{en} is the electron-neutral collision frequency, T_e is the electronic temperature, E is the electric field vector, and k_B is the Boltzmann constant, and S_e is the electron source term. The term P_{ind} is the term of inductive heating averaged over a period and is obtained from the electromagnetic model. The term W_e represents the transfer of mass and energy to the electrons by collisions with another species of density N_k, it is given by the following relation:

$$W_e=\sum_k\sum_j k_{k,j}n_e N_k\Delta\varepsilon_{j,k}\tag{V-12}$$

The equations of continuity, momentum and energy for ions are given as follows:

$$\begin{aligned}&\frac{\partial n_i}{\partial t}+\nabla.\left(n_i\mathbf{u}_i\right)=S_i\\&\frac{\partial\left(n_i m_i\mathbf{u}_i\right)}{\partial t}+\nabla.\left(n_i m_i\mathbf{u}_i\mathbf{u}_i\right)=\nabla.\left(n_i k_B T_i\right)+Z_i e n_i\mathbf{E}+\mathbf{M}_i\end{aligned}\tag{V-13}$$

Here n_i, $\mathbf{u_i}$, S_i, m_i and Z_i are respectively the density, the velocity vector, the source term, the mass and the charge of the ions, T_i is la temperature of ions, and $\mathbf{M_i}$ represents the collisional transfer of the momentum of ions to neutral species. Finally, the neutral transport in the ground state or in the excited state is governed by the following equation only:

$$\frac{\partial n_*}{\partial t}+\nabla.\left(-D_*\nabla n_*\right)=S_*\tag{V-14}$$

where n_*, D_*, and S_* represent respectively the density, the diffusion coefficient, and the source term of the neutral. The electric field due to the space charge in the plasma and the electric field of the inductive power coupling are treated separately. The electrostatic potential is obtained by solving the Poisson equation:

$$\nabla^2 V = \frac{e}{\varepsilon_0}\left(n_e - \sum_i Z_i n_i \right) \tag{V-15}$$

where ε_0 is the permittivity of the vacuum, and Z_i is the charge of the ions.

V.4.2. Electromagnetic equations of inductive coupling

In the case of the two-dimensional symmetric inductive coupling plasma model, Maxwell's electromagnetic field equations can be reduced to the vector potential **A** as follows:

$$\frac{1}{\mu_0 \mu_r}\nabla^2 \mathbf{A} + \varepsilon_0 \varepsilon_r \omega_{rf}^2 \mathbf{A} = \mathbf{-J} \tag{V-16}$$

where **J** is the current density in the coil, and although J is complex, Im (J) could be set to zero. The RF frequency can generally be up to 13.56 MHz or more, so the skin effect is important for the formation of a surface current. The resolution of this electromagnetic equation gives the distribution of the vector potential **A** in the whole domain of the computation, and only the values obtained in the plasma medium are useful for the coupling with the equation of the electronic energy and in the model through the electric field and the average value of the power density deposited in the plasma. These two quantities can be calculated by the following relations:

$$\begin{aligned} \mathbf{E} &= -\nabla V - \frac{\partial \mathbf{A}}{\partial t} \\ P_{ind} &= \frac{1}{2}\mathrm{Re}\left(\sigma_p\right)\omega_{rf}^2 \left|\mathbf{A}\right|^2 \end{aligned} \tag{V-17}$$

where σ_p is the complex conductivity of the plasma, it is given by the following expression:

$$\sigma_p = \frac{n_e e^2}{m_e\left(\nu_{en} + j\omega_{rf}\right)} \tag{V-18}$$

where m_e and ν_{en}: respectively represent the electronic mass and the actual momentum collision frequency of the motion. The dielectric constant of the plasma ε_p is obtained from the following relation:

$$\varepsilon_p = \varepsilon_0 \left(1 - j \frac{\sigma_p}{\varepsilon_0 \omega_{rf}} \right) \tag{V-19}$$

V.4.3. Navier-Stokes Equations of Neutral Flow

Neutral background gas has an important influence on the distribution of plasma in two aspects: one is that the source/sink where plasma generates or dissipates is proportional to the number density of neutral gas; and the other is that the number density of neutral gas can change the collision frequency of electrons and other particles. In consideration of the influence of neutral background gas and pressure distribution on plasma, so in this model the flow of neutral gas is described by the incompressible Navier-Stokes equation.

$$\begin{aligned} &\rho \frac{\partial \mathbf{u}}{\partial t} - \nabla \eta \left(\nabla \mathbf{u} + (\nabla \mathbf{u})^T \right) + \rho \mathbf{u} \nabla \mathbf{u} + \nabla p = \mathbf{F} \\ &\nabla (\rho \mathbf{u}) = 0 \end{aligned} \tag{V-20}$$

where ρ, η, and u represent the gas density, the dynamic viscosity and the velocity vector, respectively, p is the gas pressure and F is the force. In this case, the force is zero. The boundary conditions of the input and output are defined according to the type of velocity input and the pressure output, and the boundary condition at the wall is simply defined with the Dirichlet condition, it is ie $u = 0$.

V.4.4. Limit Conditions

In order to resolve the equations of this self consistent fluid model, we are used the following limits conditions.

Electrical potential and magnetic potential: The reactor walls are considered perfectly conductive and connected to the ground, this implies that the electric potential and the magnetic vector potential are zero at the metal walls, at the level of the dielectric wall, the electric potential can be obtained taking into account the following condition:

$$\begin{aligned} &\frac{\partial \sigma_s}{\partial t} = \mathbf{n}\mathbf{J}_i + \mathbf{n}\mathbf{J}_e \\ &-\mathbf{n}\left(\mathbf{D}_p - \mathbf{D}_d \right) = \sigma_s \end{aligned} \tag{V-21}$$

where σ_s, $\mathbf{n}$, $\mathbf{J}_i$, $\mathbf{J}_e$, $\mathbf{D}_p$, and $\mathbf{D}_d$: are respectively, the accumulated charge on the surface of the dielectric, the norm of the surface, the density of the ionic current, the density of the

electronic current, the electric displacement vector in the plasma side, and the electric displacement vector in the dielectric side.

Density, flux and energy of species: The electron flow at the walls and electrodes is obtained by using the limit condition of a Maxwellian flux where:

$$\Gamma = \pm\frac{1}{4} n_e v_{e,th} e^{\frac{V}{k_B T_e}}$$
$$v_{e,th} = \sqrt{\frac{8k_B T_e}{\pi m_e}} \quad \text{(V-22)}$$

where the signs ± correspond to the direction of the electron flow, V is the potential of the wall, $v_{e,th}$ is the thermal velocity of the electron. Ignoring the thermal conduction of electrons, the energy flow to the electrodes and the walls is given by:

$$\Gamma_\varepsilon = \frac{5}{2} n_e T_\varepsilon \Gamma_e \quad \text{(V-23)}$$

The ion density and velocity gradients are set to zero at the limits, so:

$$\nabla n_i = 0, \nabla v_i = 0 \quad \text{(V-24)}$$

Flow of the gas: to know the speed of the flow of the neutrals and the distribution of the pressure in the reactor, one must solve the Navier-Stokes equation by taking into account as boundary conditions, the velocity of the gas to the reactor inlet, zero velocity at the walls and electrodes, and constant pressure at the reactor outlet.

V.4.5. Model input parameters

For electrons, mobility is calculated from their cross section and the diffusion coefficient is calculated by the Einstein relation which relates the mobility to the diffusion coefficient. The mobility of the ions is calculated by the relation of Dalgarno while taking a long-range polarization interaction potential and the diffusion coefficient by the Einstein relation, they are expressed as follows:

$$\mu_i = \frac{36}{\sqrt{\alpha_n m_r}}$$
$$\frac{D_i}{\mu_i} = \frac{k_B T_i}{q_i} \qquad \text{(V-25)}$$

With q_i is the ion charge, μ_i is the mobility [$cm^2V^{-1}.s^{-1}$], m_r is the reduced mass ion-neutral given in units a.u.m ,α_n is the polarizability in function of a_0^3 (a_0 is Bohr's radius), D_i is the ionic diffusion coefficient, k_B is the Boltzmann constant, and T_i is the ionic temperature. The diffusion coefficient of excited particles is calculated by taking into account the interaction potential of type *Lennard-Jones*

$$D_* = 0.0018583\sqrt{\frac{T^3}{m_r}}.\frac{1}{p\sigma_{EN}^2\Omega_D}$$
$$\Omega_D = \frac{1.06036}{\Psi^B} + \frac{0.193}{e^{D\Psi}} + \frac{1.03587}{e^{F\Psi}} + \frac{1.76464}{e^{H\Psi}} \qquad \text{(V-26)}$$
$$\sigma_{EN} = \frac{\sigma_E + \sigma_N}{2}, \Psi = \frac{T_g}{\varepsilon_{EN}}, \varepsilon_{EN} = \sqrt{\varepsilon_E \varepsilon_N}$$

Where T and p are the gas temperature (in K) and the pressure (en atm), m_r the reduced mass (in kg), (σ_E, ε_E) and (σ_N, ε_N) are respectively the parameters of *Leonard-Jones* potential of excited particle E and of the particle in the fundamental state N. B=0.15610, D=0.47635, F=1.52996, and H=3.89411.

Finally, the reaction rate with walls and the electrodes can be calculated by:

$$k_* = \frac{D_*}{\Lambda^2} \qquad \text{(V-27)}$$

For a reactor of Radius R and Length L, the length of effective diffusion Λ can be expressed by the following relation:

$$\Lambda^2 = \left[\left(\frac{\pi}{L}\right)^2 + \left(\frac{2.405}{R}\right)^2\right]^{-1} \qquad \text{(V-28)}$$

V.4.6. Chemical model

The reactions between the different species are shown in the appendix (tables: A-1, A-2 and A-3). The species considered in this work are: the electrons, CH_4, C, C_2, C_2H, C_2H_2, C_2H_3, C_2H_4, C_2H_6, C_3H_8, C_4H_{10},H_2,H, CH_3, CH_2, CH, C_2H_5,H, CH_4^+, CH_5^+ ,CH_3^+ ,CH_2^+ ,CH^+, C^+, C_2^+, C_2H^+, $C_2H_2^+$, $C_2H_3^+$, $C_2H_4^+$, $C_2H_5^+$, $C_2H_6^+$,H_3^+, H_2^+, H^+.

V.5. Result and Discussion

The simulation is performed for a GEC RF ICP reactor for pure methane. The model takes into account the motion of the gas in the plasma reactor through solving the Navier-Stokes equation. The gas flow at the inlet and the gas pressure are taken constant in this study with values of 100 sccm (standard cubic centimeters per minute) and 25 mTorr respectively. The results shown in figures (Fig.V-8, Fig.V-9, Fig.V-10, Fig.V-11, Fig.V-11, Fig.V-12, and Fig.V-14,) are obtained for input power deposition in gas of 270W. Figure (V-8) shows the spatial variation of the gas flow velocity in the reactor. This speed is obtained by the resolution of the Navier-Stokes equation; it clearly shows that the velocity is very important at the inlet of the reactor than other sides; its value at the reactor outlet is almost half of that at the inlet due the large outlet section in the comparison of that of the inlet. In the figure (V-9) we show the modulus of the magnetic potential created by the coil, the electric field induced by the temporal variation of this potential is the source of energy that will be recovered by the electrons to maintain the electric discharge. The spatial variation of the electric potential is illustrated in figure (V-10). Unlike the capacitively coupled discharge where the plasma potential is large, in inductively coupled discharges is low (about 20 V in our case), because this latter is mainly due to the presence of space charge. In the inductively coupled discharges, the electrons density is very higher than that in capacitively coupling discharges because of the confinement of electrons by the magnetic field, in our conditions it is about 4×1012 cm^{-3} (see figure V-11). The heating of the electrons is mainly due to the electric field induced by the temporal variation of the magnetic potential vector, so it is logical that the maximum of this is located in the zone where this potential is important, as it is shown in figure (IV-12).

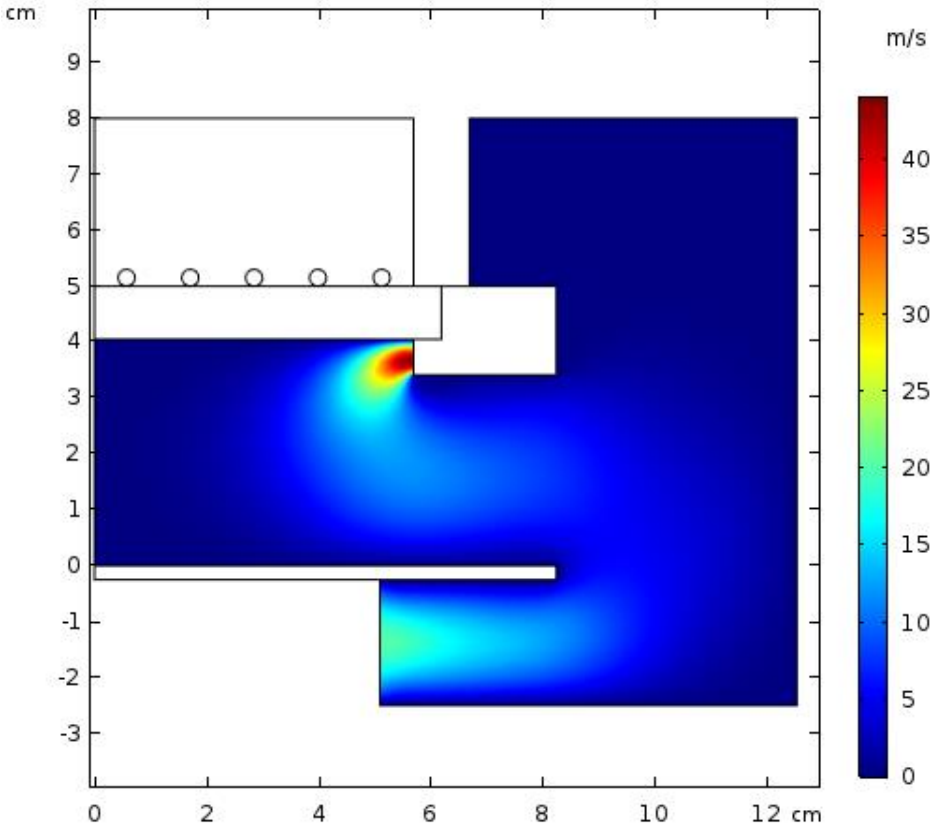

Fig. V-8: Spatial distribution of the gas velocity in the reactor

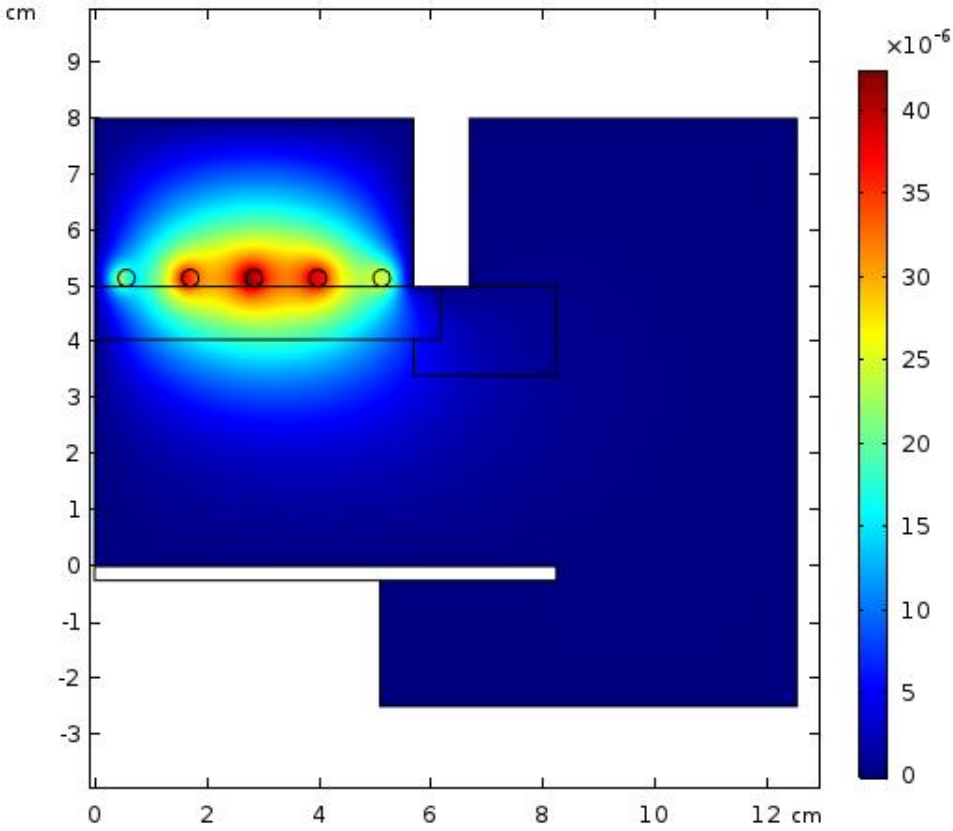

Fig. V-9: Spatial variation of the magnetic potential vector

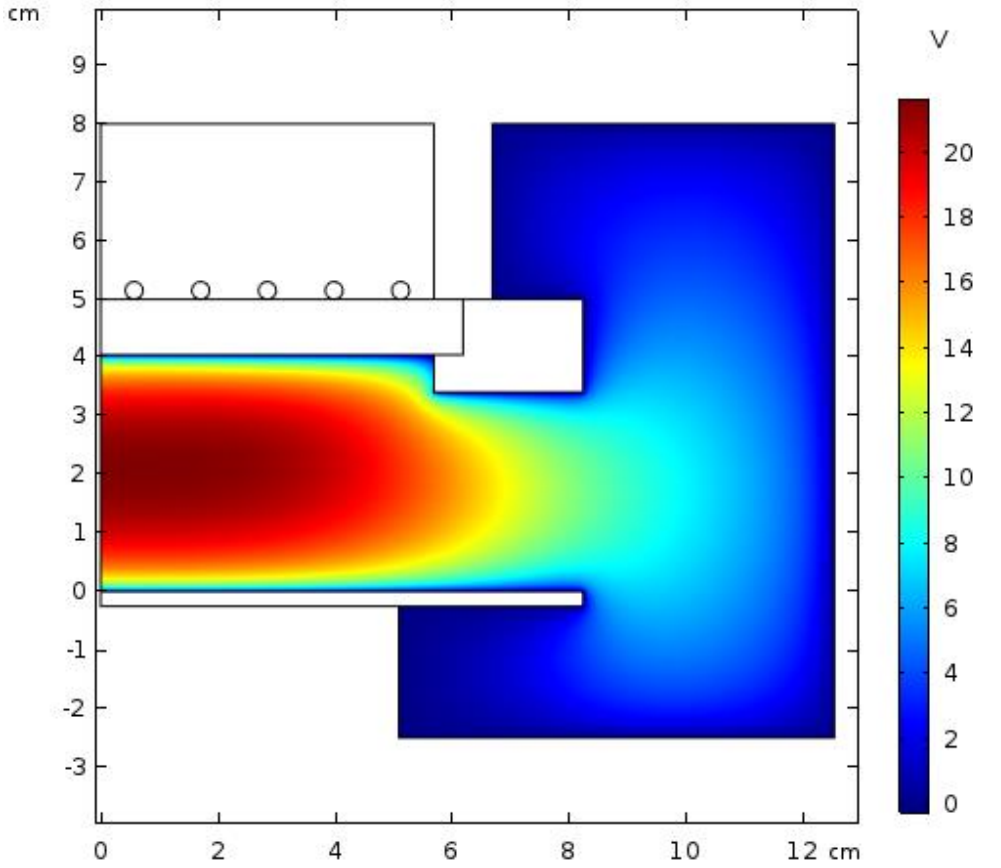

Fig. V-10: Spatial variation of the electric potential

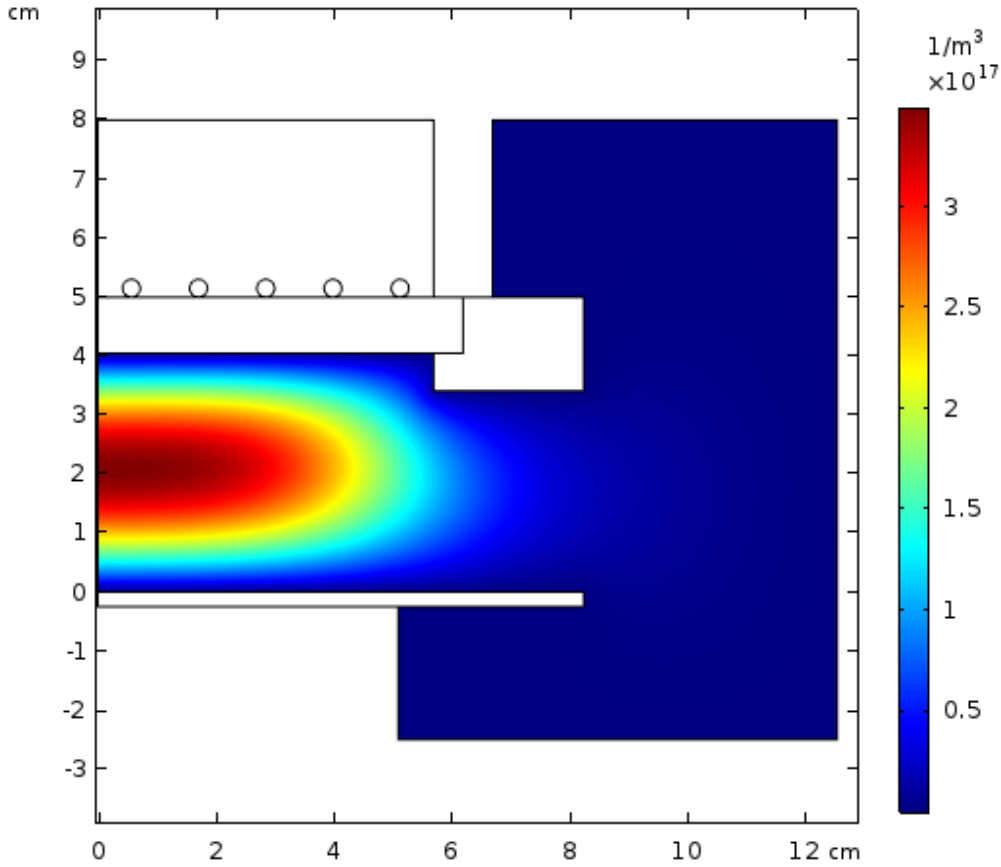

Fig. V-11: Spatial variation of the electron density

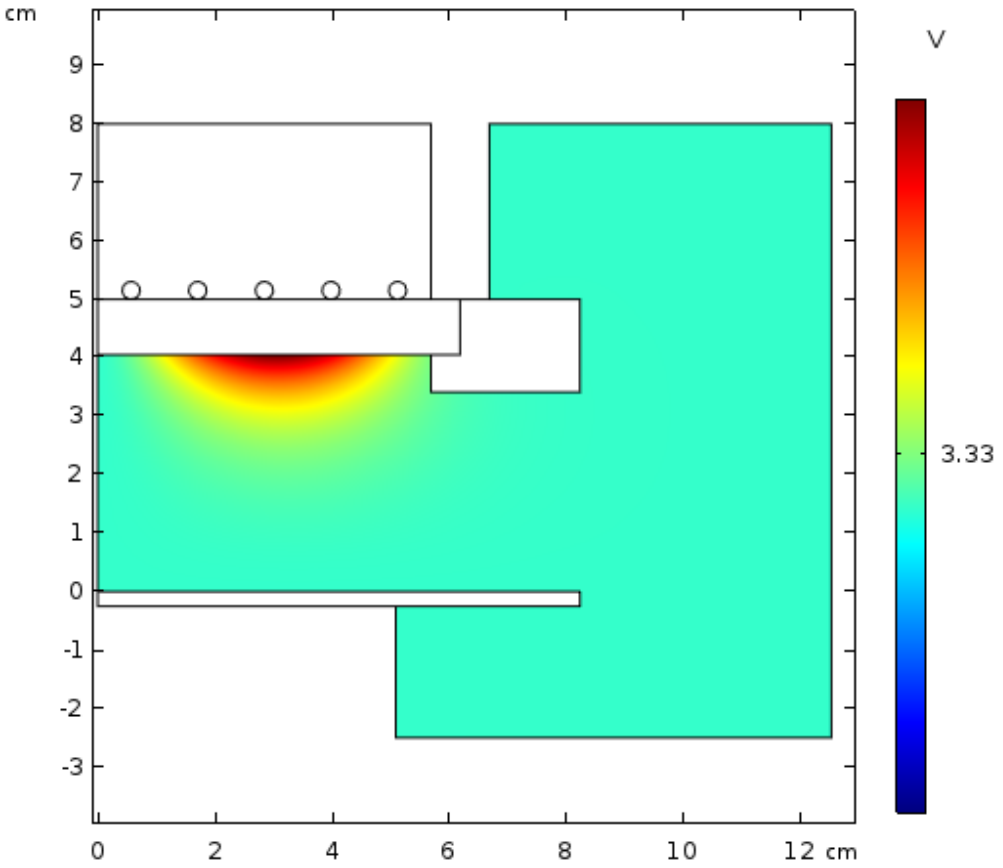

Fig. V-12: Spatial variation of the electron temperature

Figure V-13 shows the profile density of different ions at the center axis of discharge (r=0) for input power of 270 W, it shows that the most amount ions are: CH_3^+, CH_4^+, $C_2H_4^+$, and $C_2H_2^+$, respectively. The principal reactions which create CH_3^+ and CH_4^+ are: $e+CH_4 \Rightarrow 2e+CH_3^++H$ and $e+CH_4 \Rightarrow 2e+CH_4^+$ respectively, where the rate of CH_4^+ production is higher that of CH_3^+. So the dominance of CH_3^+ can be explained only by the loss rates of these ions. In this operating conditions, the loss of CH_4^+ is done through two main processes $CH_4^++CH_4 \Rightarrow CH_5^++CH_3$ and $CH_4^++H_2 \Rightarrow CH_5^++H$, contrariwise the loss of CH_3^+ is done through one important process only $CH_3^++CH_4 \Rightarrow C_2H_5^++H_2$. CH_5^+ and $C_2H_5^+$ ions are not appear successively in the third and fourth positions due to their high loss rates through the reaction $C_2H_5^++H \Rightarrow C_2H_4^++H_2$, $CH_5^++C_2H_4 \Rightarrow C_2H_5^++CH_4$, $CH_5^++C_2H_2 \Rightarrow C_2H_3^++CH_4$. The profile density of different neutrals at the center axis of discharge (r=0) is shown figure V-14. This figure indicate that the first important species after the CH_4 in these conditions is the hydrogen molecule (H_2), this molecule is created primarily by the first process in the plasma which is the electron impact collision, these reactions are the dissociation into: CH_2+H_2, $CH+H_2+H$, and $C+2H_2$, and also through dissociative ionization of methane molecule to: $CH_2^++H_2$, CH^++H_2+H, and C^++2H_2. Other reactions also lead to increase the amount of the H_2 produced, such as $CH_4+H \Rightarrow CH_3+H_2$ and $CH_3+H \Rightarrow CH_2+H_2$.

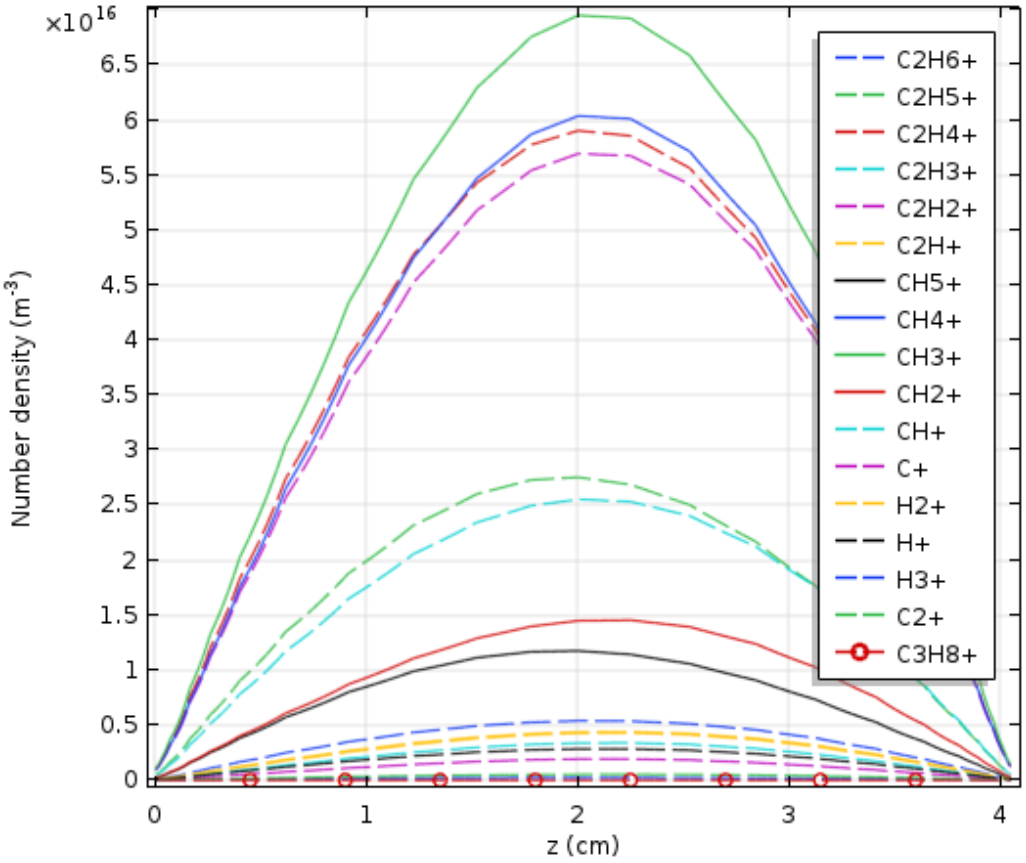

Fig. V-13: Mole fraction distribution of the different neutrals species at the reactor center

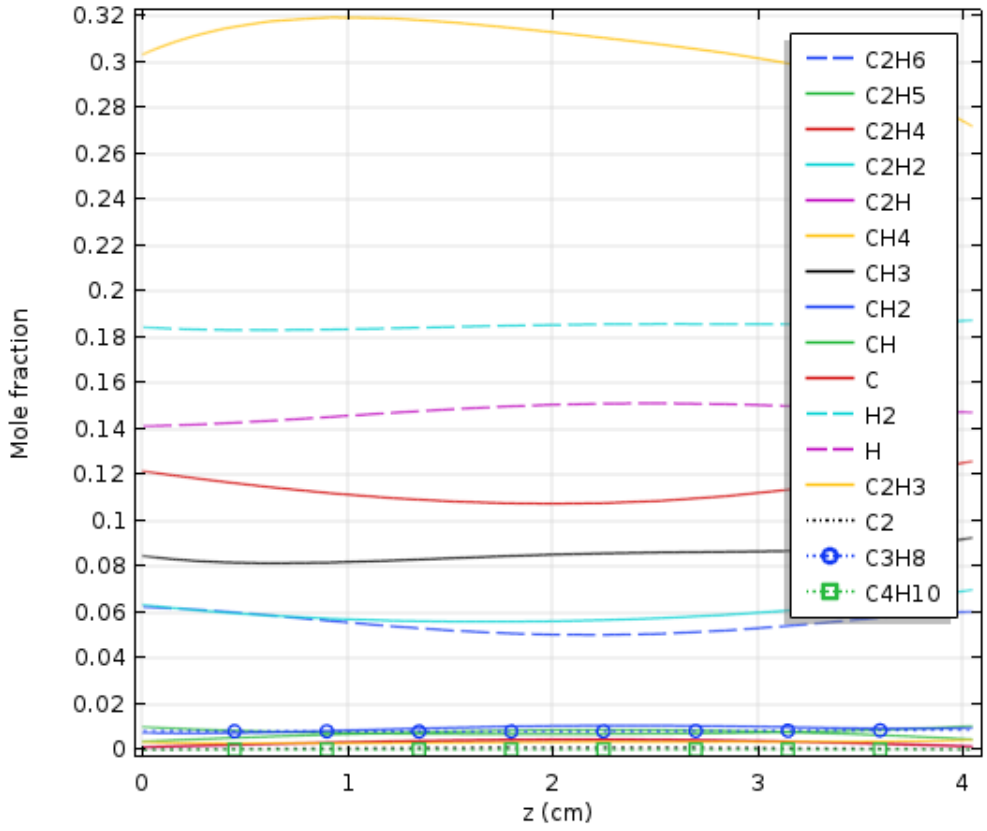

Fig. V-14: Mole fraction distribution of the different neutrals species at the reactor center

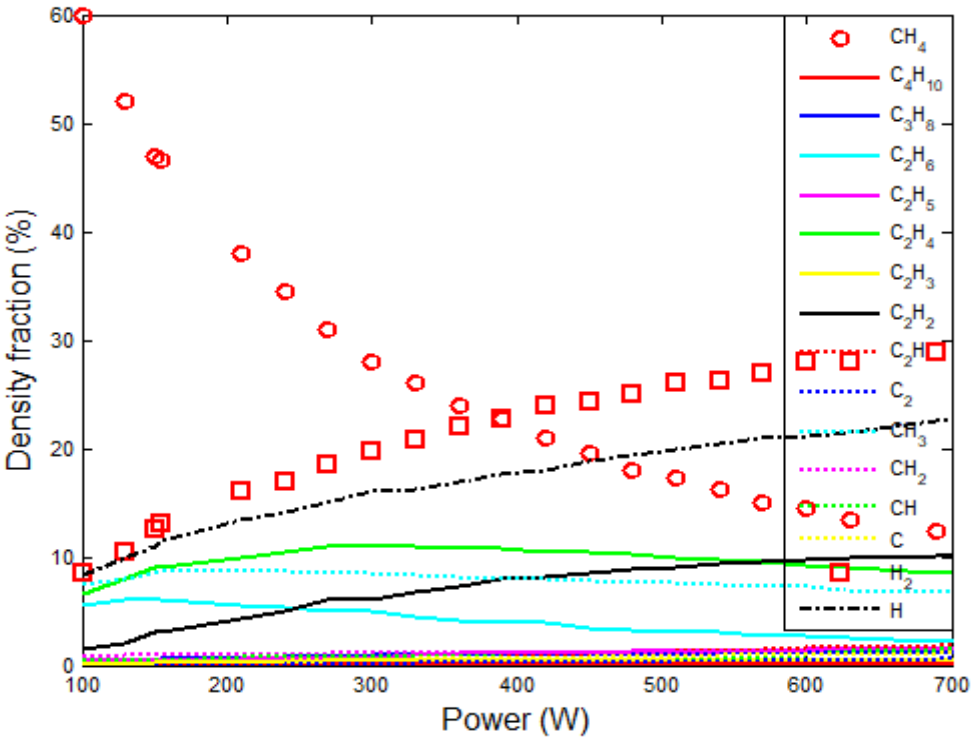

Fig. V-15: Variation of neutrals molecules and atoms production and methane in function of input power.

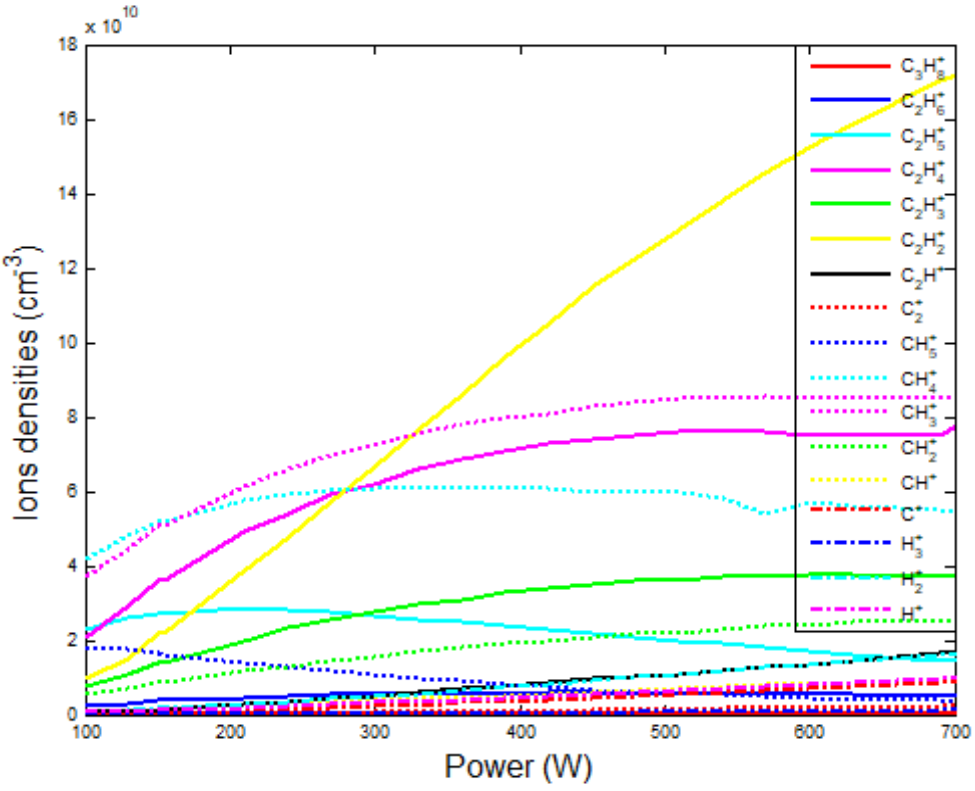

Fig. V-16: Variation of neutrals molecules and atoms production and methane in function of input power.

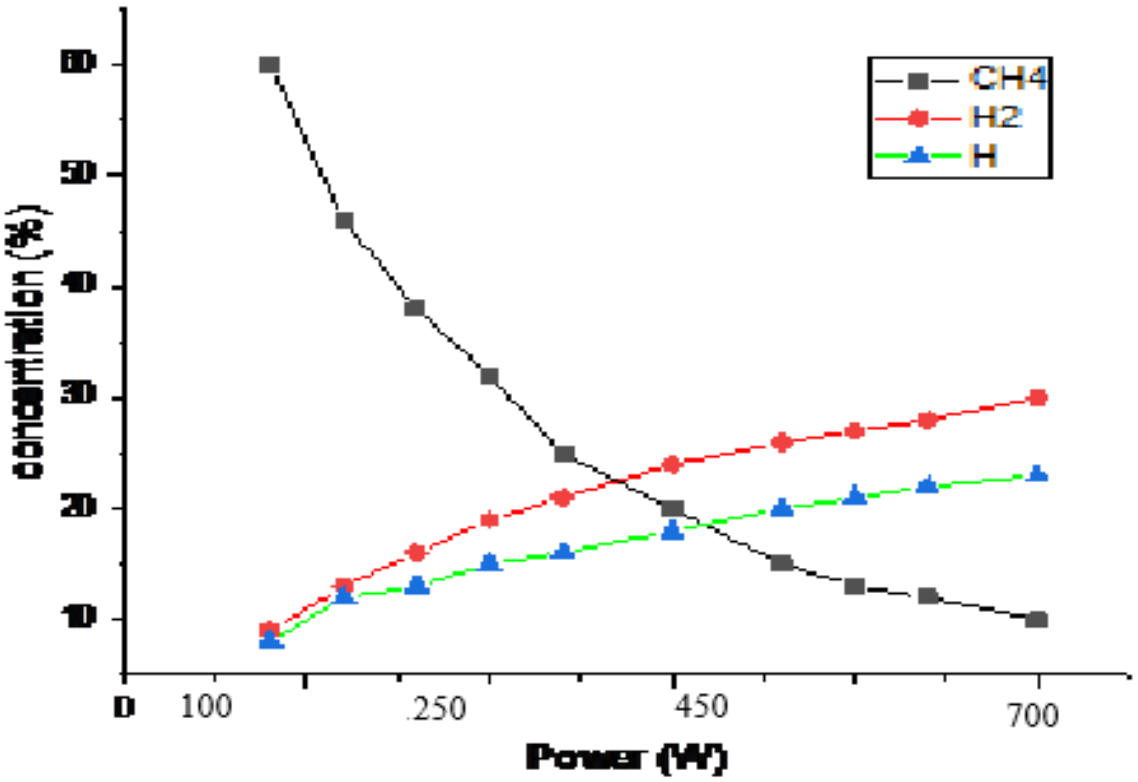

Fig. V-17: Variation of Hydrogen Production (H2 and H) and Methane dissociation in function of input power

We resume in the figures V-15 and V-16, the evomution of neutrals molecules, atoms production with methane and ions redpectively in function of input power from 100 W to 700W, we can see that the dissociation increase mainly between 100W and 600W and incrase slowly after because of the quantity of CH_4 is small and the reaction with CH_4 become weak. The figure V-17 shows just the evolution of hydrogen (atom_H and molecule_H_2) and the methane in function of increasing input power.

The CH_3, CH_2 and CH are produced firstly by the electronic impact collision (e+CH_3+H, 2e+CH_3+H^+, e+CH_2+H_2, 2e+CH_2+H_2^+ ande+CH+H_2+H), but as we can see in the figure V-14 that the amount of CH_3 is just about 8%, and less than 1% for CH_2 and CH. This is because of these species mainly participate in the production of the most abundant neutrals (H_2, H, C_2H_2 and C_2H_4) especially by reaction with CH_4 for example the following reactions:

CH_4+CH_3 => C_2H_5+H_2, CH_4+CH_2 => C_2H_4+H_2, CH_4+CH_3 => CH_3+CH_3, CH_4+CH=> C_2H_4+H, CH_4+CH=> C_2H_5, CH_4+CH_3=> C_2H_5+H_2, CH_3+CH_3 => C_2H_5+H, CH_3+CH_2 => C_2H_4+H, CH_3+C => C_2H_2+H, CH_2+CH_2 => C_2H_4, CH_2+CH_2 => C_2H+H_2, CH_2+CH_2 => C_2H_2+2H, CH_2+CH => C_2H_2+H, and CH+CH => C_2H_2.

V.6. Conclusion

The study achieved out during this work concerns the numerical modeling of a capacitively coupled cold electric discharge plasma. The adopted model considers the plasma as a continuous fluid medium.

In this model, ions and electrons are described by the conservation and momentum transfer equations for ions and electrons and the conservation energy equation for electrons, all these equations are coupled to the Poisson equation for the electric field, with the approximation of the local field.

The work carried out has highlighted a number of phenomena taking place in the methane plasma especially the densities of existing species.

The study achieved out during this work concerns the numerical modeling of inductively coupled cold electric discharge plasma. The results show that the first important species at the model simulation conditions is the hydrogen molecule, and the second important species is the hydrogen atom, these two species are created firstely by methane molecule dissociation into: CH_3+H, CH_2+H_2, CH+H_2+H, and C+2H_2, and also through dissociative ionization of methane molecule into: CH_3^++ H, CH_2^++H_2, CH^++H_2+H, and C^++2H_2. the methane molecule mole fraction is coming in the third position (10%), which indicate that the rate conversion of methane in these conditions is 90%.

Methane inductively coupled plasma is rich of different species, and especially of hydrogen molecule species. This plasma can be used as source for the hydrogen.

OVERALL CONCLUSION AND PERSPECTIVES

Overall conclusion and perspectives

This work is part of the general context of radiofrequency plasmas, encountered in many research fields such as the micro and Nano electronics industry for the deposition of thin films or for etching patterns on silicon substrates, as well as on new ones; materials for photonics. The purpose of this study was to gain a better understanding of the discharge and plasma.

The main objective of this thesis is to develop a numerical model that allows the multidimensional simulation of the distribution of the different charged particles (electrons and positive ions) and neutral species (metastable), the potential and the electric field, the electronic temperature and then the reaction rate in his plasma reactor, for a radiofrequency discharge and for an electropositive polyatomic gas (CH_4 in the case of capacitive and inductive coupling). What interests us in this work is the quantity of hydrogen that can be obtained in these two types of reactors.

For this, and after applying some simplifying hypotheses and initial and boundary conditions, we have developed a self - consistent fluid - type simulation model to describe the behavior of the different plasma parameters. The model developed is based on the resolution of the first three moments of the Boltzmann equation. These three moments, which are the mass equation, the momentum transfer continuity equation, and the electron energy equation are coupled to the Poisson equation and the Maxwell equations, in the case of the ICP discharge, for to form a system of nonlinear and strongly coupled equations. We therefore proceeded to its resolution by using commercial software Comsol Multiphysics which is based on the finite element method. The elaborate 1D and 2D fluid models allowed us to simulate the composition of electropositive plasma produced in two different reactors: (i) the capacitive reactor (CCP) and (ii) the inductive reactor (ICP). Due to the lack of data for methane gas especially the cross sections for e + CH_4, the first part of this work was for the accumulation of these data.

The first simulation carried out in this work, described in the fourth chapter of this manuscript, made it possible to highlight the main phenomena involved in a capacitively coupled discharge. The results obtained show that the production of hydrogen in this type of reactor is very low due to the weak dissociations of methane.

The results are given, both for a capacitively coupled discharge in terms of spatio-temporal evolution of the species created in the discharge (electrons, ions, metastables), of the electronic temperature and also of the electric potential and field in the sheaths. and the plasma region.

In the fifth chapter, for the simulation of the inductive discharge we have found that the increase of the power leads to an increase in the dissociation rate of the methane which attains 90% and the production of the molecule of the hydrogen reaches 30% and 22% of the hydrogen atom. This result shows us that this type of reactor can be used for hydrogen production.

The work carried out opens the way to many perspectives, some of which are given below.

- ✓ Study other types of discharges, such as the Barrier Dielectric Discharge (DBD) and the DBD Packed Bed for the case of methane.
- ✓ Treat numerically the radiofrequency discharges for other molecular gases.

Table: A-1: Electronic impact reactions with threshold energy (CH_4, CH_3, CH_2, CH, C, H, H_2, C_2H_2, C_2H_4, and C_2H6).

N	reactions	Threshold (eV)
01	$e+CH_4 \Rightarrow e+CH_3+H$	8.8
02	$e+CH_4 \Rightarrow e+CH_2+H_2$	9.4
03	$e+CH_4 \Rightarrow e+CH+H_2+H$	12.5
04	$e+CH_4 \Rightarrow e+C+2H_2$	14
05	$e+CH_4 \Rightarrow 2e+CH_4^+$	12.63
06	$e+CH_4 \Rightarrow 2e+H+CH_3^+$	14.25
07	$e+CH_4 \Rightarrow 2e+H2+CH_2^+$	15.1
08	$e+CH_4 \Rightarrow 2e+H+H_2+CH^+$	19.9
09	$e+CH_4 \Rightarrow 2e+2H_2+C^+$	19.6
10	$e+CH_4 \Rightarrow 2e+CH_2+H_2^+$	20.1
11	$e+CH_4 \Rightarrow 2e+CH_3+H^+$	18
12	$e+CH_3 \Rightarrow e+CH_2+H$	6.9
13	$e+ CH_3 \Rightarrow e+CH+H_2$	7.2
14	$e+ CH_3 \Rightarrow e+CH+2H$	12.4
15	$e+ CH_3 \Rightarrow e+C+H_2+H$	10.6
16	$e+ CH_3 \Rightarrow 2e+CH_3^+$	9.84
17	$e+ CH_3 \Rightarrow 2e+CH_2^++H$	15.12
18	$e+ CH_3 \Rightarrow 2e+CH^++H_2$	15.74
19	$e+ CH_3 \Rightarrow 2e+H^++CH_2$	18.42
20	$e+ CH_3 \Rightarrow 2e+C^++H+H_2$	19.50
21	$e+ CH_3 \Rightarrow 2e+H_2^++CH$	20.18
22	$e+CH_2 \Rightarrow e+CH+H$	6.4
23	$e+CH_2 \Rightarrow e+C+H_2$	6.6
24	$e+CH_2 \Rightarrow e+C+2H$	10.4
25	$e+CH_2 \Rightarrow 2e+CH_2^+$	10.4
26	$e+CH_2 \Rightarrow 2e+CH^++H$	15.53
27	$e+CH_2 \Rightarrow 2e+C^++H2$	14.67
28	$e+CH_2 \Rightarrow 2e+H^++CH$	18.01
29	$e+CH_2 \Rightarrow 2e+H_2^++C$	18.83
30	$e+CH \Rightarrow e+C+H$	5.3
31	$e+CH \Rightarrow 2e+CH^+$	10.64
32	$e+CH \Rightarrow 2e+C^++H$	14.74
33	$e+CH \Rightarrow 2e+H^++C$	17.07
34	$e+C \Rightarrow 2e+C^+$	11.26
35	$e+H \Rightarrow 2e+H^+$	13.6
36	$e+H_2 \Rightarrow e+H+H$	15.0
37	$e+H_2 \Rightarrow e+H+H$	16.6
38	$e+H_2 \Rightarrow 2e+H_2^+$	15.4
39	$e+H_2 \Rightarrow 2e+H+H^+$	18.1
40	$e+C_2H_2 \Rightarrow e+C_2H+H$	7.5
41	$e+C_2H_2 \Rightarrow e+C_2+H_2$	8.7
42	$e+C_2H_2 \Rightarrow e+C_2+2H$	11.38
43	$e+C_2H_2 \Rightarrow e+CH+CH$	10.6
44	$e+C_2H_2 \Rightarrow e+CH_2+C$	9.8
45	$e+C_2H_2 \Rightarrow 2e+C_2H_2^+$	11.4
46	$e+C_2H_2 \Rightarrow 2e+C_2H^++H$	16.48
47	$e+C_2H_2 \Rightarrow 2e+C_2^++H_2$	16.76
48	$e+C_2H_2 \Rightarrow 2e+CH^++CH$	20.61

49	$e+C_2H_2=>2e+C^++CH_2$	20.35
50	$e+C_2H_2=>2e+H^++C_2H$	18.46
51	$e+C_2H_4=>e+C_2H_3+H$	6.9
52	$e+C_2H_4=>e+C_2H_2+H_2$	5.8
53	$e+C_2H_4=>e+C_2H_2+2H$	6.5
54	$e+ C_2H_4=>e+C_2H+H_2+H$	8.4
55	$e+ C_2H_4=>e+CH3+CH$	8.7
56	$e+ C_2H_4=>e+CH_2+CH_2$	8.9
57	$e+ C_2H_4=>e+C+CH_4$	8.1
58	$e+ C_2H_4=>2e+C_2H_4+$	11.51
59	$e+ C_2H_4=>2e+C_2H_3^++H$	13.09
60	$e+ C_2H_4=>2e+C_2H_2^++H2$	13.23
61	$e+ C_2H_4=>2e+C_2H^++H_2+H$	19.06
62	$e+ C_2H_4=>2e+C_2^++2H_2$	20.09
63	$e+ C_2H_4=>2e+CH_3^++CH$	16.91
64	$e+ C_2H_4=>2e+CH_2^++CH_2$	17.94
65	$e+ C_2H_4=>2e+CH^++CH_3$	18.2
66	$e+C_2H_4=>2e+C^++CH_4$	18.94
67	$e+ C_2H_6=>e+C_2H_5+H$	7.45
68	$e+C_2H_6=>e+C_2H_4+H2$	4.0
69	$e+ C_2H_6=>e+C_2H_3+H_2+H$	9.4
70	$e+ C_2H_6=>e+C_2H_2+2H_2$	6.2
71	$e+C_2H_6=>e+CH_4+CH_2$	6.95
72	$e+C_2H_6=>e+CH_3+CH_3$	6.38
73	$e+C_2H_6=>2e+C_2H_6^+$	11.52
74	$e+C_2H_6=>2e+C_2H_5^++H$	12.50
75	$e+C_2H_6=>2e+C_2H_4^++H_2$	11.43
76	$e+C_2H_6=>2e+C_2H_3^++H_2+H$	14.51
77	$e+C_2H_6=>2e+C_2H_2^++2H_2$	14.65
78	$e+C_2H_6=>2e+C_2H^++2H_2+H$	17.73
79	$e+C_2H_6=>2e+C_2^++3H_2$	21.01
80	$e+C_2H_6=>2e+CH_3^++CH_3$	13.51
81	$e+C_2H_6=>2e+CH_2^++CH_4$	16.05
82	$e+C_2H_6=>2e+CH^++CH_4+H$	19.1
83	$e+C_2H_6=>2e+C^++CH_4+H_2$	18.77

Table A-3: Wall reactions with sticking coefficient (for ions we assume that the sticking coefficient is 1).

N	Wall reaction	Sticking coefficient	Ref
01	CH_2	0.026	[26]
02	CH_3	0.001	[26]
03	CH_4	0.01	[26]
04	C_2H	0.8	[26]
05	C_2H_3	0.3	[26]
06	C_2H_5	0.01	[26]
07	H	0.07	[26]
08	C	1	[26]
09	C_2	1	[26]

References

[1] Mizeraczyk, J., Urashima, K., Jasiński, M., & Dors, M. (2014). Hydrogen production from gaseous fuels by plasmas—a review. *Int. J. Plasma Env. Sci. Technol*, *8*(2), 89-97.

[2] Hrabovsky, M., Hlina, M., Kopecky, V., Maslani, A., Krenek, P., Serov, A., & Hurba, O. (2018). Steam plasma methane reforming for hydrogen production. *Plasma Chemistry and Plasma Processing*, *38*(4), 743-758.

[3] Jasiński, M., Dors, M., Nowakowska, H., Nichipor, G. V., & Mizeraczyk, J. (2011). Production of hydrogen via conversion of hydrocarbons using a microwave plasma. *Journal of Physics D: Applied Physics*, *44*(19), 194002.

[4] Moshrefi, M. M., & Rashidi, F. (2018). Hydrogen production from methane decomposition in cold plasma reactor with rotating electrodes. *Plasma Chemistry and Plasma Processing*, *38*(3), 503-515.

[5]Dors, M., Izdebski, T., Berendt, A., & Mizeraczyk, J. (2012). Hydrogen production via biomethane reforming in DBD reactor. *Int J Plasma Environ Sci Technol*, *6*(2), 93-97.

[6] R Dagle, V Dagle, M Bearden, J Holladay, T Krause and S Ahmed (2017). An Overview of Natural Gas Conversion Technologies for Co-Production of Hydrogen and Value-Added Solid Carbon ProductsAn Overview of Natural Gas Conversion Technologies for Co-Production of Hydrogen and Value-Added Solid Carbon Products.

[7]Sobhansarbandi, S., Maharjan, L., Fahimi, B., & Hassanipour, F. (2018). Thermal Fluid Analysis of Cold Plasma Methane Reformer. *Fluids*, *3*(2), 31.

[8] Malik, M. A., & Malik, S. A. (1999). Catalyst enhanced oxidation of VOCs and methane in cold-plasma reactors. *Platinum Metals Review*, *43*(3), 109-113.

[9]Malik, M. A., & Malik, S. A. (1999). Catalyst enhanced oxidation of VOCs and methane in cold-plasma reactors. *Platinum Metals Review*, *43*(3), 109-113.

[10] Venugopal, A., Kumar, S. N., Ashok, J., Prasad, D. H., Kumari, V. D., Prasad, K. B. S., & Subrahmanyam, M. (2007). Hydrogen production by catalytic decomposition of methane over Ni/SiO2. *International Journal of Hydrogen Energy*, *32*(12), 1782-1788.

[11] Kalamaras, C. M., & Efstathiou, A. M. (2013). Hydrogen production technologies: current state and future developments. In *Conference papers in science* (Vol. 2013). Hindawi.

[12]Longmier, B. W., Gallimore, A. D., & Hershkowitz, N. (2012). Hydrogen production from methane using an RF plasma source in total nonambipolar flow. *Plasma Sources Science and Technology*, *21*(1), 015007.

[13] Dixon, R. K., Li, J., & Wang, M. Q. (2016). Progress in hydrogen energy infrastructure development—addressing technical and institutional barriers. In *Compendium of Hydrogen Energy* (pp. 323-343). Woodhead Publishing.

[14] Niaz, S., Manzoor, T., & Pandith, A. H. (2015). Hydrogen storage: Materials, methods and perspectives. *Renewable and Sustainable Energy Reviews*, *50*, 457-469.

[15]Zacharia, R. (2015). Review of solid state hydrogen storage methods adopting different kinds of novel materials. *Journal of Nanomaterials*, *2015*, 4.

[16]ICCT 'The International Council On Clean Transportation'. (2017). Developing hydrogen fueling infrastructure for fuel cell vehicles: A status update.

[17] Johnson, J. (2016). Fossil-fuel methane emissions underestimated. *Chemical & Engineering News*, *94*(40), 16-16.

[18] Crabtree, R. H. (1995). Aspects of methane chemistry. *Chemical Reviews*, *95*(4), 987-1007.

[19]Mohajan, H. (2011). Dangerous effects of methane gas in atmosphere.

[20] Skorek, A., & Włodarczyk, R. (2018). The Use of Methane in Practical Solutions of Environmental Engineering. *Journal of Ecological Engineering*, *19*(2).

[21] Daniel Zavala-Araiza, David R. Lyon, Ramón A. Alvarez, Kenneth J. Davis, Robert Harriss, Scott C. Herndon, Anna Karion, Eric Adam Kort, Brian K. Lamb, Xin Lan, Anthony J. Marchese, Stephen W. Pacala, Allen L. Robinson, Paul B. Shepson, Colm Sweeney, Robert Talbot, Amy Townsend-Smallm, Tara I. Yacovitch, Daniel J. Zimmerle, and Steven P. Hamburg. (2015). Reconciling divergent estimates of oil and gas methane emissions. *Proceedings of the National Academy of Sciences*, *112*(51), 15597-15602.

[22] Townsend-Small, A., Marrero, J. E., Lyon, D. R., Simpson, I. J., Meinardi, S., & Blake, D. R. (2015). Integrating source apportionment tracers into a bottom-up inventory of methane emissions in the Barnett Shale hydraulic fracturing region. *Environmental science & technology*, *49*(13), 8175-8182.

[23] Daniel Zavala-Araiza, David Lyon, Ramón A. Alvarez, Virginia Palacios, Robert Harriss, Xin Lan, Robert Talbot, and Steven P. Hamburg. (2015). Toward a functional definition of methane super-emitters: Application to natural gas production sites. *Environmental science & technology*, *49*(13), 8167-8174.

[24] Smith, M. L., Kort, E. A., Karion, A., Sweeney, C., Herndon, S. C., & Yacovitch, T. I. (2015). Airborne ethane observations in the Barnett Shale: Quantification of ethane flux and attribution of methane emissions. *Environmental science & technology*, *49*(13), 8158-8166.

[25] Harriss, R., Alvarez, R. A., Lyon, D., Zavala-Araiza, D., Nelson, D., & Hamburg, S. P. (2015). Using multi-scale measurements to improve methane emission estimates from oil and gas operations in the Barnett Shale region, Texas.

[26] Johnson, D. R., Covington, A. N., & Clark, N. N. (2015). Methane emissions from leak and loss audits of natural gas compressor stations and storage facilities. *Environmental science & technology*, *49*(13), 8132-8138.

[27] Lyon, D. R., Zavala-Araiza, D., Alvarez, R. A., Harriss, R., Palacios, V., Lan, X., ... & Herndon, S. C. (2015). Constructing a spatially resolved methane emission inventory for the Barnett Shale region. *Environmental science & technology*, *49*(13), 8147-8157.

[28] Zavala-Araiza, D., Alvarez, R. A., Lyon, D. R., Allen, D. T., Marchese, A. J., Zimmerle, D. J., & Hamburg, S. P. (2017). Super-emitters in natural gas infrastructure are caused by abnormal process conditions. *Nature communications*, *8*, 14012.

[29] Yacovitch, T. I., Herndon, S. C., Pétron, G., Kofler, J., Lyon, D., Zahniser, M. S., & Kolb, C. E. (2015). Mobile laboratory observations of methane emissions in the Barnett Shale region. *Environmental science & technology*, *49*(13), 7889-7895.

[30] Wang, A., Austin, D., Qian, H., Zeng, H., & Song, H. (2018). Catalytic Valorization of Furfural under Methane Environment. *ACS Sustainable Chemistry & Engineering*, *6*(7), 8891-8903.

[31] U.S.Department of Energy Hydrogen Program. (2018). Hydrogen & Our Energy Future. www.hydrogen.energy.gov

[32] Sürer, M. G., & Arat, H. T. (2017). State of art of hydrogen usage as a fuel on aviation. European Mechanical Science, 2(1), 20-30.

[33] Bicer, Y., & Dincer, I. (2017). Life cycle evaluation of hydrogen and other potential fuels for aircrafts. International Journal of Hydrogen Energy, 42(16), 10722-10738.

[34] Al-Baghdadi, M. A. S., & Al-janabi, H. A. S. (2005). Optimization study of proton exchange membrane fuel cell performance. *Turkish Journal of Engineering and Environmental Sciences*, *29*(4), 235-240.

[35] Fărcaş, A. C., & Dobra, P. (2014). Adaptive control of membrane conductivity of PEM fuel cell. *Procedia Technology*, *12*, 42-49.

[36]Shamim, S., Sudhakar, K., Choudhary, B., & Anwar, J. (2015). A review on recent advances in proton exchange membrane fuel cells: materials, technology and applications. *Advances in Applied Science Research*, *6*(9), 89-100.

[37] Rahimnejad, M., Bakeri, G., Najafpour, G., Ghasemi, M., & Oh, S. E. (2014). A review on the effect of proton exchange membranes in microbial fuel cells. *Biofuel Research Journal*, *1*(1), 7-15.

[38] Marjan Bele, Matija Gatalo, Primož Jovanoviˇc, Francisco Ruiz-Zepeda, Martin Šala, Ervin Šest, Nejc Hodnik, Stanko Hoˇcevar, Irene Gatto, Ada Saccà, Antonino S. Aricò and Miran Gaberšˇcek. (2019). Insight on Single Cell Proton Exchange Membrane Fuel Cell Performance of Pt-Cu/C Cathode. *Catalysts*, *9*(6), 544.

[39] Rotondo, D., Nejjari, F., & Puig, V. (2016). Fault tolerant control of a proton exchange membrane fuel cell using Takagi–Sugeno virtual actuators. *Journal of Process Control*, *45*, 12-29.

[40] Pettersson, J., Ramsey, B., & Harrison, D. (2006). A review of the latest developments in electrodes for unitised regenerative polymer electrolyte fuel cells. *Journal of Power Sources*, *157*(1), 28-34.

[41] Li, C., Liu, Y., Xu, B., & Ma, Z. (2019). Finite Time Thermodynamic Optimization of an Irreversible Proton Exchange Membrane Fuel Cell for Vehicle Use. *Processes*, *7*(7), 419.

[42] Basu, S. U. D. D. H. A. S. A. T. W. A. (2015, September). Proton exchange membrane fuel cell technology: india's perspective. In *Proc Indian Natl Sci Acad* (Vol. 81, pp. 865-890).

[43] Bhattacharya, P. K. (2015). Water flooding in the proton exchange membrane fuel cell. *Directions*, *15*(1).

[44] Igbal, M. Z. M., Rosli, M. I., & Panuh, D. (2018). Performance Investigation of High-Temperature Proton Exchange Membrane Fuel Cell. *JURNAL KEJURUTERAAN*, *1*(4), 1-6.

[45] Benyoucef, D. (2011). *Modélisation particulaire et multidimensionnelle des décharges hors équilibre à basse pression excitées par champs électromagnétiques* (Doctoral dissertation, Université de Toulouse, Université Toulouse III-Paul Sabatier).

[46] Lin, Y. H., & Adomaitis, R. A. (2001). Simulation and model reduction methods for an RF plasma glow discharge. *Journal of computational physics*, *171*(2), 731-752.

[47] Kline, L. E., Partlow, W. D., Young, R. M., Mitchell, R. R., & Congedo, T. V. (1991). Diagnostics and modeling of RF discharge dissociation in N/sub 2/O. *IEEE Transactions on Plasma Science*, *19*(2), 278-285.

[48] Graves, D. B., & Jensen, K. F. (1986). A continuum model of DC and RF discharges. *IEEE Transactions on plasma science*, *14*(2), 78-91.

[49] Lieberman, M. A., Lichtenberg, A. J., & Savas, S. E. (1991). Model of magnetically enhanced, capacitive RF discharges. *IEEE Transactions on Plasma Science*, *19*(2), 189-196.

[50] Samir, T., Liu, Y., & Zhao, L. (2018). Study on effect of neutral gas pressure on plasma characteristics in capacitive RF argon glow discharges at low pressure by fluid modeling. *IEEE Transactions on Plasma Science*, *46*(5), 1738-1746.

[51] Benyoucef, D., Yousfi, M., & Belmadani, B. (2011). Self-consistent particle modeling of radio frequency discharge in Ar/O2 mixtures: Effects of crossed electric and magnetic fields and partial pressure. *Journal of Applied Physics*, *109*(8), 083304.

[52] Benyoucef, D., Yousfi, M., Belmadani, B., & Settaouti, A. (2010). PIC MC using free path for the simulation of low-pressure RF discharge in argon. *IEEE Transactions on plasma science*, *38*(4), 902-908.

[53] Benyoucef, D., Yousfi, M., & Belmadani, B. (2012). Particle-in-cell Monte Carlo simulation using free path method for radio frequency argon discharge modelling: Comparison with experiment. *International Journal of Physical Sciences*, *7*(33), 5256-5265.

[54] Benyoucef, D., & Yousfi, M. (2013). Effects of Increasing Magnetic Field and Decreasing Pressure on Asymmetric Magnetron Radio Frequency Ar/O2 Discharges. *IEEE Transactions on Plasma Science*, *41*(4), 829-838.

[55] Benyoucef, D., & Yousfi, M. (2014). Particle modelling of low-pressure radio-frequency magnetron discharges including the effects of self-induced electromagnetic fields. *Plasma Sources Science and Technology*, *23*(4), 044007.

[56] Benyoucef, D., & Yousfi, M. (2015). Particle modelling of magnetically confined oxygen plasma in low pressure radio frequency discharge. *Physics of Plasmas*, *22*(1), 013510.

[57] Richards, A. D., Thompson, B. E., & Sawin, H. H. (1987). Continuum modeling of argon radio frequency glow discharges. *Applied physics letters*, *50*(9), 492-494.

[58] Goedheer, W. J., & Meijer, P. M. (1993). Numerical simulation of RF discharges for plasma processing. *Journal of nuclear materials*, *200*(3), 282-290.

[59] Sommerer, T. J., & Kushner, M. J. (1992). Numerical investigation of the kinetics and chemistry of rf glow discharge plasmas sustained in He, N2, O2, He/N2/O2, He/CF4/O2, and SiH4/NH3 using a Monte Carlo-fluid hybrid model. *Journal of applied physics*, *71*(4), 1654-1673.

[60] Vahedi, V., Surendra, M. (1995). A Monte Carlo collision model for the particle-in-cell method: applications to argon and oxygen discharges. *Computer Physics Communications*, *87*(1-2), 179-198.

[61] Kuppermann, A., & Greene, E. F. (1968). Chemical reaction cross sections and rate constants. Journal of Chemical Education, 45(6), 361.

[62] Liu, X., & Shemansky, D. E. (2006). Analysis of electron impact ionization properties of methane. *Journal of Geophysical Research: Space Physics*, *111*(A4).

[63] Danko,M. Orszagh, M J. Ďurian, M. Kočišek, J. Daxner,M. Zöttl, S. Maljković, J B. Fedor, J. Scheier, P. Denifl, S. and Matejčík, Š. (2013). Electron impact excitation of methane: determination of appearance energies for dissociation products. *Journal of Physics B: Atomic, Molecular and Optical Physics*, *46*(4), 045203.

[64] Nikitović, Ž., Šašić, O., Petrović, Z. L., Malović, G. N., Strinić, A., Dujko, S., Raspopović, Z and Radmilović-Radjenović, M. (2004). Data bases for modeling plasma devices for processing of integrated circuits. In *Materials Science Forum* (Vol. 453, pp. 15-20). Trans Tech Publications.

[65] Wei, B., Chen, Z., Wang, X., Lu, D., Lin, S., Hutton, R., & Zou, Y. (2013). The relative cross section and kinetic energy distribution of dissociation processes of methane by electron impact. *Journal of Physics B: Atomic, Molecular and Optical Physics*, *46*(21), 215205.

[66] Haresnape, J. N., Stevels, J. M., & Warhurst, E. (1940). The rate of reaction of sodium atoms with polyhalogenated methane derivatives. *Transactions of the Faraday Society*, *35*, 465-472.

[67] Longmier, B. W., Gallimore, A. D., & Hershkowitz, N. (2012). Hydrogen production from methane using an RF plasma source in total nonambipolar flow. *Plasma Sources Science and Technology*, *21*(1), 015007.

[68] Rawat, P., Prabhudesai, V. S., Rahman, M. A., Ram, N. B., & Krishnakumar, E. (2008). Absolute cross sections for dissociative electron attachment to NH3 and CH4. *International Journal of Mass Spectrometry*, *277*(1-3), 96-102.

[69] Cooper, G., Christensen, E., & Hitchcock, A. P. (2007). Quasielastic electron scattering from methane, methane-d4, methane-d2, ethylene, and 2-methylpropane. *The Journal of chemical physics*, *127*(8), 084315.

[70] Makochekanwa, C., Oguri, K., Suzuki, R., Ishihara, T., Hoshino, M., Kimura, M., & Tanaka, H. (2006). Experimental observation of neutral radical formation from CH 4 by electron impact in the threshold region. *Physical Review A*, *74*(4), 042704.

[71] Erwin, D. A., & Kunc, J. A. (2005). Electron-impact dissociation of the methane molecule into neutral fragments. *Physical Review A*, *72*(5), 052719.

[72] Mishra, L. N., Shibata, K., Ito, H., Yugami, N., & Nishida, Y. (2004). Characteristics of methane destruction using a pulsed corona discharge at atmospheric pressure. *J. Plasma Fusion Res.*, *6*, 760-763.

[73] Marcum, S. D., Parish, J. W., & Ganguly, B. N. (2004). Methane dissociation in pulsed dc discharges at high reduced electric field. *Journal of propulsion and power*, *20*(2), 360-368.

[74] Gluch, K., Scheier, P., Schustereder, W., Tepnual, T., Feketeova, L., Mair, C., Stamatovic, L. & Märk, T. D. (2003). Cross sections and ion kinetic energies for electron impact ionization of CH4. *International Journal of Mass Spectrometry*, *228*(2-3), 307-320.

[75] Geleijns, M., van der Avoird, A., Wormer, P. E., & Halberstadt, N. (2002). Photodissociation of the methane–argon complex. II. Vibrational predissociation dynamics, spectral linewidths and fragment state distributions. *The Journal of chemical physics*, *117*(16), 7562-7574.

[76] Ziółkowski, M., Vikár, A., Mayes, M. L., Bencsura, Á., Lendvay, G., & Schatz, G. C. (2012). Modeling the electron-impact dissociation of methane. *The Journal of chemical physics*, *137*(22), 22A510.

[77] Indarto, A., Coowanitwong, N., Choi, J. W., Lee, H., & Song, H. K. (2008). Kinetic modeling of plasma methane conversion in a dielectric barrier discharge. *Fuel Processing Technology*, *89*(2), 214-219.

[78] Herrebout, D., Bogaerts, A., Yan, M., Gijbels, R., Goedheer, W., & Vanhulsel, A. (2002). Modeling of a capacitively coupled radio-frequency methane plasma: Comparison between a one-dimensional and a two-dimensional fluid model. *Journal of applied physics*, *92*(5), 2290-2295.

[79] Herrebout, D., Bogaerts, A., Yan, M., Gijbels, R., Goedheer, W., & Dekempeneer, E. (2001). One-dimensional fluid model for an rf methane plasma of interest in deposition of diamond-like carbon layers. *Journal of Applied Physics*, *90*(2), 570-579.

[80] Nagayama, K., Farouk, B., & Lee, Y. H. (1998). Particle simulation of radio-frequency plasma discharges of methane for carbon film deposition. *IEEE transactions on plasma science*, *26*(2), 125-134.

[81] Masi, M., Cavallotti, C., & Carra, S. (1998). Different approaches for methane plasmas modeling. *Chemical engineering science*, *53*(22), 3875-3886.

[82] Gogolides, E., Buteau, C., Rhallabi, A., & Turban, G. (1994). Radio-frequency glow discharges in methane gas: modelling of the gas-phase physics and chemistry. *Journal of Physics D: Applied Physics*, *27*(4), 818.

[83] Rhallabi, A., & Catherine, Y. (1991). Computer simulation of a carbon-deposition plasma in CH_4. *IEEE Transactions on plasma science*, *19*(2), 270-277.

[84] Matyash, K., Schneider, R., Bergmann, A., Jacob, W., Fantz, U., & Pecher, P. (2003). Modeling of hydrocarbon species in ECR methane plasmas. *Journal of nuclear materials*, *313*, 434-438.

[85] Chang, C. W., Davoudabadi, M., & Mashayek, F. (2010). One-dimensional fluid model of methane plasma for diamond-like coating. *IEEE Transactions on Plasma Science*, *38*(7), 1603-1614.

[86] Tachibana, K., Nishida, M., Harima, H., & Urano, Y. (1984). Diagnostics and modelling of a methane plasma used in the chemical vapour deposition of amorphous carbon films. *Journal of Physics D: Applied Physics*, *17*(8), 1727.

[87] Snoeckx, R., Setareh, M., Aerts, R., Simon, P., Maghari, A., & Bogaerts, A. (2013). Influence of N2 concentration in a CH4/N2 dielectric barrier discharge used for CH4 conversion into H2. *International Journal of Hydrogen Energy*, *38*(36), 16098-16120.

[88] Richley, J. C., Fox, O. J., Ashfold, M. N., & Mankelevich, Y. A. (2011). Combined experimental and modeling studies of microwave activated CH4/H2/Ar plasmas for microcrystalline, nanocrystalline, and ultrananocrystalline diamond deposition. *Journal of Applied Physics*, *109*(6), 063307.

[89] Takita, K., Shishido, K., & Kurumada, K. (2011). Ignition in a supersonic flow by a plasma jet of mixed feedstock including CH4. Proceedings of the Combustion Institute, 33(2), 2383-2389.

[90] Alcouffe, G., Cavarroc, M., Cernogora, G., Ouni, F., Jolly, A., Boufendi, L., & Szopa, C. (2009). Capacitively coupled plasma used to simulate Titan's atmospheric chemistry. Plasma Sources Science and Technology, 19(1), 015008.

[91] Möller, I., Serdyuchenko, A., & Soltwisch, H. (2006). Analysis of the chemistry in CH4/O2 plasmas by means of absorption spectroscopy and a simple numerical model. Journal of applied physics, 100(3), 033302.

[92] Sebastian, A. A., & Wadehra, J. M. (2005). Time-dependent behaviour of electron transport in methane–argon mixtures. *Journal of Physics D: Applied Physics*, *38*(10), 1577.

[93] Yoon, S. F., Tan, K. H., Rusli, & Ahn, J. (2002). Modeling and analysis of hydrogen–methane plasma in electron cyclotron resonance chemical vapor deposition of diamond-like carbon. *Journal of applied physics*, *91*(1), 40-47.

[94] Farouk, B., & Nagayama, K. (2001, August). Particle simulation of CH_4/H_2 RF glow discharges for DLC film deposition. In *AIP Conference Proceedings* (Vol. 585, No. 1, pp. 230-237). AIP.

[95] Gordillo-Vázquez, F. J., Gómez-Aleixandre, C., & Albella, J. M. (2001). Influence of the excitation frequency on $CH_4/H/H_2$ plasmas for diamond film deposition: electron energy distribution function and atomic hydrogen concentration. *Plasma Sources Science and Technology*, *10*(1), 99.

[96] Tahara, H., Minami, K. I., Murai, A., Yasui, T., & Yoshikawa, T. (1995). Diagnostic experiment and kinetic model analysis of microwave CH4/H2 plasmas for deposition of diamondlike carbon films. *Japanese journal of applied physics*, *34*(4R), 1972.

[97] Duncan, C. W., & Walker, I. C. (1972). Collision cross-sections for low energy electrons in methane. *Journal of the Chemical Society, Faraday Transactions 2: Molecular and Chemical Physics*, *68*, 1514-1521.

[98] Winters, H. F. (1975). Dissociation of methane by electron impact. *The Journal of Chemical Physics*, *63*(8), 3462-3466.

[99] Jones, R. K. (1985). Absolute total cross section for the scattering of low energy electrons by methanea. *The Journal of chemical physics*, *82*(12), 5424-5427.

[100] Haddad, G. N. (1985). Low energy electron collision cross sections for methane. *Australian journal of physics*, *38*(5), 677-686.

[101] Davies, D. K., Kline, L. E., & Bies, W. E. (1989). Measurements of swarm parameters and derived electron collision cross sections in methane. *Journal of Applied physics*, *65*(9), 3311-3323.

[102] Schmidt, B. (1991). Anisotropic low energy electron collision cross sections for methane derived from transport coefficients. *Journal of Physics B: Atomic, Molecular and Optical Physics*, *24*(22), 4809.

[103] Nakano, T., Toyoda, H., & Sugai, H. (1991). Electron-impact dissociation of methane into CH_3 and CH_2 radicals I. Relative cross sections. *Japanese journal of applied physics*, *30*(11R), 2908.

[104] Gogolides, E., Mary, D., Rhallabi, A., & Turban, G. (1995). RF plasmas in methane: Prediction of plasma properties and neutral radical densities with combined gas-phase physics and chemistry model. *Japanese journal of applied physics*, *34*(1R), 261.

[105] Song, M. Y., Yoon, J. S., Cho, H., Itikawa, Y., Karwasz, G. P., Kokoouline, V., Nakamura, Y. & Tennyson, J. (2015). Cross sections for electron collisions with methane. *Journal of Physical and Chemical Reference Data*, *44*(2), 023101.

[106] Korolov, I., Vass, M., & Donkó, Z. (2016). Scanning drift tube measurements of electron transport parameters in different gases: argon, synthetic air, methane and deuterium. *Journal of Physics D: Applied Physics*, *49*(41), 415203.

[107] Joshipura, K. N., Vinodkumar, M., Limbachiya, C. G., & Antony, B. K. (2004). Calculated total cross sections of electron-impact ionization and excitations in tetrahedral (X Y 4) and SF 6 molecules. *Physical Review A*, *69*(2), 022705.

[108] Goto, N., & Makabe, T. (1990). Time-dependent electron swarm parameters in RF fields in CH4 and H2. *Journal of Physics D: Applied Physics*, *23*(6), 686.

[109] Hunter, S. R., Carter, J. G., & Christophorou, L. G. (1986). Electron transport measurements in methane using an improved pulsed Townsend technique. *Journal of applied physics*, *60*(1), 24-35.

[110] Vuškovic, L., & Trajmar, S. (1983). Electron impact excitation of methane. *The Journal of Chemical Physics*, *78*(8), 4947-4951.

[111] Winstead, C., Sun, Q., McKoy, V., Lino, J. L., & Lima, M. A. (1993). Electronic excitation of CH_4 by low-energy electron impact. *The Journal of chemical physics*, *98*(3), 2132-2137.

[112] Bagnasco, C., Kondo, Y., & Nakahara, M. (2014). Efficient entanglement operator for a multi-qubit system. *Physica Scripta*, *89*(8), 085102.

[113] Makochekanwa, C., Hoshino, M., Tanaka, H., & Kimura, M. (2007). Electron-Impact Induced Neutral Radical Fragmentation of CH4. In *Journal of Physics: Conference Series* (Vol. 86, No. 1, p. 012004). IOP Publishing.

[114] Erwin, D. A., & Kunc, J. A. (2008). Dissociation and ionization of the methane molecule by nonrelativistic electrons including the near threshold region. *Journal of Applied Physics*, *103*(6), 064906.

[115] Gil, T. J., Lengsfield, B. H., McCurdy, C. W., & Rescigno, T. N. (1994). Ab initio complex Kohn calculations of dissociative excitation of methane: Close-coupling convergence studies. *Physical Review A*, *49*(4), 2551.

[116] Janev, R. K., & Reiter, D. (2002). *Collision processes of hydrocarbon species in hydrogen plasmas: I. The methane family*. Forschungszentrum Jülich, Zentralbibliothek.

[117] Sohn, W., Jung, K., & Ehrhardt, H. (1983). Threshold structures in the cross sections of low-energy electron scattering of methane. *Journal of Physics B: Atomic and Molecular Physics*, *16*(5), 891.

[118] Cho, H., Park, Y. S., y Castro, E. A., De Souza, G. L. C., Iga, I., Machado, L. E., Brescansin, L,M & Lee, M. T. (2008). A comparative experimental–theoretical study on elastic electron scattering by methane. *Journal of Physics B: Atomic, Molecular and Optical Physics*, *41*(4), 045203.

[119] Boesten, L., & Tanaka, H. (1991). Elastic DCS for e+ CH4 collisions, 1.5-100 eV. *Journal of Physics B: Atomic, Molecular and Optical Physics*, *24*(4), 821.

[120] Sakae, T., Sumiyoshi, S., Murakami, E., Matsumoto, Y., Ishibashi, K., & Katase, A. (1989). Scattering of electrons by CH4, CF4 and SF6 in the 75-700 eV range. *Journal of Physics B: Atomic, Molecular and Optical Physics*, *22*(9), 1385.

[121] Sohn, W., Kochem, K. H., Scheuerlein, K. M., Jung, K., & Ehrhardt, H. (1986). Elastic electron scattering from CH_4 for collision energies between 0.2 and 5 eV. *Journal of Physics B: Atomic and Molecular Physics*, *19*(21), 3625.

[122] Iga, I., Lee, M. T., Homem, M. G. P., Machado, L. E., & Brescansin, L. M. (2000). Elastic cross sections for e− CH_4 collisions at intermediate energies. *Physical Review A*, *61*(2), 022708.

[123] Tanaka, H., Okada, T., Boesten, L., Suzuki, T., Yamamoto, T., & Kubo, M. (1982). Differential cross sections for elastic scattering of electrons by CH_4 in the energy range of 3 to 20 eV. *Journal of Physics B: Atomic and Molecular Physics*, *15*(18), 3305.

[124] Shyn, T. W., & Cravens, T. E. (1990). Angular distribution of electrons elastically scattered from CH_4. *Journal of Physics B: Atomic, Molecular and Optical Physics*, *23*(2), 293.

[125] Bundschu, C. T., Gibson, J. C., Gulley, R. J., Brunger, M. J., Buckman, S. J., Sanna, N., & Gianturco, F. A. (1997). Low-energy electron scattering from methane. *Journal of Physics B: Atomic, Molecular and Optical Physics*, *30*(9), 2239.

[126] Shyn, T. W. (1991). Vibrational excitation cross sections of methane by electron impact. *Journal of Physics B: Atomic, Molecular and Optical Physics*, *24*(24), 5169.

[127] Tanaka, H., Kubo, M., Onodera, N., & Suzuki, A. (1983). Vibrational excitation of CH4 by electron impact: 3-20 eV. *Journal of Physics B: Atomic and Molecular Physics*, *16*(15), 2861.

[128] Gan, L., & Cravens, T. E. (1992). Electron impact cross-sections and cooling rates for methane. *Planetary and space science*, *40*(11), 1535-1544.

[129] Čurík, R., Čársky, P., & Allan, M. (2008). Vibrational excitation of methane by slow electrons revisited: theoretical and experimental study. *Journal of Physics B: Atomic, Molecular and Optical Physics*, *41*(11), 115203.

[130] Straub, H. C., Lin, D., Lindsay, B. G., Smith, K. A., & Stebbings, R. F. (1997). Absolute partial cross sections for electron-impact ionization of CH4 from threshold to 1000 eV. *The Journal of chemical physics*, *106*(11), 4430-4435.

[131] Rapp, D., & Englander-Golden, P. (1965). Total cross sections for ionization and attachment in gases by electron impact. I. Positive ionization. *The Journal of Chemical Physics*, *43*(5), 1464-1479.

[132] Feagin, J. M. (1984). Wannier threshold theory for the Coulomb break-up of three-particle systems. *Journal of Physics B: Atomic and Molecular Physics*, *17*(12), 2433.

[133] Melton, C. E., & Rudolph, P. S. (1967). Radiolysis of Methane in a Wide-Range Radiolysis Source of a Mass Spectrometer. I. Individual and Total Cross Sections for the Production of Positive Ions, Negative Ions, and Free Radicals by Electrons. *The Journal of Chemical Physics*, *47*(5), 1771-1774.

[134] Schmidt, B., & Roncossek, M. (1992). Drift velocity, longitudinal and transverse diffusion in hydrocarbons derived from distributions of single electrons. *Australian journal of physics*, *45*(3), 351-364.

[135] Cochran, L. W., & Forester, D. W. (1962). Diffusion of slow electrons in gases. *Physical Review*, *126*(5), 1785.

[136] Millican, P. G., & Walker, I. C. (1987). Electron swarm characteristic energies (Dr/μ) in methane, perdeuteromethane, silane, perdeuterosilane, phosphine and hydrogen sulphide at low E/N. *Journal of Physics D: Applied Physics*, *20*(2), 193.

[137] Lakshminarasimha, C. S., & Lucas, J. (1977). The ratio of radial diffusion coefficient to mobility for electrons in helium, argon, air, methane and nitric oxide. *Journal of Physics D: Applied Physics*, *10*(3), 313.

[138] Heylen, A. E. D. (1968). Ionization coefficients and sparking voltages in argon-methane and argon-propane mixtures. *INTERNATIONAL JOURNAL OF ELECTRONICS*, *24*(2), 165-175.

[139] De Urquijo, J., Alvarez, I., Basurto, E., & Cisneros, C. (1999). Measurement of ionization and electron transport in methane-argon mixtures. *Journal of Physics D: Applied Physics*, *32*(14), 1646.

[140] Lieberman, M. A., & Lichtenberg, A. J. (2005). *Principles of plasma discharges and materials processing*. John Wiley & Sons.

[141] Chabert, P., & Braithwaite, N. (2011). *Physics of radio-frequency plasmas*. Cambridge University Press.

[142] Wilczek, S., Trieschmann, J., Schulze, J., Schuengel, E., Brinkmann, R. P., Derzsi, A., & Mussenbrock, T. (2015). The effect of the driving frequency on the confinement of beam electrons and plasma density in low-pressure capacitive discharges. *Plasma Sources Science and Technology*, *24*(2), 024002.

[143] Bi, Z. H., Liu, Y. X., Jiang, W., Xu, X., & Wang, Y. N. (2011). A brief review of dual-frequency capacitively coupled discharges. *Current Applied Physics*, *11*(5), S2-S8.

[144] Schulze, J., Donko, Z., Derzsi, A., Korolov, I., & Schuengel, E. (2014). The effect of ambipolar electric fields on the electron heating in capacitive RF plasmas. *Plasma Sources Science and Technology*, *24*(1), 015019.

[145] Liu, D. W., Iza, F., & Kong, M. G. (2008). Electron heating in radio-frequency capacitively coupled atmospheric-pressure plasmas. *Applied Physics Letters*, *93*(26), 261503.

[146] Ahn, S. K., You, S. J., & Chang, H. Y. (2006). Driving frequency effect on the electron energy distribution function in capacitive discharge under constant discharge power condition. *Applied physics letters*, *89*(16), 161506.

[147] Schulze, J., Schüngel, E., Donkó, Z., & Czarnetzki, U. (2011). The electrical asymmetry effect in multi-frequency capacitively coupled radio frequency discharges. *Plasma Sources Science and Technology*, *20*(1), 015017.

[148] Zhang, G. F., Reuter, S., & Buck, V. (2005). Deposition of hard carbon coatings using combined inductively and capacitively coupled plasma sources. *Surface and Coatings Technology*, *190*(1), 54-59.

[149] Van Laer, K., & Bogaerts, A. (2015). Fluid modelling of a packed bed dielectric barrier discharge plasma reactor. *Plasma Sources Science and Technology*, *25*(1), 015002.

[150] Zhang, Y. R., Gao, F., Li, X. C., Bogaerts, A., & Wang, Y. N. (2015). Fluid simulation of the bias effect in inductive/capacitive discharges. *Journal of Vacuum Science & Technology A: Vacuum, Surfaces, and Films*, *33*(6), 061303.

[151] Leszczynski, S., Strobel, C., Albert, M., Bartha, J. W., & Stephan, U. (2014, May). Influence of the excitation frequency increase on a fluid model of the capacitively coupled argon plasma. In *2014 IEEE 41st International Conference on Plasma Sciences (ICOPS)*

held with 2014 IEEE International Conference on High-Power Particle Beams (BEAMS) (pp. 1-6). IEEE.

[152] Rafatov, I., Bogdanov, E. A., & Kudryavtsev, A. A. (2012). Account of nonlocal ionization by fast electrons in the fluid models of a direct current glow discharge. *Physics of Plasmas*, *19*(9), 093503.

[153] Rafatov, I., Bogdanov, E. A., & Kudryavtsev, A. A. (2012). On the accuracy and reliability of different fluid models of the direct current glow discharge. *Physics of Plasmas*, *19*(3), 033502.

[154] Lu, Y. J., Yan, D. Q., & Chen, Y. S. (2009). 2-D fluid simulation of dual-frequency capacitively coupled plasma. *Journal of Hydrodynamics, Ser. B*, *21*(6), 814-819.

[155] Kim, H. C., Iza, F., Yang, S. S., Radmilović-Radjenović, M., & Lee, J. K. (2005). Particle and fluid simulations of low-temperature plasma discharges: benchmarks and kinetic effects. *Journal of Physics D: Applied Physics*, *38*(19), R283.

[156] Chen, G., & Raja, L. L. (2004). Fluid modeling of electron heating in low-pressure, high-frequency capacitively coupled plasma discharges. *Journal of applied physics*, *96*(11), 6073-6081.

[157] Maddison, G. P., Helander, P., & Cornford, S. L. (1998). Fluid modelling of edge plasmas with ion frictional forces allowing for arbitrary impurity abundances. *Contributions to Plasma Physics*, *38*(1-2), 254-259.

[158] Chang, C. W., Davoudabadi, M., & Mashayek, F. (2010). One-dimensional fluid model of methane plasma for diamond-like coating. *IEEE Transactions on Plasma Science*, *38*(7), 1603-1614.

[159] Nagayama, K., Farouk, B., & Lee, Y. H. (1998). Particle simulation of radio-frequency plasma discharges of methane for carbon film deposition. *IEEE transactions on plasma science*, *26*(2), 125-134.

[160] Baranov, O., Bazaka, K., Kersten, H., Keidar, M., Cvelbar, U., Xu, S., & Levchenko, I. (2017). Plasma under control: Advanced solutions and perspectives for plasma flux management in material treatment and nanosynthesis. Applied Physics Reviews, 4(4), 041302.

[161] Bogaerts, A., Neyts, E., Gijbels, R., & van der Mullen, J. (2002). Gas discharge plasmas and their applications. Spectrochimica Acta Part B: Atomic Spectroscopy, 57(4), 609-658.

[162]Jaritz, M., Hopmann, C., Behm, H., Kirchheim, D., Wilski, S., Grochla, D., Wilski, S. Grochla, D. Banko, L. Ludwig, A. Boke, M. Winter, J. Bahre, H. And Dahlman, R. (2017). Influence of residual stress on the adhesion and surface morphology of PECVD-coated polypropylene. Journal of Physics D: Applied Physics, 50(44), 445301.

[163] Dobbyn, K. (2000). Design and application of a plasma impedance monitor for RF plasma diagnostics (Doctoral dissertation, Dublin City University).

[164] Benedikt, J. (2010). Plasma-chemical reactions: low pressure acetylene plasmas. Journal of Physics D: Applied Physics, 43(4), 043001.

[165] Tanışlı, M., Şahin, N., & Demir, S. (2017). An investigation on optical properties of capacitive coupled radio-frequency mixture plasma with Langmuir probe. Optik, 142, 153-162.

[166] Chung, T. H., Yoon, H. S., & Lee, J. K. (1995). Scaling laws verification for capacitive rf-discharge Ar plasma using particle-in-cell simulations. Journal of applied physics, 78(11), 6441-6447.

[167] Park, S., Choe, W., & Kim, H. (2018). Electron heating in rf capacitive discharges at atmospheric-to-subatmospheric pressures. Scientific reports, 8(1), 10217.

[168] Schüngel, E., Zhang, Q. Z., Iwashita, S., Schulze, J., Hou, L. J., Wang, Y. N., & Czarnetzki, U. (2011). Control of plasma properties in capacitively coupled oxygen discharges via the electrical asymmetry effect. Journal of Physics D: Applied Physics, 44(28), 285205.

[169] You, S. J., Bai, K. H., Chae, S. H., & Chang, H. Y. (2005). Control of electron density and temperature with a modified capacitive discharge. Plasma chemistry and plasma processing, 25(3), 245-254.

[170] Raizer, Y. P., Shneider, M. N., & Yatsenko, N. A. (2017). Radio-frequency capacitive discharges. CRC Press.

[171] Tanişli, M., Şahin, N., & Demir, S. (2017). Electrical characteristics for capacitively coupled radio frequency discharges of helium and neon. *Pramana*, *89*(3), 36.

[172] Kechkar, S. (2015). *Experimental investigation of a low pressure capacitively-coupled discharge* (Doctoral dissertation, Dublin City University).

[173] He, X., Liu, C., & Zhang, Y. (2017). Diagnostic of capacitively coupled radio frequency plasma from electrical discharge characteristics: comparison with optical emission spectroscopy and fluid model simulation. *Plasma Science and Technology*, *20*(2), 24005-024005.

[174] Shihab, M. (2018). Non-linear lumped model circuit of capacitively coupled plasmas at the intermediate radio-frequencies. *Physics Letters A*, *382*(24), 1609-1614.

[175] Lee, J. K., Babaeva, N. Y., Kim, H. C., Manuilenko, O. V., & Shon, J. W. (2004). Simulation of capacitively coupled single-and dual-frequency RF discharges. *IEEE Transactions on Plasma Science*, *32*(1), 47-53.

[176] Alcouffe, G., Cavarroc, M., Cernogora, G., Ouni, F., Jolly, A., Boufendi, L., & Szopa, C. (2009). Capacitively coupled plasma used to simulate Titan's atmospheric chemistry. *Plasma Sources Science and Technology*, *19*(1), 015008.

[177] Saikia, P., Bhuyan, H., Escalona, M., Favre, M., Rawat, R. S., & Wyndham, E. (2018). A nonlinear global model of single frequency capacitively coupled plasma and its experimental validation. *AIP Advances*, *8*(4), 045113.

[178] Lymberopoulos, D. P., & Economou, D. J. (1995). Two-dimensional self-consistent radio frequency plasma simulations relevant to the gaseous electronics conference RF reference cell. *Journal of research of the National Institute of Standards and Technology*, *100*(4), 473.

[179] Schüngel, E., Zhang, Q. Z., Iwashita, S., Schulze, J., Hou, L. J., Wang, Y. N., & Czarnetzki, U. (2011). Control of plasma properties in capacitively coupled oxygen discharges via the electrical asymmetry effect. *Journal of Physics D: Applied Physics*, *44*(28), 285205.

[180] Gadoum, A., & Benyoucef, D. (2018). Set of the Electron Collision Cross Sections for Methane Molecule. *IEEE Transactions on Plasma Science*, *47*(3), 1505-1513.

[182] http://kida.obs.u-bordeaux1.fr/search.html

[183] http://udfa.ajmarkwick.net/index.php

[184] http://kinetics.nist.gov/kinetics/

[185] Mao, M., & Bogaerts, A. (2010). Investigating the plasma chemistry for the synthesis of carbon nanotubes/nanofibres in an inductively coupled plasma enhanced CVD system: the effect of different gas mixtures. *Journal of Physics D: Applied Physics*, *43*(20), 205201.

[186] Huntress Jr, W. T. (1977). Laboratory studies of bimolecular reactions of positive ions in interstellar clouds, in comets, and in planetary atmospheres of reducing composition. *The Astrophysical Journal Supplement Series*, *33*, 495-514.

[188] Huang, C. Y., Liang, M. W., Chang, C. H., Lee, K. F., & Wang, C. C. (2009, June). Simulation study of a capacitively coupled plasma by two dimensional fluid model. In *2009 IEEE International Conference on Plasma Science-Abstracts* (pp. 1-1). IEEE.

[189] Bera, K., Rauf, S., & Collins, K. (2011). Plasma Dynamics in Low-Pressure Capacitively Coupled Oxygen Plasma Using PIC–MCC/Fluid Hybrid Model. *IEEE Transactions on Plasma Science*, *39*(11), 2576-2577.

[190] Kim, H. J., & Lee, H. J. (2016). 2D fluid model analysis for the effect of 3D gas flow on a capacitively coupled plasma deposition reactor. *Plasma Sources Science and Technology*, *25*(3), 035006.

[191] Alves, L. L., & Marques, L. (2012). Fluid modelling of capacitively coupled radio-frequency discharges: a review. *Plasma Physics and Controlled Fusion*, *54*(12), 124012.

[192] Gul, B., & Aman-ur-Rehman. (2015). A comparative study of capacitively coupled HBr/He, HBr/Ar plasmas for etching applications: Numerical investigation by fluid model. *Physics of Plasmas*, *22*(10), 103520.

[193] Lee, H. C. (2018). Review of inductively coupled plasmas: Nano-applications and bistable hysteresis physics. *Applied Physics Reviews*, *5*(1), 011108.

[194] Godyak, V. A. (2011). Electrical and plasma parameters of ICP with high coupling efficiency. *Plasma Sources Science and Technology*, *20*(2), 025004.

[195] Wu, C., Wang, J., Zhang, W., & Luo, Y. (2015). Modeling and simulation of ion-filtered inductively coupled plasma using argon plasma. *Japanese Journal of Applied Physics*, *54*(3), 036101.

[196] Kortshagen, U., & Heil, B. G. (1999). Kinetic two-dimensional modeling of inductively coupled plasmas based on a hybrid kinetic approach. *IEEE transactions on plasma science*, *27*(5), 1297-1309.

[197] Yoon, N. S., You, K. I., & Hwang, S. M. (1999). A self-consistent modeling and simulation of transformer coupled plasma discharge. *Surface and Coatings Technology*, *112*(1-3), 34-37.

[198] Kim, Y., Kim, H. U., Shin, Y., Kang, S., & Kim, T. (2014). Modeling of silicon nanoparticle formation in inductively coupled plasma using a modified collision frequency function. *Journal of Mechanical Science and Technology*, *28*(11), 4693-4703.

[199] Wu, H. M., Yu, B. W., Krishnan, A., Li, M., Yang, Y., Yan, J. P., & Yuan, D. P. (1997). Theoretical and experimental studies of the bell-jar-top inductively coupled plasma. *IEEE transactions on plasma science*, *25*(4), 776-785.

[200] Hash, D. B., Bose, D., Rao, M. V. V. S., Cruden, B. A., Meyyappan, M., & Sharma, S. P. (2001). Impact of gas heating in inductively coupled plasmas. *Journal of Applied Physics*, *90*(5), 2148-2157.

[201] Scheubert, P., Awakowicz, P., Schwefel, R., & Wachutka, G. (2001). Fluid dynamic modelling and experimental diagnostics of an inductive high density plasma source (ICP). *Surface and Coatings Technology*, *142*, 526-530.

[202] Yasuda, H., Morosoff, N., Brandt, E. S., & Reilley, C. N. (1979). Plasma polymerization of tetrafluoroethylene. I. Inductive radio frequency discharge. *Journal of Applied Polymer Science*, *23*(4), 1003-1011.

[203] Singh, H., Coburn, J. W., & Graves, D. B. (2001). Measurements of neutral and ion composition, neutral temperature, and electron energy distribution function in a CF 4

inductively coupled plasma. *Journal of Vacuum Science & Technology A: Vacuum, Surfaces, and Films*, *19*(3), 718-729.

[204] Singh, H., & Graves, D. B. (2000). Measurements of the electron energy distribution function in molecular gases in a shielded inductively coupled plasma. *Journal of Applied Physics*, *88*(7), 3889-3898.

[205] Watters, R. L., Carroll, R. J., & Spiegelman, C. H. (1987). Error modeling and confidence interval estimation for inductively coupled plasma calibration curves. *Analytical Chemistry*, *59*(13), 1639-1643.

[206] Suekane, T., Taya, T., Okuno, Y., & Kabashima, S. (1996). Numerical studies on the nonequilibrium inductively coupled plasma with metal vapor ionization. *IEEE transactions on plasma science*, *24*(3), 1147-1154.

[207] Colpo, P., Ernst, R., & Rossi, F. (1999). Determination of the equivalent circuit of inductively coupled plasma sources. *Journal of applied physics*, *85*(3), 1366-1371.

[208] Bera, K., Farouk, B., & Vitello, P. (2001). Inductively coupled radio frequency methane plasma simulation. *Journal of Physics D: Applied Physics*, *34*(10), 1479.

[209] Turkoz, E., & Celik, M. (2013). 2-D electromagnetic and fluid models for inductively coupled plasma for RF ion thruster performance evaluation. *IEEE Transactions on Plasma Science*, *42*(1), 235-240.

[210] Turkoz, E., & Celik, M. (2013). 2-D electromagnetic and fluid models for inductively coupled plasma for RF ion thruster performance evaluation. *IEEE Transactions on Plasma Science*, *42*(1), 235-240.

[211] Lallement, L., Rhallabi, A., Cardinaud, C., Peignon-Fernandez, M. C., & Alves, L. L. (2009). Global model and diagnostic of a low-pressure SF6/Ar inductively coupled plasma. *Plasma Sources Science and Technology*, *18*(2), 025001.

[212] Chaplin, V. H., & Bellan, P. M. (2015). One-dimensional time-dependent fluid model of a very high density low-pressure inductively coupled plasma. *Journal of Applied Physics*, *118*(24), 243303.

[213] Corr, C. S., Gomez, S., & Graham, W. G. (2012). Discharge kinetics of inductively coupled oxygen plasmas: experiment and model. *Plasma Sources Science and Technology*, *21*(5), 055024.

[214] Seo, S. H., Chung, C., & Chang, H. Y. (2000). Review of heating mechanism in inductively coupled plasma. *Surface and Coatings Technology*, *131*(1-3), 1-11.

[215] Chabert, P., & Braithwaite, N. (2011). *Physics of radio-frequency plasmas*. Cambridge University Press.

[216] Punjabi, S. B., Barve, D. N., Joshi, N. K., Das, A. K., Kothari, D. C., Ganguli, A. A., Sahasrabhude, S N & Joshi, J. B. (2019). Computational Fluid Dynamics (CFD) Simulations and Experimental Measurements in an Inductively-Coupled Plasma Generator Operating at Atmospheric Pressure: Performance Analysis and Parametric Study. *Processes*, *7*(3), 133.

[217] Singh, S. V. (2005). Investigation of ICP RF discharges by means of a Langmuir probe. Thesis university of Bochum 2004.

[218] McCarter, A. J. (2005). *Plasmoids and the E-to-H transition in an Inductively Coupled Plasma* (Doctoral dissertation, Dublin City University).

[219] Singh, S. V., & Pargmann, C. (2008). Electrical characterization of an inductively coupled gaseous electronics conference reference cell. *Journal of Applied Physics*, *104*(8), 083303.

[220] Lisovskiy, V., Yegorenkov, V., Artushenko, E., Booth, J. P., Martins, S., Landry, K., ... & Cassagne, V. (2012). Normal regime of the weak-current mode of an rf capacitive discharge. *Plasma Sources Science and Technology*, *22*(1), 015018.

[221] Godyak, V. A., Piejak, R. B., & Alexandrovich, B. M. (1999). Experimental setup and electrical characteristics of an inductively coupled plasma. *Journal of applied physics*, *85*(2), 703-712.

[222] Godyak, V. A., & Alexandrovich, B. M. (2017). Power measurements and coupler optimization in inductive discharges. *Review of Scientific Instruments*, *88*(8), 083512.

[223] Lee, M. Y., Nam, J. S., Yang, I. M., & Seo, J. H. (2018). Equivalent circuit and numerical analyses of an inductively coupled plasma torch with a tapped induction coil. *AIP Advances*, *8*(11), 115208.

[224] Miller, P. A., Hebner, G. A., Greenberg, K. E., Pochan, P. D., & Aragon, B. P. (1995). An inductively coupled plasma source for the gaseous electronics conference RF reference cell. *Journal of research of the National Institute of Standards and Technology*, *100*(4), 427.